JYVÄSKYLÄ STUDIES IN COMPUTING
124

Tuomas Puurtinen

# Numerical Simulation of Low Temperature Thermal Conductance of Corrugated Nanofibers

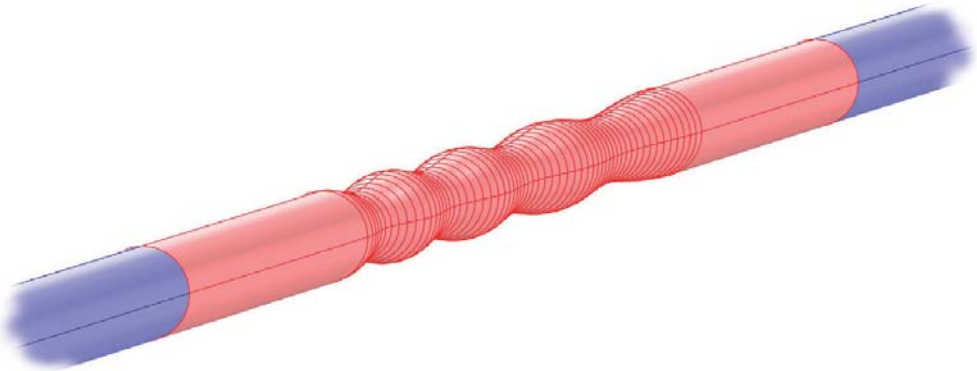

JYVÄSKYLÄN YLIOPISTO

JYVÄSKYLÄ STUDIES IN COMPUTING 124

Tuomas Puurtinen

# Numerical Simulation of Low Temperature Thermal Conductance of Corrugated Nanofibers

Esitetään Jyväskylän yliopiston informaatioteknologian tiedekunnan suostumuksella
julkisesti tarkastettavaksi yliopiston Agora-rakennuksen auditoriossa 2
joulukuun 18. päivänä 2010 kello 12.

Academic dissertation to be publicly discussed, by permission of
the Faculty of Information Technology of the University of Jyväskylä,
in the Agora building, auditorium 2, on December 18, 2010 at 12 o'clock noon.

UNIVERSITY OF JYVÄSKYLÄ

JYVÄSKYLÄ 2010

# Numerical Simulation of Low Temperature Thermal Conductance of Corrugated Nanofibers

JYVÄSKYLÄ STUDIES IN COMPUTING 124

Tuomas Puurtinen

# Numerical Simulation of Low Temperature Thermal Conductance of Corrugated Nanofibers

UNIVERSITY OF JYVÄSKYLÄ

JYVÄSKYLÄ 2010

Editor
Timo Männikkö
Department of Mathematical Information Technology, University of Jyväskylä
Pekka Olsbo, Sini Rainivaara
Publishing Unit, University Library of Jyväskylä

Cover picture: Perturbed cylindrical domain which
continues to infinity as a straight cylinder

URN:ISBN:978-951-39-4144-4
ISBN 978-951-39-4144-4 (PDF)

ISBN 978-951-39-4094-2 (nid.)
ISSN 1456-5390



Jyväskylä University Printing House, Jyväskylä 2010

## ABSTRACT

Puurtinen, Tuomas
Numerical simulation of low temperature thermal conductance of corrugated nanofibers
Jyväskylä: University of Jyväskylä, 2010, 114 p.
(Jyväskylä Studies in Computing
ISSN 1456-5390; 123)
ISBN 978-951-39-4094-2 (nid.), 978-951-39-4144-4 (PDF)
Finnish summary
Diss.

In the present work the low temperature thermal conductance of dielectric elastic nanofibers was numerically simulated. A special smooth cylindrical or elliptical corrugation was shaped on the fiber boundary in order to lower the thermal conductance by reflecting low energy phonons. On temperature range $T = 0.1 - 10K$ thermal energy is carried mainly by flexural, torsional and longitudinal waves, which were simulated here with 1D and 3D models. Finite element method was used to solve frequency spectrum of periodical fibers and scattering matrix for the waves through a finite locally periodical fibers. Landauer formalism was then used to calculate the thermal conductance. For numerical calculation there were taken silicon nanofibers as typical examples. It was found that 3D frequency spectrum of axially symmetrical periodical corrugation can be approximated with 1D frequency spectra obtained from certain simple differential equations. By simulating numerous boundary shapes, suggestions were made about the parameter range where 1D models give reliable results. It was concluded that 1D models can be used to reliably calculate transmission probability curves for low energy phonons. Finally, a special chirped circular-elliptical corrugation was designed to decrease the thermal conductance by 90% on range $T = 0.1 - 1K$.

Keywords: corrugation, nanofiber, phonon transport, low temperature, thermal conductance, frequency spectrum, scattering matrix, numerical simulation, finite element method

**Author**

Tuomas Puurtinen
Department of Mathematical Information Technology
University of Jyväskylä
Finland
Email: tuomas.a.puurtinen@jyu.fi

**Supervisors**

Professor Lev Baskin
Department of Mathematics
Saint Petersburg State University for Telecommunications
Russia

Professor Pekka Neittaanmäki
Department of Mathematical Information Technology
University of Jyväskylä
Finland

Professor Boris Plamenevsky
Department of Mathematical Physics
Saint Petersburg State University
Russia

**Reviewers**

Professor Ilari Maasilta
Department of Physics
University of Jyväskylä
Finland

Professor Dmitri Sokolovsky
Department of Physical Chemistry
University of the Basque Country
Spain

Professor Dimitri Yafaev
IRMAR, Campus de Beaulieu
University of Rennes 1
France

**Opponent**

Professor Gennadi G. Sominski
Department of Physical Electronics
Saint Petersburg State Politechnical University
Russia

## ACKNOWLEDGEMENTS

I would like to thank my supervisors Professor Lev Baskin (St. Petersburg University for Telecommunications, Russia), Professor Pekka Neittaanmäki (University of Jyväskylä, Finland) and Professor Boris Plamenevsky (St. Petersburg State University, Russia) for their expert guidance and inestimable support. I would also like to express my gratitude to Prof. Ilari Maasilta, Prof. Dmitri Sokolovsky and Prof. Dimitri Yafaev for reviewing the manuscript. Doctor Alexey Pozharskiy deserves special thanks for helping me with MATLAB programming.

This work was financially supported by COMAS Graduate School of the University of Jyväskylä.

Tuomas Puurtinen
Jyväskylä, November 2010

## LIST OF FIGURES


FIGURE 1 Schematic picture of bolometer leg. ..... 12
FIGURE 2 Finitely perturbed waveguide. ..... 15
FIGURE 3 Scattering of 1D torsional left-incoming wave. ..... 20
FIGURE 4 Frequency spectrum of periodical 3D waveguide with harmonically perturbed boundary. ..... 21
FIGURE 5 Four eigenmodes of different types in almost cylindrical periodical fiber. ..... 22
FIGURE 6 Comparison of spectral gap locations and widths from 1D and 3D models. ..... 23
FIGURE 7 Comparison of transmission coefficients of longitudinal waves in 1D and 3D models. ..... 24
FIGURE 8 Thermal conductance by the lowest energy phonons. ..... 25
FIGURE 9 Comparison of longitudinal transmission coefficients of fibers with separate and combined perturbations. ..... 26
FIGURE 10 Flexural modes in a straight cylinder. ..... 30
FIGURE 11 Torsional and longitudinal modes in straight cylinder. ..... 31
FIGURE 12 Analytical solution of 3D longitudinal mode. ..... 36
FIGURE 13 Slightly perturbed periodicity cell. ..... 38
FIGURE 14 Frequency spectrum of almost cylindrical 3D silicon fiber. ..... 40
FIGURE 15 Frequency spectrum of eigenmodes with characteristics of flexural waves in almost cylindrical 3D fiber. ..... 42
FIGURE 16 Flexural eigenmodes in almost cylindrical periodical fiber. ..... 43
FIGURE 17 Frequency spectrum of eigenmodes with characteristics of torsional waves in almost cylindrical 3D fiber. ..... 44
FIGURE 18 Torsional eigenmodes in almost cylindrical periodical fiber. ..... 45
FIGURE 19 Frequency spectrum of eigenmodes with characteristics of longitudinal waves in almost cylindrical 3D fiber. ..... 46
FIGURE 20 Longitudinal eigenmodes in almost cylindrical periodical fiber. 47
FIGURE 21 Differential element of thin almost cylindrical fiber under transversal motion. ..... 49
FIGURE 22 Differential element of thin almost cylindrical fiber under torsional motion. ..... 51
FIGURE 23 Differential element of thin almost cylindrical fiber under longitudinal motion. ..... 52
FIGURE 24 Comparison of 1D and 3D frequency spectra of flexural waves. 54
FIGURE 25 Comparison of 1D and 3D frequency spectra of torsional and longitudinal waves. ..... 55
FIGURE 26 Comparison of width and location of flexural spectral gaps from 1D and 3D models. ..... 57
FIGURE 27 Comparison of width and location of torsional spectral gaps from 1D and 3D models. ..... 58

FIGURE 28 Comparison of width and location of longitudinal spectral gaps from 1D and 3D models. ..... 59
FIGURE 29 Spectral gap locations as a function of period length. ..... 60
FIGURE 30 Spectral gap widths as a function of period length. ..... 61
FIGURE 31 Scattering of 3D longitudinal wave. ..... 67
FIGURE 32 Scattering 1D torsional wave. ..... 69
FIGURE 33 Comparison of transmission coefficients of longitudinal waves from 1D and 3D models (2 periods). ..... 70
FIGURE 34 Comparison of transmission coefficients of longitudinal waves from 1D and 3D models (7 periods). ..... 71
FIGURE 35 Comparison of transmission coefficients and frequency spectra of flexural waves. ..... 76
FIGURE 36 Comparison of transmission coefficients and frequency spectra of torsional waves. ..... 77
FIGURE 37 Comparison of transmission coefficients and frequency spectra of longitudinal waves. ..... 78
FIGURE 38 Thermal conductance of a fiber with an ideal forbidden band. .. 82
FIGURE 39 Thermal conductance in infinitely long periodical fiber. ..... 83
FIGURE 40 Normalized thermal conductance by 1D longitudinal waves. ..... 84
FIGURE 41 Normalized thermal conductance by 1D flexural and torsional waves. ..... 85
FIGURE 42 3D surface of transmission coefficients of 1D longitudinal waves for different number of perturbations. ..... 90
FIGURE 43 Thermal conductance by longitudinal waves in thin Silicon fiber. 91
FIGURE 44 Thermal conductance by torsional waves in a thin Silicon fiber.. 92
FIGURE 45 Thermal conductance by flexural waves in (cylindrical) thin Silicon fiber. ..... 93
FIGURE 46 Comparison of 1D and 3D frequency spectra of periodical elliptically perturbed fiber. ..... 95
FIGURE 47 3D surface of transmission coefficients of 1D flexural waves in elliptically perturbed fiber. ..... 96
FIGURE 48 Thermal conductance by flexural waves in thin (elliptical) Silicon fiber. ..... 97
FIGURE 49 Transmission coefficients of longitudinal waves in separate perturbations. ..... 98
FIGURE 50 Transmission coefficients of longitudinal waves in combined perturbations. ..... 99
FIGURE 51 Program diagram. ..... 103

## CONTENTS

ABSTRACT
ACKNOWLEDGEMENTS
LIST OF FIGURES
CONTENTS

1 INTRODUCTION ..... 11
1.1 Physical background ..... 11
1.2 Mathematical model of scattering in an elastic wire ..... 14
1.3 Computational method for scattering matrices ..... 17
1.4 One dimensional models of scattering in an elastic wire ..... 18
1.5 Outline of the main results ..... 21

2 THREE DIMENSIONAL MODEL OF AN ELASTIC NANOFIBER ..... 27
2.1 Elastic waves in straight cylinder ..... 28
2.2 On solving the Lamé's equation analytically in a cylinder ..... 30
2.3 First longitudinal phonon modes in a cylinder ..... 34

3 CLASSIFICATION OF ELASTIC WAVES IN ALMOST CYLINDRICAL DOMAINS ..... 37
3.1 Frequency spectrum of periodical domain ..... 38
3.2 Defining algorithm for the lowest elastic modes ..... 40
3.3 Flexural waves ..... 41
3.4 Torsional waves ..... 44
3.5 Longitudinal waves ..... 46

4 ONE DIMENSIONAL MODELS OF ELASTIC WAVES ..... 48
4.1 Flexural waves ..... 49
4.2 Torsional waves ..... 50
4.3 Longitudinal waves ..... 52
4.4 Comparison of frequency spectra produced with 1D and 3D models ..... 53
4.5 Spectral gaps in 1D and 3D models ..... 56

5 TRANSMISSION COEFFICIENTS ..... 62
5.1 Scattering of elastic waves in perturbed 3D fiber ..... 63
5.2 Boundary amplitude method for longitudinal 3D waves ..... 65
5.3 Boundary amplitude method for 1D waves ..... 68
5.4 Comparison of transmission coefficients of longitudinal 1D and 3D waves ..... 70
5.5 Scattering matrix method for 3D and 1D models ..... 72
5.6 Transmission coefficients in 1D ..... 75

6 THERMAL CONDUCTANCE ..... 79

6.1 Equation for thermal conductance by acoustic phonons ..... 79
6.2 Infinite periodical fibers ..... 81
6.3 Finite periodical fibers ..... 84

7 DESIGNING THE PERTURBATION ..... 86
7.1 Chirped fibers ..... 86
7.2 Fibers with cylindrical chirped deformation ..... 89
7.3 Elliptical balanced deformation for reflecting flexural waves ..... 94
7.4 Fibers with several perturbed parts ..... 97

8 NUMERICAL IMPLEMENTATION IN MATLAB/COMSOL ..... 100
8.1 Finite element method ..... 100
8.2 Program code ..... 102
8.3 One dimensional simulation ..... 103
8.4 Three dimensional simulation ..... 105
8.5 Post processing ..... 107

9 CONCLUSIONS AND FURTHER STUDY ..... 109

REFERENCES ..... 111

YHTEENVETO (FINNISH SUMMARY) ..... 114

# 1 INTRODUCTION

The thesis is devoted to numerical studies of phonon transport in elastic dielectric nanofibers. The investigation is stimulated by the possibility of using such fibers for producing thermo-insulating structures in nano- and microelectronics. In [1, 2] it was shown how to decrease the thermal conductivity of a fiber by corrugating part of its boundary. A special shallow corrugation can sharply diminish the fiber thermal conductivity without damaging its mechanical strength. In the thesis we analyze numerically various mathematical models of elastic dielectric nanofibers in order to justify and develop the method suggested in [1, 2].

Chapter 1 contains a short physical background, a description of mathematical models, and an outline of the main results. Having familiarized himself with Introduction, the reader can understand the mathematical statement of problem, the purpose and the results of the thesis. Chapters 2-4 are devoted to comparing 3D and 1D models of a nanofiber. These preparatory chapters justify numerically the change from 3D models to 1D models. The main results are exposed in Chapters 5-7.

## 1.1 Physical background

Heat removal from electronic devices and heat insulation of such devices play an important role in microelectronics. A number of new type devices operate at temperature about $4.2K$ and less. For one example, low temperature operating conditions are essential for resonant transistors because only such conditions provide a sufficiently large electron free path. Another example is presented by detectors of infrared radiation known as bolometers that reveal an increase in temperature of sensors caused by the radiation. Such detectors operate at temperature $T \leq 1K$. Heat leaking through the sensor legs sharply diminishes the device sensitivity. Therefore, elaboration of heat insulating facilities which operate at the mentioned low temperature region is of fundamental importance. The surface area of a sensor can be approximately $1\mu m^2$, the length of a sensor leg av-

erages several $\mu m$ while the leg cross-section has diameter of $10nm$. Under such conditions, the heat conductivity acquires a purely quantum character.

In an elastic dielectric nanofiber heat energy is transferred by elastic waves (see e.g. [3, 4, 5]). From the quantum mechanical point of view, such a wave with wave vector $k$ and frequency $\omega = \omega(k)$ can be represented as a flow of particles called phonons. Every phonon possesses energy $E = \hbar\omega$ and crystal momentum $p = \hbar k$. At temperature $T \leq 1K$ the phonon mean free path exceeds the fiber length and phonons propagate freely without collisions through the bolometer leg. In other words, the flow is within the ballistic regime. Schematic picture is given in Figure 1.

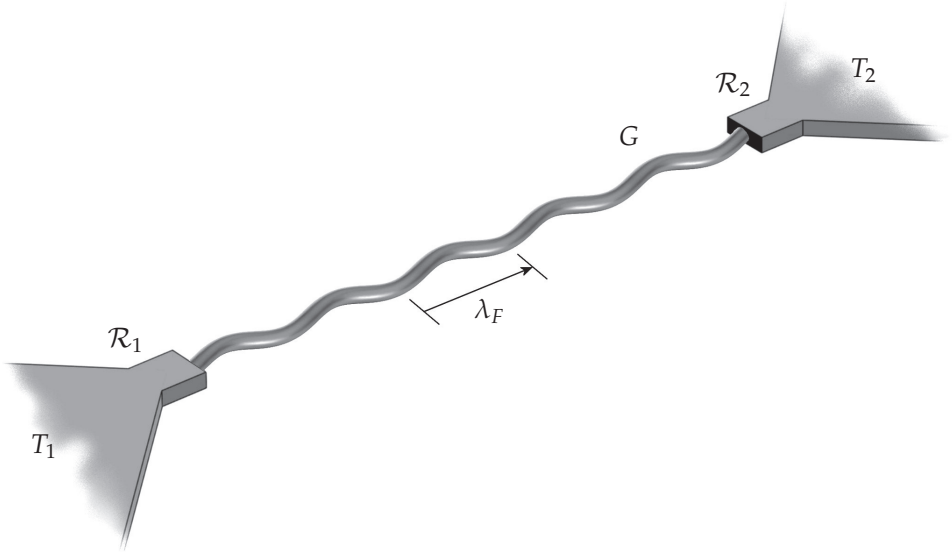


FIGURE 1 Schematic picture of a cylindrical bolometer support leg $G$ carrying thermal energy between reservoirs $\mathcal{R}_1$ and $\mathcal{R}_2$ with temperatures $T_1$ and $T_2$, respectively, by flexural elastic motion with wavelength $\lambda_F$.

The elastic waves can be of various types. For instance, in an isotropic bulk crystal there exist a longitudinal wave and two independent transverse waves. In a thin fiber at low frequencies, because of presence of the boundary, one can recognize a longitudinal, a torsional, and two independent transverse waves. Transverse waves in beams are often also called flexural. The type of a wave will be indicated by the index $\alpha$. In what follows, $E = \hbar\omega_\alpha = \hbar\omega_\alpha(k_\alpha)$ stands for the phonon energy of type $\alpha$, where $\alpha = F$, $T$ or $L$, signifying flexural, torsional or longitudinal waves, respectively.

Let two reservoirs $\mathcal{R}_1$ and $\mathcal{R}_2$ with temperatures $T_1$ and $T_2$, respectively, be connected by a ballistic wire $G$. It means that the free path of the phonons is supposed to be much greater than the length of $G$. The quantity of thermal energy passing through $G$ from $\mathcal{R}_1$ to $\mathcal{R}_2$ in a unit time is

$$\frac{\partial Q}{\partial t} = \frac{1}{2\pi} \sum_\alpha \int \hbar\omega [n(\omega, T_2) - n(\omega, T_1)] p_\alpha(\omega) \, \mathrm{d}\omega \,, \tag{1}$$

where $n(\omega, T)$ stands for the phonon distribution function defined by

$$n(\omega, T) = (e^{\hbar\omega/k_B T} - 1)^{-1}, \tag{2}$$

which means that phonons obey Bose-Einstein statistics. Quantity $p_\alpha(\omega)$ denotes the probability for a phonon of mode $\alpha$ and frequency $\omega$ to go through $G$, and $k_B$ is the Boltzmann constant. Integration is over the whole spectrum of the phonon frequencies. We suppose that the reservoirs $\mathcal{R}_1$ and $\mathcal{R}_2$ are sustained at constant temperature, so that $\partial Q/\partial t$ is time-independent.

Let us assume that $|T_2 - T_1|$ is small in comparison with $T_1$ and $T_2$ and change (1) for

$$\frac{\partial Q}{\partial t} = \frac{T_2 - T_1}{2\pi} \sum_\alpha \int \hbar\omega \frac{\partial n}{\partial T}(\omega, T) p_\alpha(\omega)\, \mathrm{d}\omega\,, \tag{3}$$

where $T$ is a number in $[T_1, T_2]$. The value

$$\Omega = \frac{\partial Q}{\partial t} / (T_2 - T_1)$$

is called the thermal conductance. Quantity $\Omega$ has a unit $[W/K]$ and in low temperatures it is independent of the fiber length. Throughout the text, when necessary, we use a term *conductivity* in reference to length dependent thermal conduction with unit $[W/Km]$.

We take into account (2), substitute the expression for $\partial n/\partial T$ into (3), and obtain the Landauer formula [6] for phonons [7]

$$\Omega = \frac{\hbar^2}{2\pi k_B T^2} \sum_\alpha \int_{\omega_{\alpha,\min}}^{\omega_{\alpha,\max}} p_\alpha(\omega) \frac{\omega^2 \exp(\beta\hbar\omega)}{(\exp(\beta\hbar\omega) - 1)^2}\, \mathrm{d}\omega\,, \tag{4}$$

where $\beta = 1/(k_B T)$, $T \approx T_1 \approx T_2$, and $\omega_{\alpha,\min}$ ($\omega_{\alpha,\max}$) is the minimal (maximal) phonon frequency of mode $\alpha$.

Let us dwell on (4). Suppose that $\omega_{\alpha,\min} = 0$ and $\omega_{\alpha,\max} = +\infty$. Moreover, we assume that $p_\alpha(\omega) \equiv 1$. Then the corresponding integral in (4) equals $\pi^2 k_B^3 T^3/(3\hbar^3)$ and the contribution of such a term to $\Omega$ is $\Omega_{univ} := (\pi/6) k_B^2 T/\hbar$. This quantity is called the universal quantum of thermal conductance. This value is independent of the properties of a dielectric and its geometry. If $\beta\hbar\omega_{\alpha,\min} \gg 1$, then the contribution of mode $\alpha$ to $\Omega$ is exponentially small and can be neglected.

In a cylindrical rod, there are four independent modes $\alpha$ for which $\omega_\alpha(0) = 0$: a longitudinal mode, a torsional mode, and two flexural modes. For the other modes $\omega_{\alpha,\min} \sim n v_\alpha/D$, where $v_\alpha$ is the characteristic propagation speed of elastic wave $\alpha$ and $D$ is the diameter of the rod cross-section with $n$ being a positive integer. At low temperature $T < 1K$ and small $D < 100nm$ the mentioned four modes give the main contribution to $\Omega$, so

$$\Omega \simeq 4 \frac{\pi k_B^2 T}{6\hbar}.$$

Let us estimate the effect of the conductance of a bolometer suspending fiber on the device sensitivity. For the sake of simplicity we assume that the bolometer

is attached to a cooling system by only one leg. If energy of power $W$ falls upon the bolometer sensor then the temperature increase is equal to $T_2 - T_1 = W/\Omega$. Thus the bolometer sensitivity is inversely proportional to $\Omega$.

It is known that at low temperature an unstructured surface roughness of a wire diminishes the wire heat conductance due to the constructive interference of scattered waves [8, 9]. As was shown in [1, 2], a roughness structured in a proper way can sharply decrease the conductance of a wire. More precisely, it was described there how to form the surface of a wire in order that the transmission probabilities $p_\alpha(\omega)$ would be small for the phonons in a sufficiently wide frequency band. Let us outline the idea in more detail. Consider an infinite elastic wire with periodically varying cross-section as a model. In such a wire a phonon cannot propagate if its energy remains within some frequency intervals called spectral gaps. There is a good reason to believe that in a finite cylindrical fiber containing a sufficiently long periodically corrugated part the transmission probabilities $p_\alpha(\omega)$ are relatively small for the phonons with energy in a spectral gap of the aforementioned model wire. To extend the energy interval corresponding to the decay of transmission probabilities one can change the corrugated part with periodically varying cross-section for a goffer with "perturbed period" linearly varying along the wire. Such a device is similar to that used for the Bragg optical gratings to enlarge their operating range [10].

## 1.2 Mathematical model of scattering in an elastic wire

Let $\Pi$ be the cylinder $\{\, x = (x_1, x_2, x_3) \in \mathbb{R}^3 \,:\, (x_1, x_2) \in \Theta,\ -\infty < x_3 < +\infty \,\}$ whose cross-section $\Theta$ is a two-dimensional bounded and connected domain with smooth boundary. Assume that an elastic homogeneous and isotropic wire $G$ coincides with $\Pi$ for $|x_3| > R$, $R$ being a positive number, while

$$G(R) = \{\, x \in G \,:\, |x_3| \le R \,\}$$

is a perturbed part of $G$, see Figure 2. Later we also use $G(S)$, $S > R$, where a finitely long straight cylinders of length $S - R$ are attached to both ends of $G(R)$. Choosing $G(R)$, we shall try to make the transmission probabilities through the wire as small as possible.

We consider the homogeneous boundary value problem in elasticity theory

$$\begin{aligned} \mathcal{L}u(x) &= 0, \quad x \in G, \\ \nu \cdot \sigma(u)(x) &= 0, \quad x \in \partial G, \end{aligned} \tag{5}$$

where $u = (u_1, u_2, u_2)$ stands for displacements and

$$\mathcal{L}u = \mu \triangle u + (\lambda + \mu) \nabla \operatorname{div} u + \rho\omega^2 u. \tag{6}$$

Lamé's constants $\lambda$ and $\mu$ which satisfy $\mu > 0$ and $3\lambda + 2\mu > 0$, and density $\rho$ together with the frequency $\omega$ are supposed to be constant. As usual $\partial G$ denotes

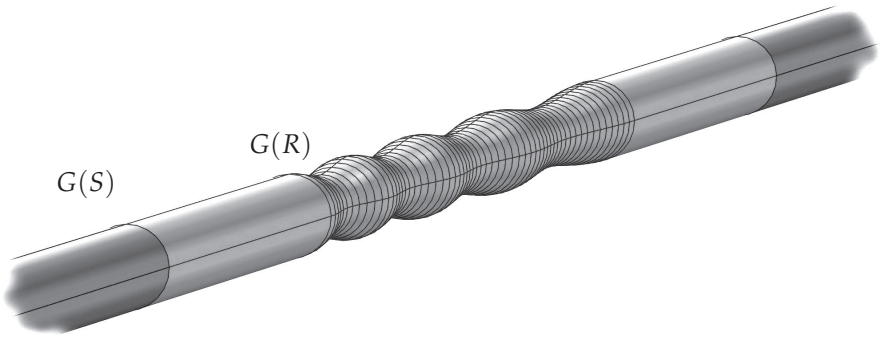


FIGURE 2 Example of a perturbed cylindrical domain which continues to infinity as a straight cylinder. Part $G(R)$ contains the perturbations and part $G(S)$, $S > R$, printed in red, contains in addition two cylinders of length $S - R$ attached to circular ends of $G(R)$.

the boundary of $G$ and $\nu$ is the outward unit normal to $\partial G$. Finally, $\sigma$ is the stress tensor with Cartesian components

$$\sigma(u) = (\lambda e_{kk}\delta_{ij} + 2\mu e_{ij})_{ij}, \tag{7}$$

where $e_{ij} = \frac{1}{2}(\partial_i u_j + \partial_j u_i)$, $i, j = 1, 2, 3$. By setting the stress tensor zero one considers so called free boundary problem, i.e. an elastic problem without outer mechanical forces affecting on the boundary. A solution $Y$ to problem (5) is called a continuous spectrum eigenfunction corresponding to the frequency $\omega$, if $Y$ satisfies the following conditions:

- $Y$ is a bounded function on $G$, $|Y(\cdot)| \leq C$, $C$ constant,
- $Y$ does not converge to zero at infinity, $|Y(x)| \not\to 0$ as $|x| \to \infty$.

The continuous spectrum eigenfunctions play the role of phonon wave functions. It is known that the total number of eigenfunctions below eigenfrequency $\omega$ increases like a staircase function as $\omega$ increases. The step values $\omega_i$ of this function are called "threshold" values. If a frequency band $[\omega_1, \omega_2]$ contains no threshold values then for any $\omega \in [\omega_1, \omega_2]$ there is known to exist the same even number of linearly independent continuous spectrum eigenfunctions (CSE). We assume here to consider only frequencies below the first threshold. In the elastic theory threshold values $\omega_i$ are related to cut-off frequencies of higher elastic modes such as shear modes or modes with higher transversal quantum number. Denote the number of CSE by $2M$. In the space of CSE's corresponding to a frequency $\omega$, there can be chosen a basis $\{ Y_1(\cdot, \omega), \ldots, Y_{2M}(\cdot, \omega) \}$ such that

$$Y_j(x, \omega) = w_j^+(x, \omega) + \sum_{k=1}^{2M} s_{jk}(\omega) w_k^-(x, \omega) + \mathcal{O}(e^{-\gamma|x_3|}), \tag{8}$$

where $j = 1, \dots, 2M$, the functions $w_j^+$ ($w_j^-$) can be explicitly described and are called incoming (outgoing) waves, the matrix $\mathbf{S}(\omega) = (s_{jk}(\omega))_{j,k=1}^{2M}$ is unitary and called the scattering matrix, $\gamma$ being a sufficiently small positive number. The existence of such solutions was discussed e.g. in [11].

Let us turn to the solutions $Y_j$ in (8) for $j = M+1, \dots, 2M$. The $Y_j$ describes the phonon incoming from $-\infty$ as the wave $w_j^+$, which scatters from the perturbed part $G(R)$ into $2M$ outgoing waves $w_k^-$. The sum

$$p_j(\omega) := \sum_{k=1}^{M} |s_{jk}(\omega)|^2 \tag{9}$$

is called the transmission coefficient while

$$\sum_{k=M+1}^{2M} |s_{jk}(\omega)|^2$$

is the reflection coefficient. The $p_j(\omega)$ in (9) can be interpreted as the transmission probability through the wire $G$ from $-\infty$ to $+\infty$ for the phonon $Y_j$.

We now explain the choice of distorted part $G(R)$ (see Fig. 2). Let us consider as a model an infinite waveguide $\Xi$ whose cross-section

$$\Theta(t) = \{\, x : x_3 = t \,\}$$

periodically depends on $t$ with period $a$, $\Theta(t+a) = \Theta(t)$. Introduce the auxiliary problem

$$\begin{aligned} \mathcal{L}u(x) &= 0, \quad x \in \Xi, \\ \nu \cdot \sigma(u) &= 0, \quad x \in \partial\Xi \end{aligned} \tag{10}$$

with the same $\mathcal{L}$ and $\sigma$ as in (6) and (7). We seek solutions to problem (10) of the form $\exp(ikx_3)U(x)$ with real number $k$ and periodic function $U \not\equiv 0$ such that $U(x_1, x_2, x_3 + a) = U(x_1, x_2, x_3)$. The *ansatz* is based on well known Bloch's theorem for periodic potentials. To find $k$ and $U$, we obtain the problem

$$\begin{aligned} \mathcal{L}(\partial_{x_1}, \partial_{x_2}, \partial_{x_3} + k)U(x) &= 0, \quad x \in \mathcal{S}, \\ \nu \cdot \sigma(\partial_{x_1}, \partial_{x_2}, \partial_{x_3} + k)(U)(x) &= 0, \quad x \in \mathcal{T}, \end{aligned} \tag{11}$$

where $\mathcal{S} = \{\, x \in \Xi : 0 < x_3 < a \,\}$, $\mathcal{T} = \{\, x \in \partial\Xi : 0 < x_3 < a \,\}$. Notation means that every $\partial_{x_3}$ in definition of $\mathcal{L}$ and $\sigma$ is replaced with $\partial_{x_3} + k$ with other partial derivatives kept intact.

A number $k_0$ and a function $U_0$ satisfying (11) are called an eigenvalue and an eigenfunction of the problem. Given $k_0$ and $U_0$, the number $k_0 + 2\pi q/a$ and the function $\exp(-i2\pi q x_3/a)U_0(x)$ are an eigenvalue and an eigenfunction as well for $q = \pm 1, 2, \dots$.

Recall that the operator $\mathcal{L}$ depends on $\omega$ (see (6)). If there is no solution of the indicated form to problem (10) for some frequency $\omega_0$, then $\omega_0$ is said to be in

a spectral gap. In such a case the phonons with frequency $\omega_0$ cannot propagate in the waveguide $\Xi$.

In order to reduce thermal conductance of wire $G$ we have to reflect a considerably wide frequency band of phonons. Suppose we decided to reflect phonons with frequencies $[\omega_1, \omega_2]$. Let us assume we have found a collection of waveguides $\Xi_i$ with spectral gaps filling the band $[\omega_1, \omega_2]$. Then we can construct $G(R)$ by combining finite parts of $\Xi_i$ with lengths $l_i$ into series. It is reasonable to expect that transmission probability through the combined perturbation is decaying with exponential rate as $l_i, R \to +\infty$. There is also another way to extend the frequency interval corresponding to diminished transmission probabilities. One can construct a corrugated perturbation with periodically varying cross-section where the length of period is changing linearly. We intend to examine the thermal properties of such structures.

## 1.3 Computational method for scattering matrices

In order to find the scattering patterns for each incoming wave $w_j^+$, we seek the $j$-th row $(s_{j1}, \ldots, s_{j,2M})$ of the scattering matrix $\mathbf{S}$. As an approximation of the row we take a vector that minimizes one particular quadratic functional [12]. To construct the functional we introduce the boundary value problem in the truncated domain $G(S) = \{\, (x,y) \in G \,:\, |x| < S \,\}$ with $S > R$ so that the distorted part $G(R)$ of the waveguide $G$ is contained in $G(S)$ (see Figure 2):

$$\begin{aligned} \mathcal{L} Y_j^S(x) &= 0, \quad x \in G(S), \\ \nu \cdot \sigma(Y_j^S)(x) &= 0, \quad x \in \partial G(S) \setminus I(S), \end{aligned} \tag{12}$$

$$(\partial_{x_3} + i\zeta) Y_j^S = (\partial_{x_3} + i\zeta)(w_j^+ + \sum_{k=1}^{2M} a_k w_k^-), \quad x \in I(S), \tag{13}$$

where $I(S) = \{\, x \in G \,:\, x_3 = \pm S \,\}$ is the union of left and right truncation boundaries, $\zeta \neq 0$ a real number, and $a_1, \ldots, a_{2M}$ are arbitrary complex numbers. Let $Y_j^S$ be the solution to the above three equations depending on $a_1, \ldots, a_{2M}$. As approximation of the row $(s_{j1}, \ldots, s_{j,2M})$ we take the minimizer $a^0(S) = (a_1^0(S), \ldots, a_{2M}^0(S))$ of the functional

$$J_j^S(a_1, \ldots, a_{2M}) = \int_{I(S)} \left| Y_j^S - w_j^+ - \sum_{k=1}^{2M} a_k w_k^- \right|^2 \mathrm{d}A \tag{14}$$

on the unit sphere $\{\, a^0 \in \mathbb{R}^{2M} \,:\, |a_1^0|^2 + \ldots + |a_{2M}^0|^2 = 1 \,\}$ integrating over the both truncation boundaries. Let us motivate the above choice of approximation for $(s_{j1}, \ldots, s_{j,2M})$. The function $Y_j$ in (8) satisfies (12). Since the asymptotic relation (8) can be differentiated we have

$$(\partial_{x_3} + i\zeta) Y_j(x) = (\partial_{x_3} + i\zeta)(w_j^+(x) + \sum_{k=1}^{2M} a_k w_k^-(x)) + \mathcal{O}(e^{-\gamma |x_3|})$$

for $a_k = s_{jk}$, i.e. the function $Y_j$ leaves an exponentially small discrepancy in (13). Therefore one can expect that $a_k^0(S) \to s_{jk}$ with exponential rate as $S \to +\infty$ which was proved in [13].

To explain the algorithm in more detail we explicitly describe the dependence of $Y_j^S$ on the parameters $a_1, \dots, a_{2M}$. Therefore consider the auxiliary problems

$$\begin{aligned} \mathcal{L}U_k^{\pm}(x) &= 0, \quad x \in G(S), \\ \nu \cdot \sigma(U_k^{\pm})(x) &= 0, \quad x \in \partial G(S) \setminus I(S), \\ (\partial_{x_3} + i\zeta)U_k^{\pm} &= (\partial_{x_3} + i\zeta)w_k^{\pm}, \quad x \in I(S), \end{aligned}$$

for $k = 1, \dots, 2M$. Then $Y_j^S$ can be expressed in terms of the solutions $U_k^{\pm} = U_{k,S}^{\pm}$ to those problems with $Y_j^S = U_{j,S}^{+} + \sum_k a_k U_{k,S}^{-}$. We introduce the $2M \times 2M$-matrices $E^S$ and $F^S$ with entries

$$\begin{aligned} E_{ij}^S &= (U_i^- - w_i^-, U_j^- - w_j^-)_{I(S)}, \\ F_{ij}^S &= (U_i^+ - w_i^+, U_j^- - w_j^-)_{I(S)}, \end{aligned}$$

where

$$(V, W)_{I(S)} := \int_{I(S)} V(x)\overline{W(x)}\, \mathrm{d}A$$

is the complex inner product on the truncation boundaries. We also put

$$G_i^S = (U_i^+ - w_i^+, U_i^+ - w_i^+)_{I(S)}.$$

Now the functional (14) can be written in the form

$$J_j^N(a) = (aE^S, a) + 2\mathrm{Re}(F_j^S, a) + G_j^S.$$

The minimizer $a^0(S)$ satisfies $a^0(S)E^S + F_j^S = 0$.

## 1.4 One dimensional models of scattering in an elastic wire

In various situations a 3D system can be approximately described by means of a 2D or 1D models. It happens when the size of a 3D system, in one or two directions, is essentially less than the rest of the parameters determining the behavior of the system. Such a situation arises, for instance, for wave propagation in a fiber provided that the fiber length as well as the wave length are much greater than the cross-sectional diameter of the fiber. In this case the initial equations describing a 3D model can be approximately replaced by equations corresponding to 1D or 2D models. The passage from a 3D model to a model of lesser dimension can be implemented in various ways (by rigorous asymptotic approach, or by means of "physical" arguments, etc.), see [14, 15, 16, 17, 18, 19, 20, 21, 22, 23]. Such approaches allow to get "qualitative" descriptions of the process which is

adequate only over a limited range of the parameters. As a rule, the limits of the range can be clarified with a reasonable accuracy for applications by numerical experiments.

The low temperature thermal conductance of elastic dielectric fibers is mainly determined by waves of frequencies $\hbar\omega \sim k_B T$, which have wavelengths $\lambda$ in the range $100 - 1000nm$ at sub-Kelvin temperatures. Thus, for nanofibers one can easily have the wavelength much larger than the fiber diameter. Therefore, the passage is possible from 3D to 1D systems. One of the purpose of the work is the clarification of the parameter range where the passage is justified e.g. in dependence on the geometry of deformed fiber, the deformation amplitude of the surface or the relation $S/D$ of the fiber length $S$ and the cross-sectional diameter $D$.

In a cylinder each of the massless modes is mainly one dimensional on their nature, i.e. each mode has major displacement component in only one direction in some coordinate system. Flexural and longitudinal modes have major displacement in $x := x_1$, $y := x_2$ or $z := x_3$-directions and torsional to $\theta$-direction in cylindrical coordinate system. Therefore one can expect a good agreement with results from 1D and 3D models.

We have chosen three simple 1D ordinary differential equation models to approximate different 3D waves. The equations are well known (e.g., see [18]) and can be easily derived from physical basis. Assume that the geometry of 3D fiber $G(S)$ can be defined by the graphs of two curves $B_x = B_x(z)$ and $B_y = B_y(z)$ so that

$$G(S) = \{\, (x, y, z) \in \mathbb{R}^3 \,:\, x^2/B_x(z)^2 + y^2/B_y(z)^2 \leq 1,\ |z| \leq S \,\}.$$

The defining relation in the set is the one for ellipse so the cross-section of $G(S)$ for each $|z| \leq S$ is an ellipse with semi-axes $B_x(z)$ and $B_y(z)$. If $B_x(z) = B_y(z)$ the cross-section is a circle.

To simulate flexural phonon modes with polarization in $x$-direction we use

$$-\frac{\partial^2}{\partial z^2}\left(B_x(z)B_y(z)^3\frac{\partial^2 u(z)}{\partial z^2}\right) = \frac{4\rho}{E}B_x(z)B_y(z)\omega^2 u(z), \quad z \in ]-S, S[, \tag{15}$$

where $\rho$ is the density, $E = \mu(3\lambda + 2\mu)/(\lambda + \mu)$ is Young modulus and $\omega$ is the angular frequency of the wave. For $y$-polarized flexural waves indices $x$ and $y$ in the above equation are interchanged. For torsional modes we use equation

$$\frac{\partial}{\partial z}\left[\frac{B_x^3(z)B_y^3(z)}{B_x^2(z) + B_y^2(z)}\frac{\partial u_\theta(z)}{\partial z}\right] = \frac{\rho}{4\mu}B_x(z)B_y(z)(B_x^2(z) + B_y^2(z))\omega^2 u_\theta(z), \tag{16}$$

for all $z \in ]-S, S[$, and for longitudinal modes equation

$$\frac{1}{A(z)}\frac{\partial}{\partial z}\left(A(z)\frac{\partial u(z)}{\partial z}\right) = \frac{\rho}{E}\omega^2 u(z), \quad z \in ]-S, S[. \tag{17}$$

In (17) notation $A(z) = \pi B_x(z)B_y(z)$ stands for the area of cross-section of the 3D domain at $z$.

The equations (15), (16) and (17) are used as a replacement for Lamé's equation (6) on 1D domain. To calculate 1D spectrum for each phonon type in the periodical domain the periodical boundary condition is set with

$$\exp(ikl)u(-S) = u(S),$$

where $k$ is a wave vector and $l$ is the periodicity length of the domain. To solve transmission probabilities $p_\alpha(\omega)$ with solving first the scattering matrix we use similar boundary conditions as in 3D case except that $x$ and $y$-directional partial derivatives are excluded.

We also use a direct way to calculate transmission probabilities from 1D models by comparing the amplitudes of incoming $w^+(z) = exp(i\zeta z)$ and outgoing waves $w^-(z) = exp(\pm i\zeta z)$ from scattering event. In Figure 3 is presented

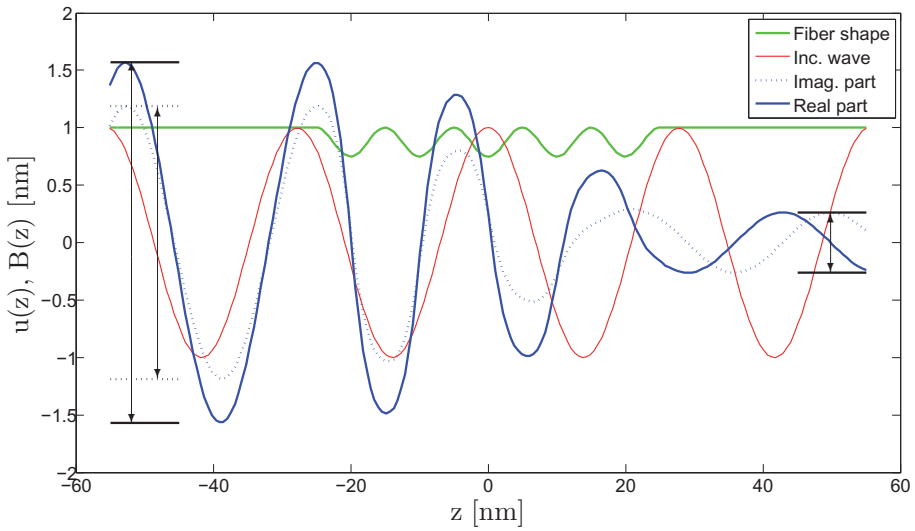


FIGURE 3 Scattering of 1D torsional left-incoming wave from finite periodical perturbation. Boundary shape of 1D fiber is printed in green. Solid (dotted) blue line is the real (imaginary) part of scattered displacement field in $\theta$-direction in cylindrical coordinate system, respectively. Red curve is the incoming wave shape, which is plotted also to left side of the perturbation for comparing the phase shift of field after scattering. Field amplitudes at boundaries, which are solved by fitting sin-curves in the solution, are drawn with black.

a blue displacement field from scattering incident around a perturbation marked with green. Real and imaginary amplitudes $A_{\text{left}}$, $A_{\text{right}}$ at left and right of solution $u$ are measured at the boundary by fitting sin-curves on the solution. Both the real and imaginary part amplitudes must be solved because the incoming and outgoing wave formulation was done in complex form. Finally, the transmission

probability can be calculated with

$$p_\alpha = \frac{1}{2}|A_{\text{right}}|^2,$$

as is shown in Chapter 5.

## 1.5 Outline of the main results

In this section we represent the main results of the research:

1. The spectra of elastic waves in periodically perturbed 3D waveguides were calculated numerically. In Figure 4 we show a typical frequency spectrum of periodical domain with perturbation strength 25.1%. We investigated

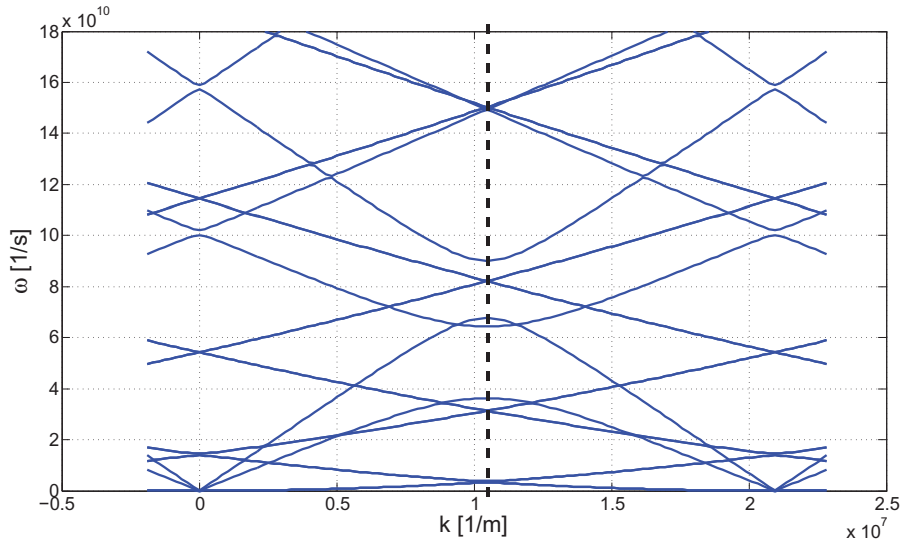


FIGURE 4 Frequency spectrum of axi-symmetrical periodical 3D waveguide with harmonically perturbed boundary. Length of periodicity cell in the perturbation is $l = 300nm$ with diameter $D = 20nm$. Perturbation strength is 25%. Material parameters were chosen for silicon (Si). Black dashed line shows the Brillouin zone edge.

the width of forbidden band gap for different elastic modes and its dependence on the strength of deformation of the waveguide. We discovered that for torsional and longitudinal modes a comparably wide spectral gap opened when a periodical deformation of a form of cos-function was used with a small strength of perturbation. For flexural waves such a deformation did not bring expected results. We found out that certain elliptical balanced deformation with constant

cross-sectional area offered wider spectral gaps for flexural modes without much effect on torsional of longitudinal modes.

2. We developed a method to distinguish the lowest energy elastic modes in perturbed 3D waveguides. We constructed a numerical algorithm which characterizes elastic modes by their similarity to flexural, torsional and longitudinal in straight cylinder. In Figure 5 we show some of the elastic modes in slightly

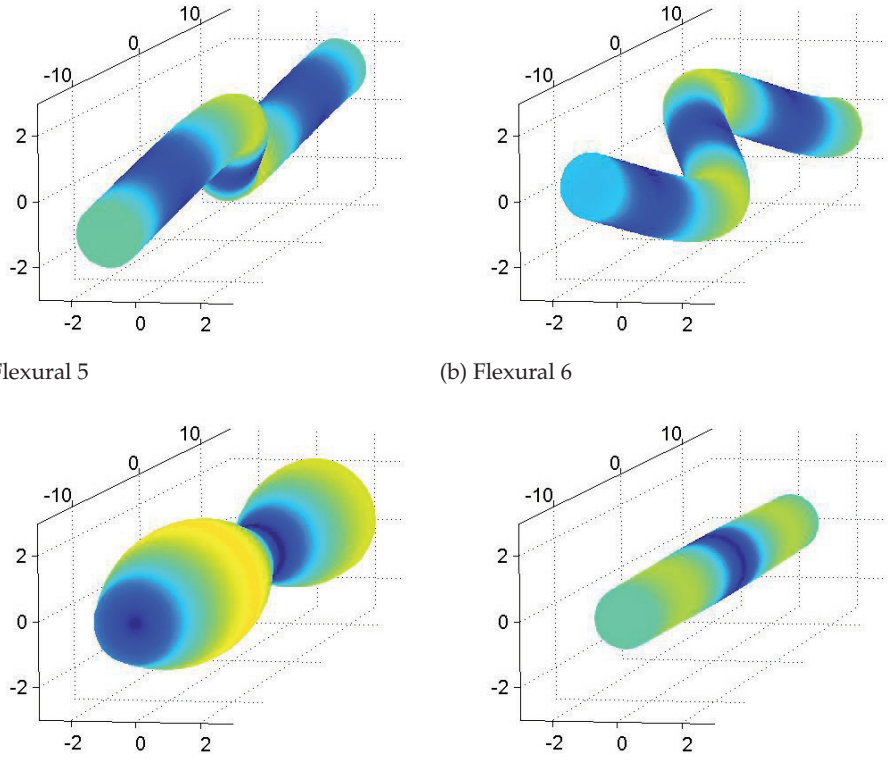


(a) Flexural 5

(b) Flexural 6

(c) Torsional 2

(d) Longitudinal 2

FIGURE 5 Four eigenmodes of different types in almost cylindrical periodical fiber with fixed wavenumber $k$. These modes passed the test which compares their characteristics to ordinary flexural, torsional and longitudinal modes in a cylinder. Coloring refers to the total displacement, i.e. absolute value $|\operatorname{Re}\vec{u}|$ of real part of the displacement field.

perturbed periodical domain, which were identified as mainly flexural, mainly torsional and mainly longitudinal by the algorithm.

3. We completed the analysis of three different 1D models for three types of elastic waves in perturbed 3D waveguide. We compared the location and width of the first band gaps calculated from 1D and 3D models. It was shown that for infinite periodic elastic waveguides the results between 1D and 3D models differed less than 1% for torsional and longitudinal modes and less than 5% for flexural modes when deformation power was 25%. In Figure 6 we show the com-

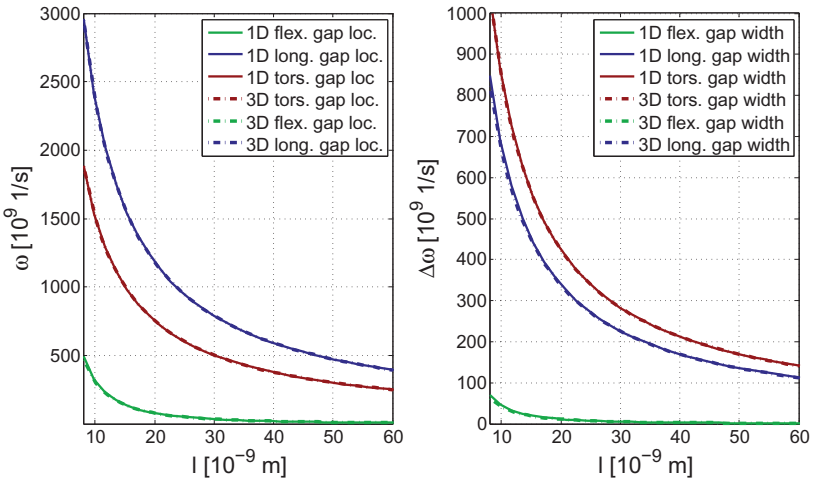


FIGURE 6 Comparison of spectral gap locations $\omega$ (left) and widths $\Delta\omega$ (right) from 1D and 3D models. Period length $l$ (horizontal axis) changes from $8nm$ to $60nm$. Strength of harmonical perturbation is 25.1% on the fiber with unperturbed diameter $D = 2nm$.

parison of 1D and 3D spectral gap locations and widths as a function of period length $l$. We also compared how the strength of perturbation affected the accuracy of approximation. There was a slight increase in error as perturbation strength $\alpha \to 50\%$. We also found out that the 1D model used for flexural waves did not give a good approximation for frequencies above the first spectral gap. The increase in error between 3D and 1D spectrum was found also for torsional and longitudinal modes, but it was decided insignificant.

4. We numerically calculated transmission coefficients $p_L(\omega)$ for longitudinal waves in 3D waveguides with short goffer. We compared transmission coefficients calculated from longitudinal 1D and 3D models and by these results we concluded that all three 1D models should give results with a good precision in comparison to 3D model. In Figure 7 there are two examples calculated for short axially symmetrical goffers containing two (left) and seven (right) periods of perturbation. Furthermore, we compared locations of cliffs in 1D transmission coefficient curves to spectra of infinite periodical fibers. We noticed that for frequencies inside a spectral gap of an infinite fiber there appears a sharp decrease in transmission probability in fibers with finite perturbations of same periodicity. The decrease is proportional to number of periods used in goffer so that as the number of periods increases, transmission coefficient functions approach the

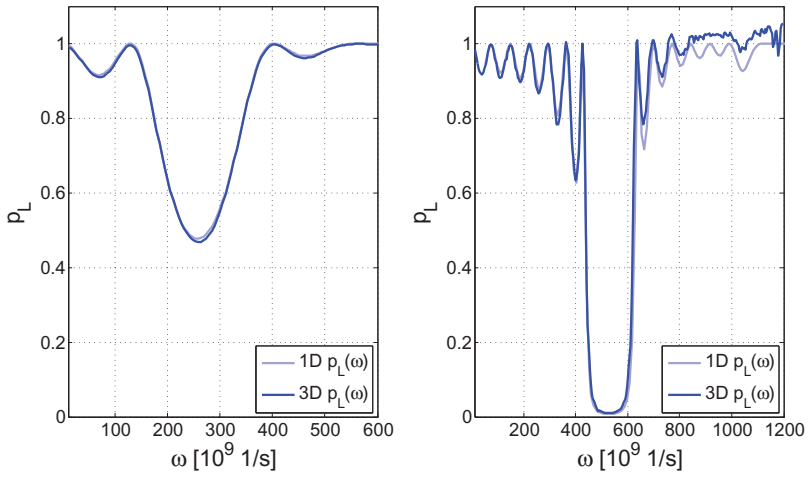


FIGURE 7 Comparison of transmission coefficients of longitudinal waves from 1D and 3D models. Left: two periods of harmonical perturbation of wavelength $l = 90nm$. Right: seven periods of harmonical type perturbation of wavelength $l = 45nm$. Diameter of the waveguide is $10nm$ and perturbation strenght $\alpha = 0.251$. We can see that 1D and 3D models give similar results.

characteristic functions of spectra of different modes. It was found that for torsional and longitudinal waves approximately 6 periods is enough while flexural waves required approximately 20 periods to obtain a 90% reduced transmission probability in the first spectral gap.

5. We calculated the thermal conductance of infinite periodical waveguides by constructing characteristic functions of frequency spectra for different elastic modes. Characteristic functions were also used to estimate how wide frequency band of different phonons should be reflected in order to obtain 90% decrease in thermal conductance at temperatures $T = 0.1 - 1K$. Reflected frequency band for such a strong decrease was calculated $0.42 - 146GHz$. By simulating single fiber designs separately we managed to find shapes that resulted into $30 - 40\%$ drop in thermal conductance by longitudinal and torsional waves through infinite periodical fibers on this particular temperature interval. The conclusion was that it is hard to design a single perturbation with such a wide reflection band without help of shape optimization.

6. It was shown with 1D models that we can create a deformation of the waveguide surface such a way that thermal conductance is reduced to $1/8^{th}$ to $1/10^{th}$ for all types of elastic waves at temperatures $T = 0.1 - 1K$. Two dif-

ferent chirped deformations are designed to reflect phonons, axi-symmetrical to reflect torsional and longitudinal waves and elliptical to reflect flexural waves. A chirped deformation is locally periodical so that the length of period is monotonically changing. In Figure 8 we show the results on thermal conductance.

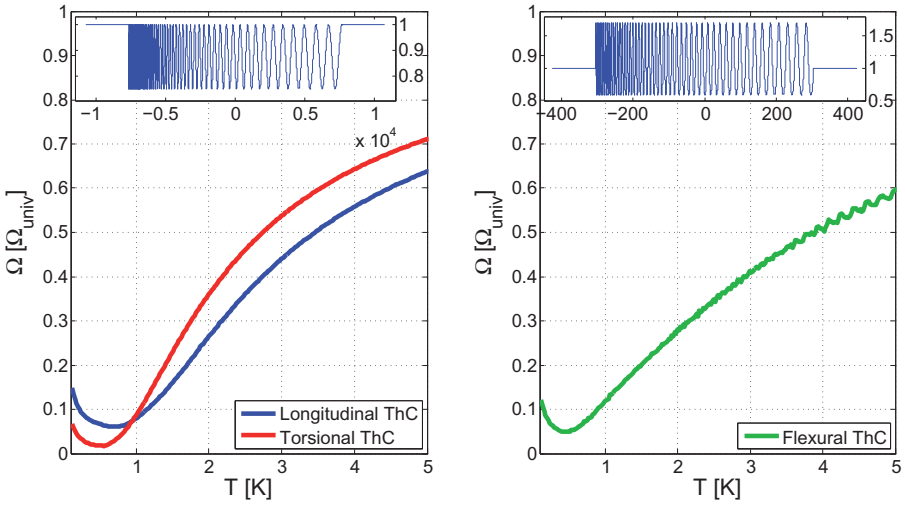


FIGURE 8 Thermal conductance by the lowest energy phonons. Left: Axi-symmetrical chirped perturbation for reducing thermal conductance by torsional and longitudinal waves. Right: Elliptical balanced deformation with constant area of cross-section for reducing thermal conductance by flexural waves. Shapes of the respective boundary curves are shown in the inset pictures.

Thermal conductance is normalized by universal quantum of thermal conductance. On the left there is an axi-symmetrical fiber with cos-type perturbation with changing period for reflecting longitudinal and torsional waves. Strength of perturbation is 25.1%. This part is $107\mu m$ long and the diameter is $10nm$. On the right is shown the boundary curve and flexural thermal conductance of elliptical chirped deformation with constant cross-sectional area. This part is $4.3\mu m$ long and diameter at the ends is again $10nm$. Strength of perturbation is 70%.

7. It was shown with 1D model for longitudinal waves that we can create the chain consisting of different perturbed parts so that each part reflects its own frequency range. Real transmission probability curve of the combined goffer can be approximated by multiplying together the curves of individual parts. In Figure 9 we show transmission probabilities of 1D longitudinal waves in two different goffers and compare their product to transmission probability through combined goffer. We noticed that if forbidden bands in two goffers interlap then there can

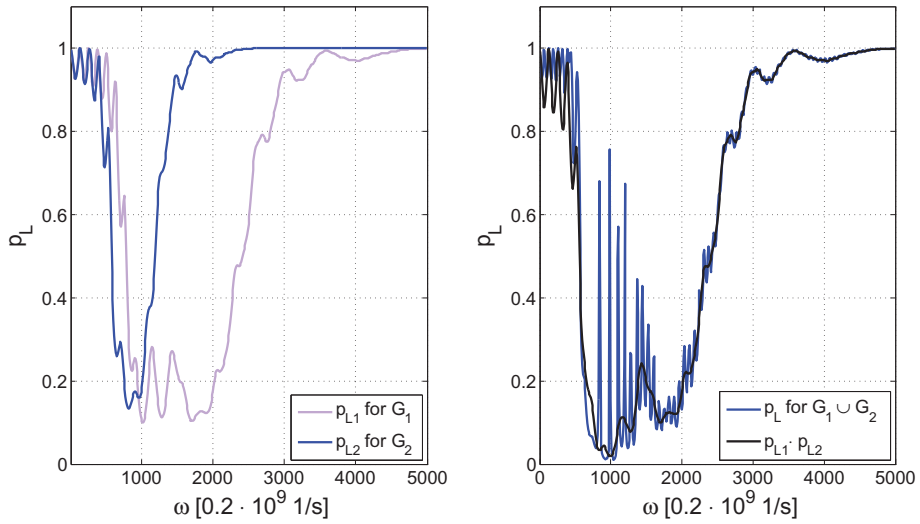


FIGURE 9 Left: Comparison of longitudinal transmission coefficients of two different linearily chirped perturbations $G_1$ and $G_2$. First period for $G_1$ is $L_{1,G_1} = 50nm$, number of periods $n_{G_1} = 10$ and chirp ratio, i.e. the ratio of the first and the last period, $C_{G_1} = 3$. Parameters for geometry for $G_2$ are $L_{1,G_2} = 100nm$, $n_{G_2} = 6$ and $C_{G_2} = 2$. Perturbation strength is $\alpha = 0.251$ and diameter $D = 10nm$. Right: Longitudinal transmission coefficients $p_L$ of combined goffer which is formed by putting perturbations $G_1$ and $G_2$ in series. We can see that it can be approximated by product curve $p_{L1} \cdot p_{L2}$, which is drawn with black.

appear resonances in the transmission probability curve of combined goffer.

# 2 THREE DIMENSIONAL MODEL OF AN ELASTIC NANOFIBER

Due to the fact that it is the phonon propagation that primarily contributes to low temperature thermal conductance in any insulating or semiconducting material it is sufficient to examine physical behavior of phonons in order to gain reliable knowledge of thermal conductance. [3, 5] In bulk materials where the dimensions are much greater than wavelength, acoustic phonons are plane waves having different polarizations. There exist only two transversal and one longitudinal acoustic modes. However if the sample is thin enough then the phonon wavelength $\lambda$ can be greater than the cross-sectional diameter $D$ of domain. We call such a construction a waveguide. It can be imagined that the presence of boundary of the waveguide allows many more than just three phonon types to propagate. In fact, shape of the waveguide dictates the nature of the waves that can propagate in the medium. If the cross-sectional shape of the waveguide is for example circular, then there can exist other phonons such as shear or torsional waves together with longitudinal and transversal ones.

When the temperature is low, $T < 10K$, phonon mean free path can become large compared to dimensions of the nanosized waveguide. This means that a phonon can propagate freely without much probability to scatter. For example for bulk crystalline silicon slightly doped with phosphor the phonon mean free path on temperature range $2K - 10K$ was measured to be greater than $300\mu m$ in [24]. It can be supposed that in pure prismatic samples the mean free path is even greater because there are no defects or impurities in the atomic lattice which can cause scattering. Because the mean free path is large, phonons cannot either annihilate or create other phonons quantum mechanically and therefore it is justifiable to use classical elastic theory to explain phonon propagation.

In order to achieve a reduced thermal conductance for a nanofiber to suit the applications we have to utilize some technique to scatter phonons. One of the possible techniques is to let the fiber cross-section approach nanoscale, and utilize the random surface roughness appearing in the production to lower the thermal conductance. This phenomenon was experimentally measured e.g. in [25]. However, lowering the fiber diameter too much does not fit in our case,

because certain structural properties are required from the fibers. Another possibility to reduce thermal conductance is to organize defects such as bubbles or clumps of other material inside the fiber and use similar analysis as in [26] for 2D models to study phonon scattering. However, changing the crystal structure in molecular level in a deliberate way can be assumed to be hard in terms of actual production of the fiber. We therefore end up to select possibly the easiest technique to manufacture, which is related to shaping the boundary of the fiber in a certain way.

The main idea of this thesis is to introduce a specific perturbation on the boundary of the fiber and examine its influence to thermal conductance with different models. The perturbation can be infinite periodical or finitely long with basically any smooth shape. Firstly, we are going to use a 3D model to numerically inspect the thermal conductance of deformed nanofibers. However, this can be very inefficient in terms of computer time because the number of mesh elements used in 3D FEM-model increases quickly when the length of domain increases. Solution to this problem is found with a remark that in low temperature in long and thin nanofiber the phonon wavelengths $\lambda$ are $\lambda > D$ where $D$ is the cross-sectional diameter of the fiber. Effectively the phonons have only one free dimension to propagate as the two transversal dimensions are quantized. Because of this, we can turn to investigate the use of different 1D models that take into account the cross-sectional shape of waveguide in simulating the propagation of the simplest phonon types in corresponding perturbed 3D waveguide.

In this chapter we begin by building a mathematical 3D model of an elastic straight fiber and examine it analytically and numerically. In the following chapters we introduce the mentioned 1D models for different elastic phonon modes in long and thin deformed fibers and calculate the effect of deformation to phonon propagation. Later we will use this information to calculate the thermal conductance of deformed waveguides. Finally with knowledge gathered by examining different deformations we give an explanation how to construct a form that has a strongly decreased thermal conductance in temperature interval $T = 0.1 - 1K$, and give some numerical values for it.

## 2.1 Elastic waves in straight cylinder

Phonons are by definition quantized lattice displacements of a solid. Because in low temperatures the wavelength of phonons is much greater than the lattice constant $d$ of the material, $\lambda \gg d$, they are assumed to be the solutions of equation describing elastic motion. This equation is called Lamé's equation $\mathcal{L}$. It can be derived from the equations of motion and energy conservation considerations as it was done for example in [17]. We intend to introduce the equation here and use it to solve the lowest energy elastic waves in a straight infinite cylinder of homogeneous material.

Let $G$ be an infinite cylinder of radius $r = 1$ lying on $z$-axis in $\mathbb{R}^3$. By Lamé-

operator we mean

$$\vec{u} \to \begin{cases} \mathcal{L}\vec{u} & \text{in } G \\ \nu \cdot \sigma(\vec{u}) & \text{on } \partial G \end{cases} \tag{18}$$

where $\vec{u} = (u_x, u_y, u_z)$, $u_i : G \to \mathbb{C}$ describes the point-wise complex-valued displacement fields in cartesian directions and where

$$\mathcal{L}\vec{u} = \mu \triangle \vec{u} + (\lambda + \mu) \nabla \operatorname{div} \vec{u} + \rho\omega^2 \vec{u} \tag{19}$$

with Lamé's elastic constants $\lambda$ and $\mu$, and the density $\rho$ depending on material of the fiber. Some other constants, e.g. $\nu$ and $E$, are generally used in literature to describe bulk properties of material. Quantity $E$ is called Young modulus and $\nu$ is Poisson ratio. These coefficients are interrelated. [17] We will be using both sets of constants through-out the text. Real number $\omega$ is the angular frequency of the displacement. As usual, we have defined the stress tensor $\sigma$ as

$$\sigma(\vec{u}) = (\lambda e_{kk} \delta_{ij} + 2\mu e_{ij})_{ij} \tag{20}$$

where in cartesian coordinates $e_{ij} = \frac{1}{2}(\partial_i u_j + \partial_j u_i)$. As an example, the corner element $\sigma_{ij}$ at $(i, j) = (x, x)$ is $\sigma_{xx} := (\lambda + 2\mu)\partial_x u_x + \lambda \partial_y u_y + \lambda \partial_z u_z$ according to definition. In definition (18) letter $\nu$ is the outward unit normal on the boundary of $G$. [18].

To restrict ourselves in physically admissible waves we examine only the periodical solutions of time-independent Lamé-operator (18) in $G$ with right hand side zero. This is the same as we would search for periodical eigensolutions $(\vec{u}, \omega)$ for equation

$$-\mu \triangle \vec{u} - (\lambda + \mu) \nabla \operatorname{div} \vec{u} = \rho\omega^2 \vec{u} \tag{21}$$

in the infinite cylinder $G$ with free boundary condition on $\partial G$. Periodical solutions $\vec{u}$ have components of a form $\vec{u}_j = U_j(x, y, z) \exp(ikz)$, $j = x, y, z$. Because of the periodicity it is possible to solve only one period $\vec{U} = (U_x, U_y, U_z)$ of the complete solution. This is done by introducing as a domain a new finite cylinder $\Pi$ of radius $r = 1$ and length $l$, and solve eigenvalue equation (21) in $\Pi$ with so called quasi-periodical boundary conditions at the circular ends $C_l$, $C_r$ of the cylinder:

$$\exp(ikl)\, \vec{U} \mid_{C_l} = \vec{U} \mid_{C_r} . \tag{22}$$

Coefficient $\exp(ikl)$ is called a phase-factor with real number $k$ and imaginary unit $i$. Free eigensolutions to (21) with boundary condition (22) describe the admissible displacement fields that have a longitudinal wavenumber $k$. We remark that wavenumber $k$ and eigenfrequencies $\omega$ can be recalculated to any unit of length $a$ with $\bar{k} = ka$, $\bar{\omega} = \omega / a$.

The eigenvalue equation (21) on a finite cylinder $\Pi$ with quasi-periodic boundary condition (22) at the ends and with free boundary condition given by $\nu \cdot \sigma(\vec{u}) = 0$ on the surface of cylinder can be easily solved numerically in order to see which kind of displacement fields there exist. Numerical implementation was done with MATLAB and COMSOL, and it will be described in more detail in the

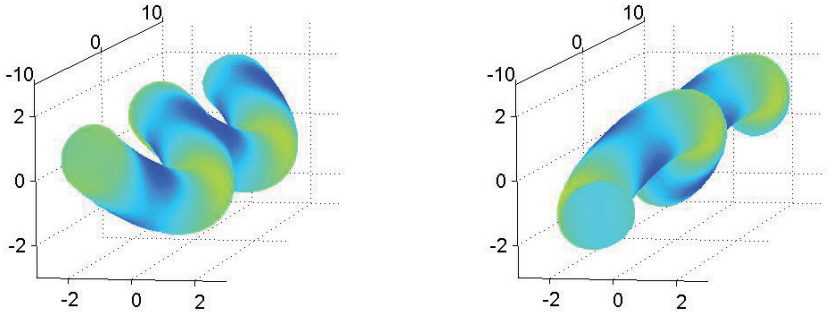


(a) Flexural 1 (b) Flexural 2

FIGURE 10 Flexural displacement modes of straight 3D cylinder. These modes are degenerated, i.e. share the same eigenfrequency, because of the symmetry of the domain. Coloring refers to the total displacement, i.e. absolute value $|\operatorname{Re}\vec{u}|$ of real part of the displacement field with dark blue designating zero.

final chapter of this text. In Figures 10 and 11 we represent numerical solutions of some of the lowest displacement modes.

In Figure 10 there are two transversal modes which have their major displacement components in orthogonal directions - these modes are called flexural. Basic distinctive mark of them from the other modes is non-existent or small displacement in $z$-direction. Because of the circular symmetry of the domain $\Pi$ these modes are coupled so they share a common eigenfrequency $\omega$. In addition, they can be mixed together resulting in rotating motion, which is also the case in the figures. If the cylindrical domain is given even an almost non-existent elliptical deformation then the mixing of these modes disappears, because they do not anymore share a common eigenfrequency.

In Figure 11 there are the other two types of displacement found at the lowest frequency range: torsional at left and longitudinal at right. Torsional modes are distinguished with rotational displacement along the cylinder boundary with the $z$-axis nearly standing still. We recognize longitudinal modes basically by cross-sectionally uniform $z$-displacement that is dominant in the solution $\vec{U}$. Color scale is the same in all of the figures. Dark blue color represents displacement $|\operatorname{Re} U(x,y,z)| \approx 0$.

## 2.2 On solving the Lamé's equation analytically in a cylinder

We have now seen a hint what kind of elastic modes there are present in the lowest energy level. These basic phonon modes can also be solved analytically from Lamé equation with help of certain physical assumptions. It was done in [18] and we will take a glance at it here.

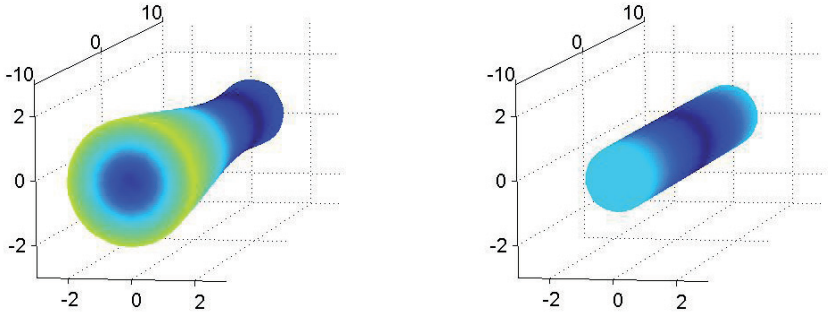


(a) Torsional (b) Longitudinal

FIGURE 11 The other two lowest energy displacement modes in a straight cylinder. Torsional mode (left) and longitudinal mode (right) are usually not degenerated, so they have a different frequencies and speeds. Coloring refers to the total displacement, i.e. absolute value $|\operatorname{Re}\vec{u}|$ of real part of the displacement field with dark blue designating zero.

Because of the circular symmetry of the cross-sections of the domain an appropriate coordinate system is cylindrical one. We first express the time-dependent displacement $\vec{u} = \vec{u}(r, \theta, z, t)$ in terms of vector and scalar potential functions $\vec{H} = (H_r, H_\theta, H_z)$ and $\Phi$, so that

$$\vec{u} = \nabla\Phi + \nabla \times \vec{H}.$$

This well-known procedure is called Helmholtz decomposition. Recalling that for cylindrical coordinates $\nabla = (\partial_r, \frac{1}{r}\partial_\theta, \partial_z)$ we conclude that components of $\vec{u}$ are then given by

$$\begin{aligned} u_r &= \frac{\partial\Phi}{\partial r} + \frac{1}{r}\frac{\partial H_z}{\partial\theta} - \frac{\partial H_\theta}{\partial z}, \\ u_\theta &= \frac{1}{r}\frac{\partial\Phi}{\partial\theta} + \frac{\partial H_z}{\partial z} - \frac{\partial H_z}{\partial r}, \\ u_z &= \frac{\partial\Phi}{\partial z} + \frac{1}{r}\frac{\partial}{\partial r}(rH_\theta) - \frac{1}{r}\frac{\partial H_r}{\partial\theta}. \end{aligned} \tag{23}$$

In order to satisfy the equations of elastic motion we insert the potentials into time-dependent Lamé's equation (24):

$$\rho\frac{\partial^2\vec{u}}{\partial t^2} = \mu\Delta\vec{u} + (\lambda + \mu)\nabla \operatorname{div}\vec{u} \tag{24}$$

With the use of vanishing of divergence of a rotor and the fact that mixed partial

derivatives are equal we end up to

$$\begin{aligned}\rho\frac{\partial^2(\nabla\Phi+\nabla\times\vec{H})}{\partial t^2} &= \mu\Delta(\nabla\Phi+\nabla\times\vec{H})+(\lambda+\mu)\nabla\,\mathrm{div}(\nabla\Phi+\nabla\times\vec{H})\\ &= \mu\Delta(\nabla\Phi+\nabla\times\vec{H})+(\lambda+\mu)\nabla(\mathrm{div}\,\nabla\Phi)\\ &= \mu\Delta(\nabla\Phi+\nabla\times\vec{H})+(\lambda+\mu)\nabla\Delta\Phi\\ &= \nabla(\mu\Delta\Phi)+\nabla\left[(\lambda+\mu)\Delta\Phi\right]+\nabla\times(\mu\Delta\vec{H})\\ &= \nabla\left[(\lambda+2\mu)\Delta\Phi\right]+\nabla\times(\mu\Delta\vec{H}).\end{aligned}$$

Rearraging of the terms gives us

$$\nabla\left[(\lambda+2\mu)\Delta\Phi-\rho\frac{\partial^2\Phi}{\partial t^2}\right]+\nabla\times\left[\mu\Delta\vec{H}-\rho\frac{\partial^2\vec{H}}{\partial t^2}\right]=0. \tag{25}$$

Clearly the equation of motion for potentials is satisfied if we suppose the potentials $\Phi$ and $\vec{H}$ to satisfy wave equations

$$\Delta\Phi=\frac{1}{c_1^2}\frac{\partial^2\Phi}{\partial t^2},\quad \Delta\vec{H}=\frac{1}{c_2^2}\frac{\partial^2\vec{H}}{\partial t^2}, \tag{26}$$

where $c_1=\sqrt{(\lambda+2\mu)/\rho}$ and $c_2=\sqrt{\mu/\rho}$. These quantities $c_1$ and $c_2$ are sometimes called dilatational and rotational wave speeds, respectively. There might exist other solutions to (25) but because solving the equations (26) results into analytical forms of flexural, torsional and longitudinal modes it is enough in perspective of this research.

Expressing the wave equations in cylindrical coordinates the scalar and vector Laplacian $\Delta$ are given by

$$\Delta\Phi=\frac{\partial^2\Phi}{\partial r^2}+\frac{1}{r}\frac{\partial\Phi}{\partial r}+\frac{1}{r^2}\frac{\partial^2\Phi}{\partial\theta^2}+\frac{\partial^2\Phi}{\partial z^2},$$

$$\Delta\vec{H}=\left(\Delta H_r-\frac{H_r}{r^2}-\frac{2}{r^2}\frac{\partial H_\theta}{\partial\theta}\right)\vec{e}_r+\left(\Delta H_\theta-\frac{H_\theta}{r^2}+\frac{2}{r^2}\frac{\partial H_r}{\partial\theta}\right)\vec{e}_\theta+\Delta H_z\vec{e}_z.$$

The stress tensor $\sigma$ must be also represented in cylindrical coordinates with

$$\begin{aligned}&e_{rr}=\frac{\partial u_r}{\partial r},\quad e_{\theta\theta}=\frac{1}{r}\frac{\partial u_\theta}{\partial\theta}+\frac{u_r}{r},\quad e_{zz}=\frac{\partial u_z}{\partial z},\\ &e_{r\theta}=\frac{1}{2}\left(\frac{1}{r}\frac{\partial u_r}{\partial\theta}+\frac{\partial u_\theta}{\partial r}-\frac{u_\theta}{r}\right),\quad e_{rz}=\frac{1}{2}\left(\frac{\partial u_z}{\partial r}+\frac{\partial u_r}{\partial z}\right),\\ &e_{\theta z}=\frac{1}{2}\left(\frac{\partial u_\theta}{\partial z}+\frac{1}{r}\frac{\partial u_z}{\partial\theta}\right),\end{aligned}$$

and the stress-free boundary condition is given by $\sigma_{rr}=\sigma_{r\theta}=\sigma_{rz}=0$ at the boundary of the cylinder $r=1$.

Assume then that the potentials are separable coordinate-wise with $z$-dependence explicitly given as exponent-function:

$$\Phi=f(r)\Theta_\phi(\theta)\exp(ikz-\omega t)),\quad H_r=h_r(r)\Theta_r(\theta)\exp(ikz-\omega t)),\ldots$$

If these solutions are substituted into wave-equations (26) we can divide out the $z$-dependence and are left with just e.g.

$$f''\Theta_\phi + \frac{1}{r}f'\Theta_\phi + \frac{1}{r^2}f\Theta''_\phi - \mathrm{k}^2 f\Theta_\phi = -\frac{\omega^2}{c_1^2}f\Theta_\phi$$

in terms of $\Phi$, where due to separability we end up solving

$$r^2\frac{f''}{f} + r\frac{f'}{f} - \left(\mathrm{k}^2 - \frac{\omega^2}{c_1^2}\right)r^2 = -\frac{\Theta''_\phi}{\Theta_\phi} = n^2. \tag{27}$$

Theta-dependence is therefore given by $\Theta_\phi = A\sin n\theta + B\cos n\theta$. This form of a solution of theta-dependence arises also for other potential components. Periodicity of the functions $\Theta_i$, $i = \phi, r, \theta, z$ is forced in order them to be well-defined, i.e. we must have $\Theta_i(\pi) = \Theta_i(-\pi)$ which implies $n \in \mathbb{Z}$. It can be also concluded afterwards that for components $\Theta_i$ only either sine or cosine term is required for describing basic elastic phonon modes: longitudinal, flexural and torsional. Therefore we choose here

$$\begin{aligned}
\Phi &= f(r)\cos n\theta\, e^{i(kz-\omega t)},\\
H_r &= h_r(r)\sin n\theta\, e^{i(kz-\omega t)},\\
H_\theta &= h_\theta(r)\cos n\theta\, e^{i(kz-\omega t)},\\
H_z &= h_z(r)\sin n\theta\, e^{i(kz-\omega t)}.
\end{aligned} \tag{28}$$

Radial dependence of the potential components can be solved with ordinary differential equations which have Bessel's $J$-functions as solutions. For example starting with $\Phi$ we can divide $r^2$ from equation (27) which results a Bessel's equation of order $n$:

$$f'' + \frac{1}{r}f' + \left(\alpha^2 - \frac{n^2}{r^2}\right)f = 0,$$

where $\alpha^2 = \omega^2/c_1^2 - k^2$. The other solutions $Y_n(\alpha r)$ have been discarded as non-physical solutions because of their singularity at $r = 0$. Therefore we write

$$f(r) = AJ_n(\alpha r). \tag{29}$$

Because of the definition of vector Laplacian the solution for $h_z$ is similar to $f(r)$, except that $\alpha^2$ would be replaced with $\beta^2 = \omega^2/c_2^2 - k^2$. So $h_z = B_3 J_n(\beta r)$.

Solving the remaining equations $h_r(r)$ and $h_\theta(r)$ will be little trickier because they are coupled, as it will be seen. By inserting potential components $H_r$ and $H_\theta$ from (28) into vector Laplacian we end up to

$$\begin{aligned}
&\frac{\mathrm{d}^2 h_r}{\mathrm{d}r^2} + \frac{1}{r}\frac{\mathrm{d}h_r}{\mathrm{d}r} + \frac{1}{r^2}(-n^2 h_r + 2nh_\theta - h_r) - k^2 h_r + \frac{\omega^2}{c_2^2}h_r = 0,\\
&\frac{\mathrm{d}^2 h_\theta}{\mathrm{d}r^2} + \frac{1}{r}\frac{\mathrm{d}h_\theta}{\mathrm{d}r} + \frac{1}{r^2}(-n^2 h_\theta + 2nh_r - h_\theta) - k^2 h_\theta + \frac{\omega^2}{c_2^2}h_\theta = 0.
\end{aligned} \tag{30}$$

Solution to equations (30) may be obtained by adding and subtracting them together. Addition gives

$$\left(\frac{\mathrm{d}^2}{\mathrm{d}r^2} + \frac{1}{r}\frac{\mathrm{d}}{\mathrm{d}r} + \beta^2 - \frac{(n-1)^2}{r^2}\right)(h_r + h_\theta) = 0,$$

which is recognaised as Bessel's equation of order $n-1$ having a solution

$$h_r + h_\theta = 2B_1 J_{n-1}(\beta r).$$

The other solution $Y_{n-1}$ is again discarded because of the singularity. Subtraction of equations (30) leads to Bessel's equation of order $n+1$:

$$\left(\frac{\mathrm{d}^2}{\mathrm{d}r^2} + \frac{1}{r}\frac{\mathrm{d}}{\mathrm{d}r} + \beta^2 - \frac{(n+1)^2}{r^2}\right)(h_r - h_\theta) = 0,$$

which has a solution $h_r - h_\theta = 2B_2 J_{n+1}(\beta r)$. Moreover, adding and subtracting the solutions leads us to

$$\begin{aligned} h_r &= B_1 J_{n-1}(\beta r) + B_2 J_{n+1}(\beta r), \\ h_\theta &= B_1 J_{n-1}(\beta r) - B_2 J_{n+1}(\beta r). \end{aligned} \tag{31}$$

Now without loss of generality we can set one of the constants to zero, say $B_1 = 0$, due to gauge invariance of Helmholtz decomposition [18]. This would result to $h_r(r) = -h_\theta(r)$. One more thing to do is to substitute the newly solved forms of potential components (28) into displacement components (23). The results are

$$\begin{aligned} u_r &= \{f' + (n/r)h_z + kh_r\}\cos n\theta\, e^{i(kz-\omega t)}, \\ u_\theta &= \{-(n/r)f + kh_r - h_z'\}\sin n\theta\, e^{i(kz-\omega t)}, \\ u_z &= \{-kf - h_r' - (n+1)h_r/r\}\cos n\theta\, e^{i(kz-\omega t)}. \end{aligned} \tag{32}$$

## 2.3 First longitudinal phonon modes in a cylinder

Due to complexity of previous analysis we calculate only longitudinal 3D modes here explicitly. Assume first that $u_\theta = 0$ and that all the derivatives $\partial/\partial\theta$ in (23) are zero. We are left only with

$$u_r = \frac{\partial\Phi}{\partial r} - \frac{\partial H_\theta}{\partial z}, \quad u_z = \frac{\partial\Phi}{\partial z} + \frac{1}{r}\frac{\partial(rH_\theta)}{\partial r}.$$

Analytic solutions for $\Phi$ and $H_\theta$ are given by (28) where $n = 0$. This setting eliminates other potential functions. Recalling the solutions (29) and (31) for $f(r)$ and $h_\theta(r)$ we can write

$$\Phi = AJ_0(\alpha r)\, e^{i(kz-\omega t)}, \quad H_\theta = -B_2 J_1(\beta r)\, e^{i(kz-\omega t)}. \tag{33}$$

First longitudinal displacements are given by

$$\begin{aligned} u_r &= B_2 \left\{ -\frac{A}{B_2}\alpha J_1(\alpha r) + ikJ_1(\beta r) \right\} e^{i(kz-\omega t)} \\ u_z &= B_2 \left\{ \frac{A}{B_2} ikJ_0(\alpha r) - \beta J_0(\beta r) \right\} e^{i(kz-\omega t)}, \end{aligned} \tag{34}$$

where

$$\frac{A}{B_2} = -\left(\frac{\beta}{\alpha}\right)^2 \frac{\beta^2 - k^2}{2k^2} \frac{J_1(\beta)}{J_1(\alpha)}.$$

We note also that as before $\alpha^2 = \omega^2/c_1^2 - k^2$ and $\beta^2 = \omega^2/c_2^2 - k^2$. For example for Silicon, $c_1 \approx 8382 m/s$ and $c_2 \approx 4705 m/s$, and we may choose for $\omega$ and $k$, $\omega = 533\,1/s$, $k = 0.07109 m^{-1}$. The choice of these numbers can be justified by solving the frequency equation for longitudinal waves or by calculating the frequency spectrum numerically. We will examine frequency spectra in the next chapter. We also note that by choosing macroscopic material constants does not alter the results, because the model used is independent of the length scale.

In order to visualize the displacement field (34) we use COMSOL graphical user face for plotting. The GUI is built on Cartesian coordinate system, hence in order to view cylindrical deformations we have to make a coordinate transformation. For presenting the deformations graphically we use "PDE, Coefficient Form (c)" setup in COMSOL with dependent variables ur, utheta and w. Static PDE solver is then configured to solve an equation system of a form ur $= u_r$, utheta $= u_\theta$, w $= u_z$, which can be obtained by setting the coefficient matrices c, a, etc. correctly. To view the displacement fields we use "Postprocessing"-tool to show deformations on a boundary plot. Parameters used are

```
Boundary: sqrt(ur^2+(x^2+y^2)*utheta^2+w^2)
Deformation:
    x: ur*cos(atan2(y,x)) -...
       -sqrt(x^2+y^2)*utheta*sin(atan2(y,x))
    y: ur*sin(atan2(y,x))+...
       +sqrt(x^2+y^2)*utheta*cos(atan2(y,x))
    z: w
```

Function atan2 refers to so called four quadrant inverse tangent. It can be defined for example with

$$\operatorname{atan2}(y,x) = 2\arctan\frac{y}{\sqrt{x^2+y^2}+x}.$$

In Figure 12 there is shown a displacement field defined by analytical solution for longitudinal wave with given elastic parameters. We immediately see by comparing it to longitudinal numerically solved eigensolution in Figure 11 that they are similar. Finally the displacement in radial direction seems to be almost nonexistent in the analytic solution. We will use this remark later.

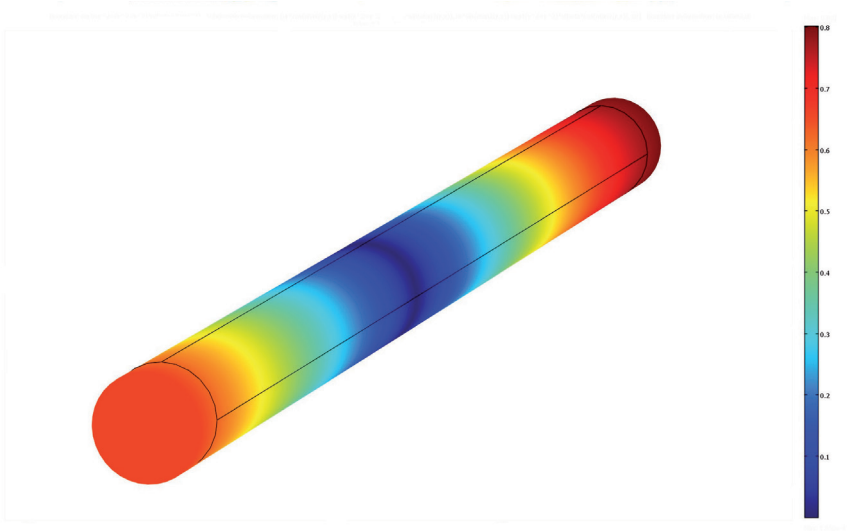


FIGURE 12 Displacement field plotted with COMSOL from analytical solution of longitudinal elastic displacement field in Silicon (Si) 3D cylinder with radius $r = 1m$ and length $l = 30m$. Coloring refers to the total displacement, i.e. absolute value $|\,\mathrm{Re}(u_r, u_\theta, u_z)|$ of real part of the displacement field.

# 3 CLASSIFICATION OF ELASTIC WAVES IN ALMOST CYLINDRICAL DOMAINS

Our intention is to affect the thermal conductance by distracting the propagation of elastic waves by introducing a refined perturbation on the boundary. However, we cannot say beforehand what exactly happens to the lowest energy phonon modes if cylindrical domain is perturbed periodically. Guiding idea is that a small perturbation should result only to a small difference to eigenvalues and phonon modes, so that the modes remain mainly the same. We can also expect that if the perturbation becomes greater but possesses enough symmetry then the phonon modes should maintain their characteristic behavior: flexural mode in cylinder should remain mainly flexural, torsional should remain mainly torsional and longitudinal should remain mainly longitudinal. We will later confirm numerically that this is in fact true when considering the first $20 - 25$ modes.

Thinking about elastic waves in a straight infinite cylinder we can try to use some of their characteristics to define wave types in perturbed periodical domains. For example starting with flexural waves we know that the main displacement component lays in $x$-$y$-plane with only little displacement on $z$-axis. Similar situation is with longitudinal waves where there is only little displacement in $x$-$y$-plane with most of it pointing to $z$-direction. Torsional modes of the lowest energy, on the other hand, have the most of their displacement near to radial boundary around $z$-axis. Assuming there is not much change for the modes under a small perturbation to the domain we can use these properties as a definition. How well the definition works numerically is seen *a posterior* from frequency spectrum: if the mode recognition procedure fails, there appear spikes on the curves.

Summarizing, in this chapter we examine the elastic modes in slightly deformed 3D waveguides by comparing their characteristics to flexural, torsional and longitudinal modes in a straight cylinder. We build an algorithm that tests these characteristics and classifies the modes into corresponding types. We also draw a frequency spectra separately for each of these modes which is later used to estimate the approximative quality of 1D models for each phonon type.

## 3.1 Frequency spectrum of periodical domain

By the symmetry of the perturbation we mean that starting from a straight finite cylinder it should look the same from both ends and it should also possess axial symmetry after the perturbation. Probably the simplest example of such a fiber is seen in Figure 13. The cylinder of radius $r$ has been axially perturbed (i.e.

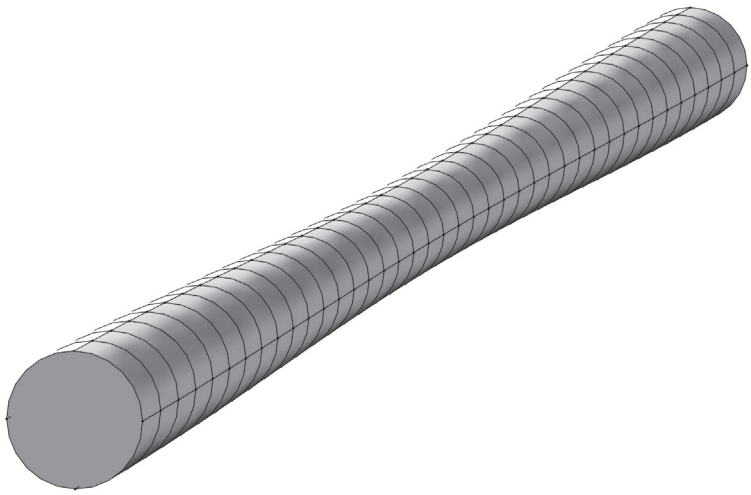

FIGURE 13 Example of the straight cylinder which has undergone a small axisymmetrical perturbation. The symmetry of the perturbation is assumed to leave phonon modes mostly intact. It can be also seen how the perturbation is implemented on the 3D domain as a linear approximation of the boundary curve.

"lathed") with one period of cos-curve with amplitude $0.25r$ so that the cross-sectional shape remains circular and the domain remains smooth along the radial boundary. The diameter of the cylinder after the perturbation at the ends is $r$ and in the middle $0.75r$. Because the theory of elasticity is independent of length scale, we do not use here any particular unit of length.

We start the classification by introducing a similar domain that was explained above with almost non-existent perturbation. The parameter $\alpha$ controlling the amplitude of the perturbation curve $\alpha\cos(z)$ is here set to $\alpha = 0.05$. More precisely, the boundary curve $B(z)$, i.e. the upper boundary of $x$-$z$-section of the domain is given with

$$B(z) = r\left\{1 + 0.5\left[1 + \operatorname{sign}\left(\frac{l}{2} - |z|\right)\right]\left[-0.5 - 0.5\cos\left(z\frac{2\pi}{l}\right)\right]\alpha\right\}, \qquad (35)$$

where $z \in [-l/2, l/2]$ and where $r$ is the radius and $l$ is the length of unperturbed cylinder. The periodical domain $\Pi$ is generated with help of MATLAB functions circ2 and extrude.

First a circle of radius $r$ is drawn on $x$-$y$-plane. Then function $B = B(z)$ is evaluated in 40 constantly separated points in $[-l/2, l/2]$. These 40 values of $B(z)$ are used as a piece-wise scaling factor for extruding the circle from $z = 0$ to $z = l$ in $\mathbb{R}^3$. Finally the domain is moved backwards on the $z$-axis so that circular ends lay at $z = -l/2$ and $z = l/2$. Extruding the circle in piece-wise linear fashion along values from a smooth function doesn't necessarily give a smooth surface in MATLAB. However there will not be any sharp edges or spikes and therefore we can neglect the effects of boundary roughness. Final remark about the domain is that the circular ends should share a same radius for definition of quasi-periodic boundary condition. If this is not the case then COMSOL uses a linear transformations to deform the other end to meet with the other. [38] In such a case the quasi-periodic model would not match with an infinite periodically perturbed almost cylindrical fiber, but instead an exponential infinite horn profile as a result of stacked linear transformations.

The equation to be solved in domain $\Pi$ is Lamé's eigenvalue equation

$$-\mu \triangle \vec{u} - (\lambda + \mu) \nabla \operatorname{div} \vec{u} = \rho \omega^2 \vec{u} \tag{36}$$

with quasi-periodical boundary condition

$$\exp(ikl)\vec{u}|_{C_l} = \vec{u}|_{C_r} \tag{37}$$

at the circular ends of the domain. Along the radial boundary or $\Pi$ we put

$$-\nu \cdot C \nabla \vec{u} = 0, \tag{38}$$

where $\nu$ is the unit normal vector of the boundary and $C$ is stiffness matrix. This is called a free boundary condition. In the boundary condition (37) the parameter $k$ goes over the zone $[0, 2\pi/l]$ with predefined steps of constant width. The resolution is usually 100 steps/zone in the figures presented in this text. For every $k$ some given number $n$ of smallest eigenfrequencies and their corresponding eigenmodes are calculated, and the eigenfrequencies are stored in a matrix of size $n \times 100$. Finally the rows of the matrix are plotted one by one in a same figure regardless of what kind of mode the values represent. More precisely, what we are plotting is actually functions $f_j$ such that

$$f_j := f_j(k) = \min\left( \{\, \omega(k) \,\} / \cup_{i=1}^{j-1} \{\, f_i(k) \,\} \right),$$

where $\{\, \omega(k) \,\}$ represents the true unordered eigenfrequency spectrum for given $k$.

As a result we get an eigenfrequency graph shown in Figure 14. The value of $k$ is let to sweep over the larger range $[-0.1\pi/l, 2.1\pi/l]$ in order to visualize the periodical structure of frequency spectrum. At $k = \pi/l$ is located so called Brillouin zone edge of the periodical structure, which is shown in the figure by dashed vertical line. We used nanometer scale dimensions in order to find out the frequency range for the first acoustic phonons. We can immediately see from the scales that the lowest phonons have frequencies up to $40GHz$ in a periodical fiber

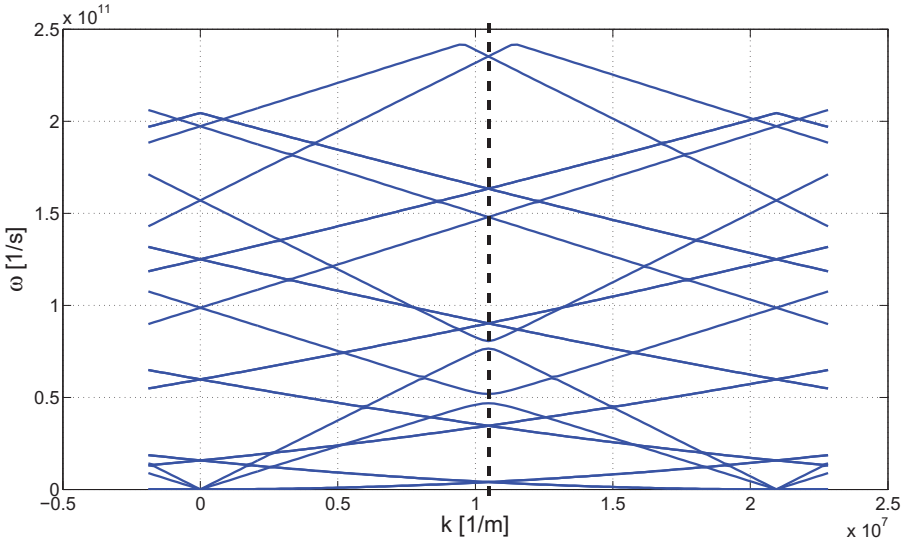


FIGURE 14 Frequency spectrum of almost cylindrical 3D silicon fiber. Parameters for geometry are length $l = 300nm$, diameter $D = 20nm$ and the strength of cos-type perturbation $\alpha = 0.05$. Black dashed line denotes the Brillouin zone edge. We can notice small gaps in the spectrum to appear near the Brillouin zone edge at $\omega \approx 0.5 \cdot 10^{11}\, 1/s$ and $\omega \approx 0.8 \cdot 10^{11}\, 1/s$.

with periodicity length $l = 300nm$ and diameter $D = 20nm$. The elastic material parameters are for silicon (Si) and they are $E = 1.31 \cdot 10^{11} Pa$, $\nu = 0.27$ and $\rho = 2330 Kg/m^3$. Finally we conclude that the resulting frequency spectrum is quite hard to interpret without more information about the corresponding modes.

## 3.2 Defining algorithm for the lowest elastic modes

In order to categorize the elastic modes they are put through an algorithm that evaluates the displacements in some points and names the modes according to their similarities with elastic modes in a straight cylinder. This algorithm serves as a definition for names of elastic modes in almost cylindrical fibers. Consequently while solving the eigenvalue equation (36) for every $k$ large enough all the eigenmodes corresponding to eigenvalues are analyzed with the next procedure:

- Interpolate the value for displacement vector $(u, v, w)$ in some predefined point $p_1$ on $z$-axis.
- If the sum $|u(p_1)| + |v(p_1)|$ of complex norms is large, i.e. close to maximal

total displacement of the solution, then the mode will be called *flexural*.

- If the mode is not flexural and the sum $|u(p_1)| + |v(p_1)|$ is small and $|w(p_1)|$ is large in comparison to maximal total displacement of the solution, then the mode will be called *longitudinal*.
- If the mode is neither flexural nor longitudinal and the sum of norms is small in comparison to maximal total displacement,

  $$|u(p_1)| + |v(p_1)| + |w(p_1)| < \epsilon,$$

  then we interpret that point $p_1$ suggests mode being torsional and the algorithm is run for a different point $p_2$. When enough points $p_j$ suggest that mode is torsional the procedure is ended and the mode will be called *torsional*.
- If the mode being analyzed did not meet any of these conditions for point $p_1$, then start from the beginning with a different point $p_2$.

Just to mention, it is somewhat challenging to find a small number of general test points $p_i$ which would allow the identifying procedure to work for large collection of different boundary shapes and values of $k$. Increasing the number of test points would of course result to increased calculation time, so therefore they should be chosen with care. The adjectives large and small need not be given exact values here as they can be defined separately for different domain shapes. For values of $k \approx 0$ this procedure may fail because the elastic modes at $k = 0$ are standing waves. For such solutions there are one or more discretely located points $z \in [-l/2, l/2]$ such that $|u(0,0,z)| + |v(0,0,z)| + |w(0,0,z)| \approx 0$ where it is impossible to say which mode it is in question. It also seems in this case that the modes can be coupled with each other so that the intuitive mode characteristics are harder to see. However this problem can be avoided if we define that the modes near $k = 0$ will be called the same that they are called for small $k > 0$. This is done by keeping the same ordering of names for eigenvalues near $k \approx 0$.

Whether the procedure works or not with given parameters it can be decided *a posterior* by combining the flexural, torsional and longitudinal frequency spectrums together and comparing the resulting picture to original frequency spectrum with unclassified modes. Differences in figures would be easily noticeable as spikes or discontinuities. For clarification we use same color codes for each of these modes: flexural will be printed with green, torsional with red and longitudinal with blue through out the text.

## 3.3 Flexural waves

Let us look into more detail of how the algorithm works for flexural waves. Say that we have calculated the frequency spectrum and corresponding eigenmodes from first up to $24^{th}$ modes. For each eigenmode we use COMSOL/MATLAB build-in interpolation function postinterp to evaluate the displacement field

$(u, v, w)$ at point $p_1 = (0, 0, l/4)$. The adjective large in the definition of algorithm is set to $0.1 \cdot D$, where $D$ is the diameter of the periodicity cell end. Deciding rule for flexural wave is therefore

$$|u(p_1)| + |v(p_1)| > 0.1 \cdot D. \tag{39}$$

If no result was found at $p_1$ then procedure is carried again one at a time for $p_j = (0, 0, (2 - 1/j)l/4)$, $j = 2, \ldots, 10$ until a solution is found.

In Figure 15 we represent the eigenfrequencies that passed the flexural test. We can immediately see that there is no visible spectral gaps present or they are

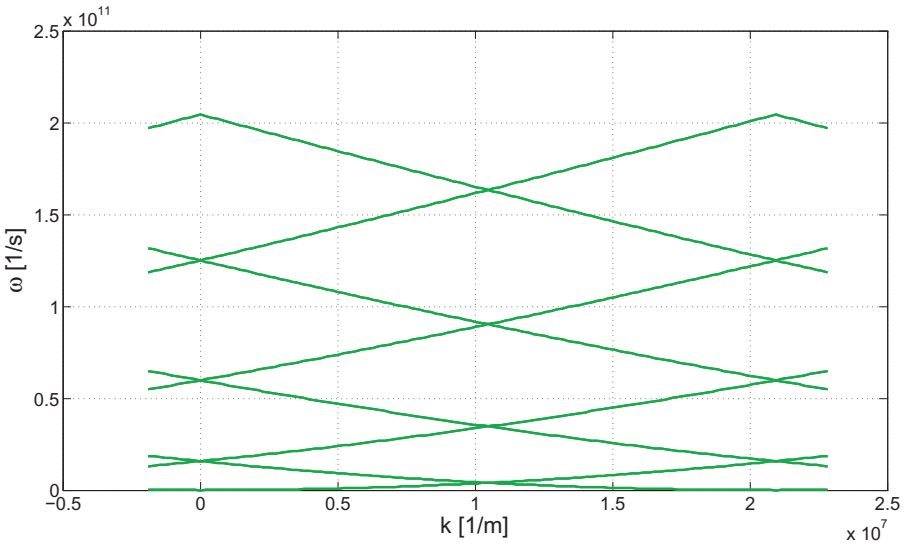


FIGURE 15 Frequency spectrum of eigenmodes with characteristics of flexural waves in almost cylindrical 3D fiber. These curves were identified from the spectrum with the algorithm that compares the characteristics of the corresponding modes to ordinary flexural modes in a straight cylinder. Parameters for geometry are length $l = 300nm$, diameter $D = 20nm$ and the strength of cos-type perturbation $\alpha = 0.05$.

small enough not to be seen within this resolution. Quick examination at the picture reveals that the algorithm should have worked in this case: there are no discontinuities or spikes on the curves. Also $\omega \propto k^2$ as it should be for flexural modes in a straight cylinder. [18] In order to be sure what kind of modes in fact passed the procedure the modes can be plotted as it is done in Figure 16. Coloring shows the absolute displacement, i.e. $|\operatorname{Re} \vec{u}|$ with dark blue corresponding to value zero. Clearly all of these modes have dominant displacement component in $x$-$y$-direction and therefore they succeed in being intuitively flexural.

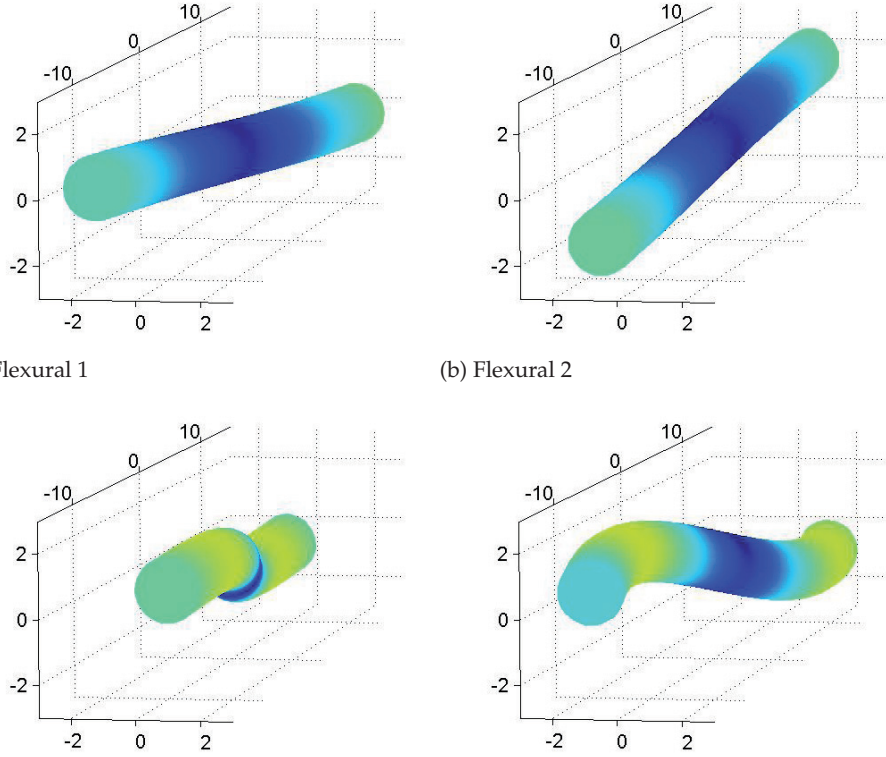


(a) Flexural 1

(b) Flexural 2

(c) Flexural 3

(d) Flexural 4

FIGURE 16 First four eigenmodes of almost cylindrical periodical fiber for fixed $k$. These modes passed the test which compares displacements to flexural wave displacements in a cylinder and are therefore called flexural as well. Coloring refers to absolute value of the real part of displacement field.

There are a couple of things to be noted about flexural waves. First, because of axial symmetry of the domain flexural modes are two-fold degenerated. It means that an eigenvalue corresponds to two different eigenmodes that have major displacement vectors to different directions in $x$-$y$-plane. Degenerated modes can be also coupled so that, loosely speaking, there is a minor component of other mode within the other. Eigenmodes are not necessarily orthogonal. This results to elliptically rotating flexural vibration, which can be seen from eigenmode animations in COMSOL. If the axial symmetry is relaxed, for example by squeezing even a small elliptical deformation to the original cylinder, then the degeneracy is relaxed as well as is the coupling of flexural modes. The final conclusion of this section is that the classifying algorithm works for flexural waves.

## 3.4 Torsional waves

We now turn to examine higher energy modes of the low frequency spectrum. In Figure 17 we present the eigenfrequencies that passed the torsional test. It was required in the algorithm that the sum of norms $|u(p_j)| + |v(p_j)| + |w(p_j)|$ must be smaller than $0.1 \cdot D$ for 5 different points $p_j = (0, 0, (2 - 1/j)l/4)$, $1 \leq j \leq 10$, along $z$-axis. Theory predicts (see [18]) that for torsional waves in straight cylin-

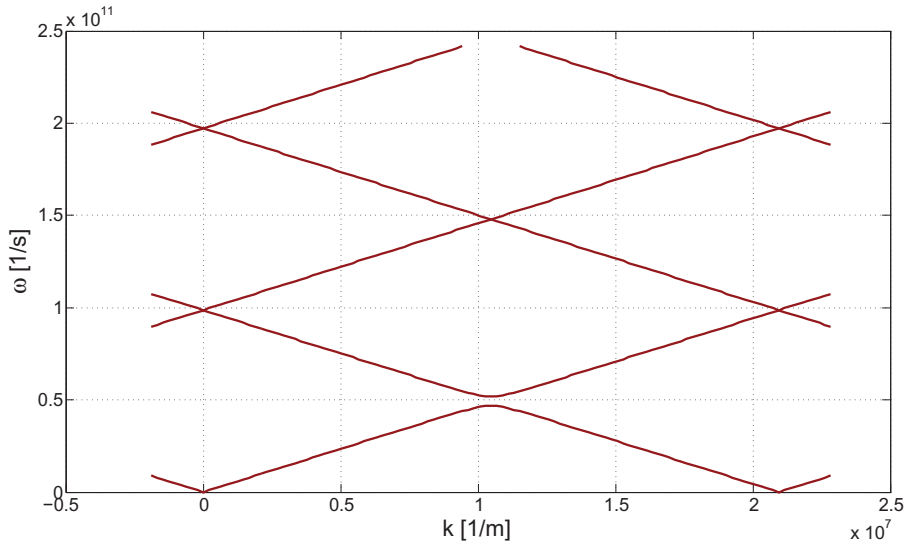


FIGURE 17 Frequency spectrum of eigenmodes with characteristics of torsional waves in almost cylindrical 3D fiber. These curves were identified from the spectrum with the algorithm that compares the characteristics of the corresponding modes to ordinary torsional modes in a straight cylinder. Parameters for geometry are length $l = 300nm$, diameter $D = 20nm$ and the strength of cos-type perturbation $\alpha = 0.05$.

der there is a linear dependence between wavenumber and frequency, $\omega \propto k$. That is also correct for small values of $k$ in almost cylindrical domains according to our results. Another remark from the Figure 17 is that for larger $k$, near the center of the zone, linearity seems to break down and there appears a remarkably wide spectral gap at $\omega \approx 0.5 \cdot 10^{11}\, 1/s$. As we remember, amplitude of the perturbation is only 5% of the original cylinder. Existence of a spectral gap for torsional waves means that such waves with frequencies lying inside a gap do not exist in such periodical fiber. Due to this it is possible to hypothesize that transmission probability of torsional waves through a finitely long wire would

be easily reduced, if the wire undergoes a deformation of a number of periods of cos-type perturbation.

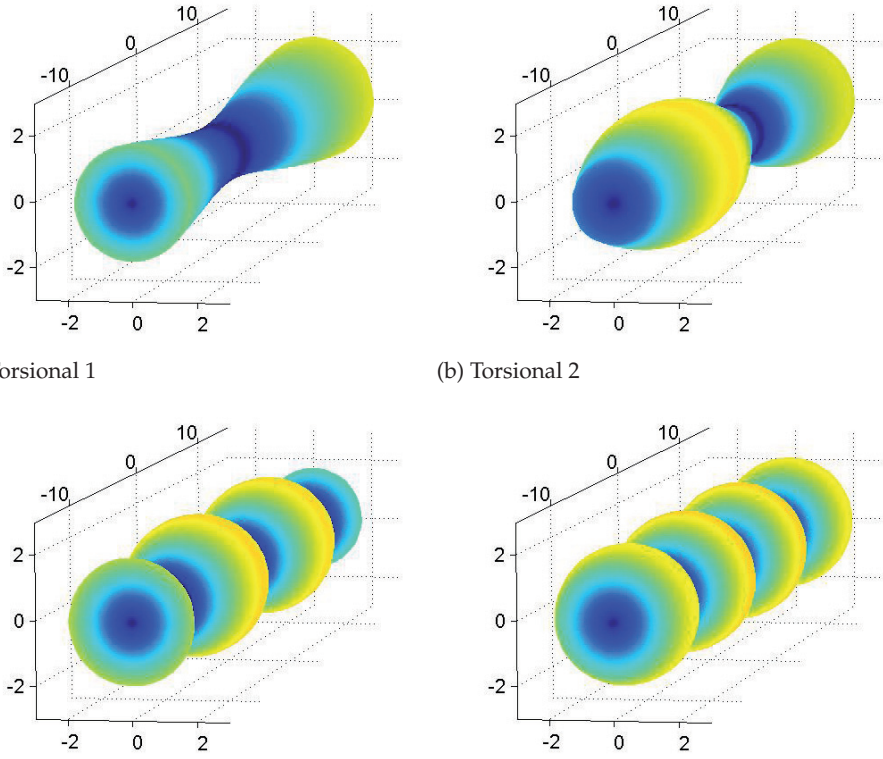


(a) Torsional 1

(b) Torsional 2

(c) Torsional 3

(d) Torsional 4

FIGURE 18 Eigenmode numbers 7, 11, 17 and 20 of almost cylindrical periodical fiber for fixed $k$. These modes passed the test which compares displacements to torsional waves in a cylinder and are therefore called torsional. Coloring refers to absolute value of the real part of displacement field.

In Figure 18 we present the modes that correspond to the four lowest eigenfrequency curves in Figure 17. Coloring of the solutions shows that the dark blue areas, where displacement is close to zero, lay on $z$-axis. This meets the characteristic requirements of torsional waves. In addition, there is considerably large displacement in radial direction which is located where the rotational displacement is large as well. Relative strengths of radial and rotational displacement in torsional modes are controlled by material parameters $\lambda$, $\mu$ and $\rho$ in Lamé's equation. We can conclude that clearly the identifying algorithm works for torsional modes.

## 3.5 Longitudinal waves

In Figure 19 there are presented the first longitudinal eigenfrequencies. By the definition, corresponding modes of these frequencies were identified to be almost longitudinal by the algorithm. Distinctive mark of longitudinal modes is nearly

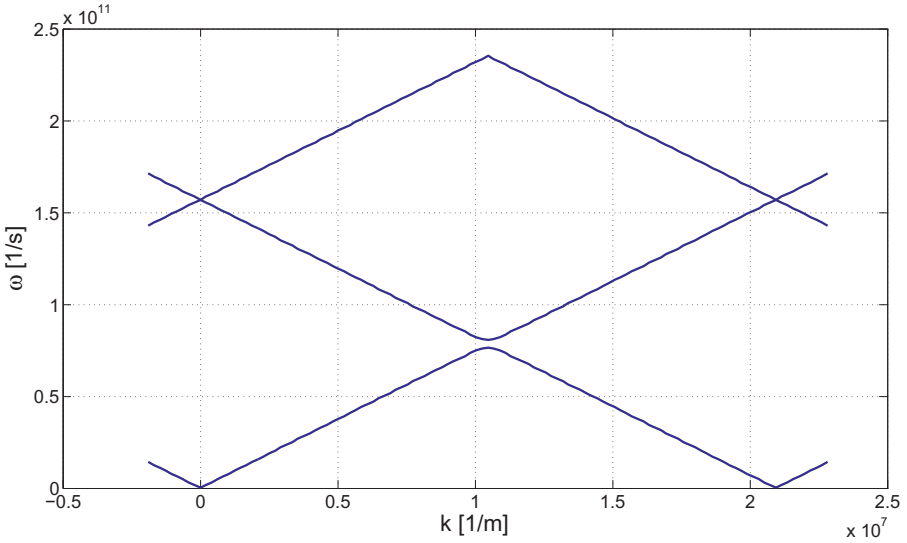


FIGURE 19 Frequency spectrum of eigenmodes with characteristics of longitudinal waves in almost cylindrical 3D fiber. These curves were identified from the spectrum with the algorithm that compares the characteristics of the corresponding modes to ordinary longitudinal modes in a straight cylinder. Parameters for geometry are length $l = 300nm$, diameter $D = 20nm$ and the strength of cos-type perturbation $\alpha = 0.05$.

constant $z$-displacement in every transversal cross-section of the domain. It was required that in any of the points $p_j$ the norm $|w(p_j)| > 0.1 \cdot D$ and the sum of norms $|u(p_j)| + |v(p_j)| < 0.1 \cdot D$ so that a mode would be named as longitudinal.

According to theory longitudinal waves in a cylinder have frequency proportional to wavenumber which is evidently correct for waves with small wavenumbers $k$ in perturbed cylinders. Like before, we can spot a spectral gap of approximately similar width as for torsional waves at the crossing of first and second eigenfrequency curves. Spectral gap is located around $\omega \approx 0.8 \cdot 10^{11}\, 1/s$. We may again hypothesize that transmission coefficients of longitudinal waves would be easily reactive to radial harmonic perturbation of the domain also in finite fibers.

Finally, just to complete the survey of lowest eigenmodes, we show the first three longitudinal modes in Figure 20. These modes indeed seem to have a cross-sectionally constant $z$-displacement and only a small radial displacement along the whole domain. Dark blue color again corresponds to $|\operatorname{Re}\vec{u}| = 0$.

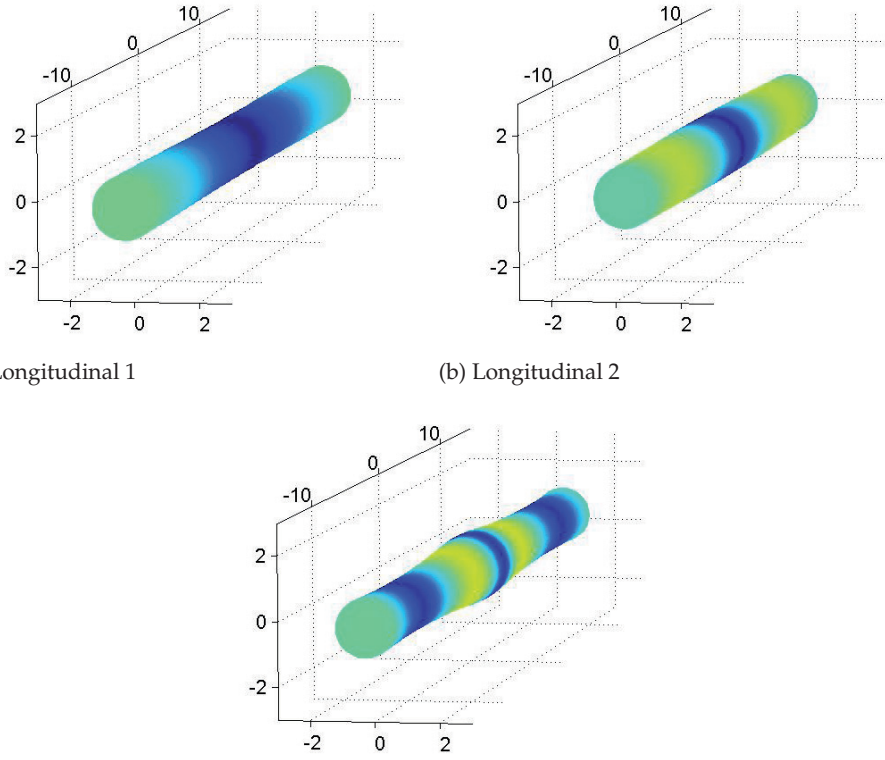


(a) Longitudinal 1

(b) Longitudinal 2

(c) Longitudinal 3

FIGURE 20 Eigenmode numbers 10, 16 and 23 of almost cylindrical periodical fiber for fixed $k$. These modes passed the test which compares displacements to longitudinal waves in a cylinder and are therefore called longitudinal as well. Coloring refers to absolute value of the real part of displacement field.

# 4 ONE DIMENSIONAL MODELS OF ELASTIC WAVES

We have learned in previous chapters that are three kinds of elastic eigenmodes in almost cylindrical fibers at the lowest energy level: flexural, longitudinal and torsional. Simulating these modes numerically in a 3D model is challenging in terms of computer time. Solving and identifying the modes from frequency spectrum can take even several hours depending on the resolution and mesh size. However, as we have seen from the figures representing eigenmodes the fields are almost one dimensional having dominant displacement in only one direction. For longitudinal modes this direction is $z$-axis, for two flexural modes it is the two transversal axes and for torsional mode the direction is the angular axis $\theta$ in cylindrical coordinate system. This remark gives us a reason to believe that suitable 1D models can give a good approximation to 3D frequency spectrum. One dimensional models would also be many times faster to solve numerically and longer fiber models could also be used in simulations.

In this chapter we are going to describe three different 1D models and give some results of how well they approximate 3D frequency spectrum. We will compare the width and location of first spectral gaps from 1D and 3D frequency spectrums. It will be seen at the end that all of the lowest 3D elastic modes can be approximated very well by the 1D models with inaccuracy usually less than 1%. The idea is to find three ordinary differential equations defined on 1D domain $[-l/2, l/2]$ that would approximatively describe the physics of each of the modes. The equations would operate as a Lamé's equation (21) in 1D domain. Such way they could be used for both finding a frequency spectrum of almost cylindrical periodical fibers and later finding so called scattering amplitudes $s_{jp}$ for different phonon modes in finite fibers. Therefore we will also find the harmonic wave solutions for each of these models in a straight cylinder. Let us start with flexural waves.

## 4.1 Flexural waves

The governing 1D equation for flexural waves in thin rods is developed in [18] and we explain it here carefully. Consider a differential element of thin rod such as one in Figure 21 undergoing a transversal motion into $x$-direction. Several

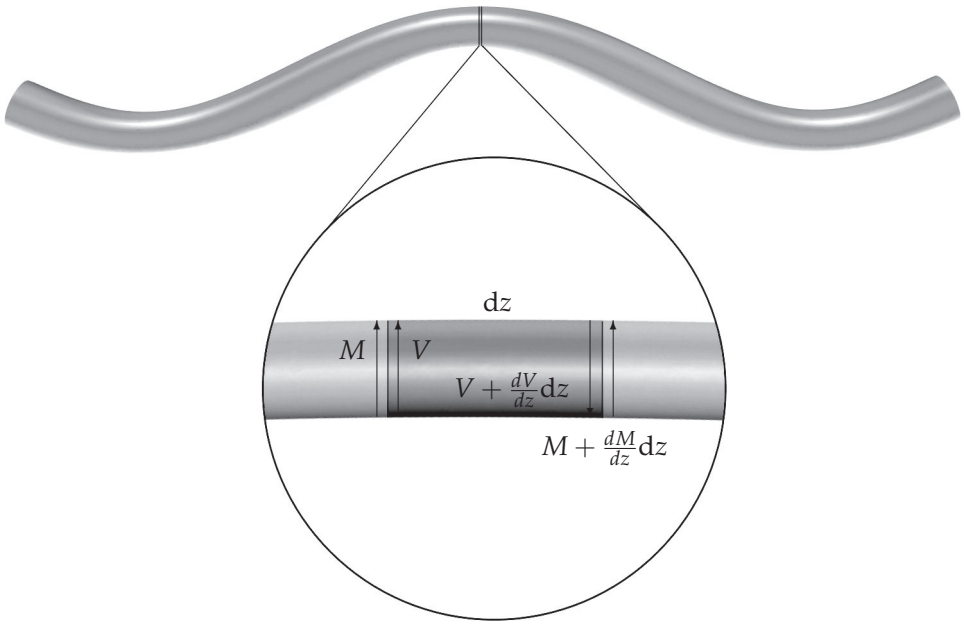


FIGURE 21 Differential element $\mathrm{d}z$ of thin almost cylindrical fiber under transversal motion. Bending moment $M = M(z)$ and shear force $V = V(z)$ are shown by vectors pointing to their respective directions. Coordinate parameter $z$ refers to the cross-section of the fiber perpendicular to its neutral axis.

forces are acting on the element $\mathrm{d}z$, but in this approximation we notice only the bending moment $M = M(z)$ and shear force $V = V(z)$. We take an assumption that perpendicular plane cross-sections of the fiber remain plane and perpendicular to neutral axis of the fiber. This is a basic postulate in the Bernoulli-Euler beam theory. The second derivative approximation of bending moment $M = M(z)$ at point $z$ is

$$\frac{\partial^2 u(z)}{\partial z^2} = -\frac{M(z)}{EI(z)},$$

where $I(z)$ is the moment of inertia and $E$ Young modulus. Denominator on the right side is sometimes called a *bending stiffness*. Displacement of neutral axis of the fiber in vertical direction for differential element at $z$ is given by

$$-V(z) + \left( V(z) + \frac{\partial V(z)}{\partial z}\,\mathrm{d}z \right) = \rho A(z) \frac{\partial^2 u(z,t)}{\partial t^2}\,\mathrm{d}z\,, \tag{40}$$

where $A(z)$ is the cross-sectional area of the element, $V(z)$ is the shear force on vertical direction and $\rho$ the density as usual. For elliptical or circular cross-sections area $A(z)$ can be expressed with $A(z) = \pi B_x(z)B_y(z)$ where $B_x(z)$ and $B_y(z)$ are the boundary curves in $x$-$z$ and $y$-$z$-plane. Moment of inertia $I(z)$ for the differential cross-section $\mathrm{d}z$ can be expressed with a same formula for circular and elliptical disc shapes: $I(z) = \pi B_x(z)B_y^3(z)/4$. We can also exchange the time derivation with $\partial/\partial t \to i\omega$ in order to relax the model to static scheme.

We may use $V(z) = \partial M(z)/\partial z$ for the moment-force relation neglecting the rotational-inertia changes arising from changing cross-section. This assumption limits the application of 1D model to only low frequency waves where deformation in $y$-direction is small. Moreover, the cross-section of the fiber must be symmetrical in $x$-$y$-plane or otherwise one must be prepared to consider coupled flexural-torsional waves (e.g., see [18]).

Substitution of the above equations into (40) gives

$$\frac{\partial^2}{\partial z^2}\left(B_x(z)B_y(z)^3\frac{\partial^2 u(z)}{\partial z^2}\right) = \frac{4\rho}{E}B_x(z)B_y(z)\omega^2 u(z). \tag{41}$$

Equation (41) can be solved numerically in MATLAB by separating the equation into two coupled second order equations with a substitution $v = B_x B_y^3 \partial^2 u/\partial z^2$. The equation becomes

$$\begin{cases} \dfrac{\partial^2}{\partial z^2}v(z) - \dfrac{4\rho}{E}B_x(z)B_y(z)\omega^2 u(z) = 0, \quad z \in ]-l/2, l/2[, \\ \dfrac{\partial^2}{\partial z^2}u(z) - \dfrac{1}{B_x(z)B_y(z)^3}v(z) = 0, \quad z \in ]-l/2, l/2[. \end{cases}$$

For a straight cylinder where $B_x = B_y \equiv a$, where $a > 0$ is a constant, the harmonic wave solution of (41) is of a form $u(z) = A\exp(i\zeta z)$. With wavenumber $\zeta$ solved the solutions take a form

$$u(z) = A\exp\left(\pm i\sqrt{\sqrt{\frac{4\rho}{E}}\frac{\omega}{a}}\,z\right), \quad \text{or} \quad u(z) = A\exp\left(\pm\sqrt{\sqrt{\frac{4\rho}{E}}\frac{\omega}{a}}\,z\right), \tag{42}$$

where only the first two give a propagating wave field. The latter two are expected to play a role in forced or transient elastic problems and are therefore neglected here.

## 4.2 Torsional waves

Let us then consider a differential element of almost cylindrical fiber subjected to different torques at the ends of the element as shown in Figure 22. The guide lines of analysis were presented for straight cylinders in [18]. By adding the torques we end up to equation of motion for element, which is

$$-T(z) + \left(T(z) + \frac{\partial T(z)}{\partial z}\,\mathrm{d}z\right) = \rho I(z)\,\mathrm{d}z\,\frac{\partial^2 u_\theta}{\partial t^2}. \tag{43}$$

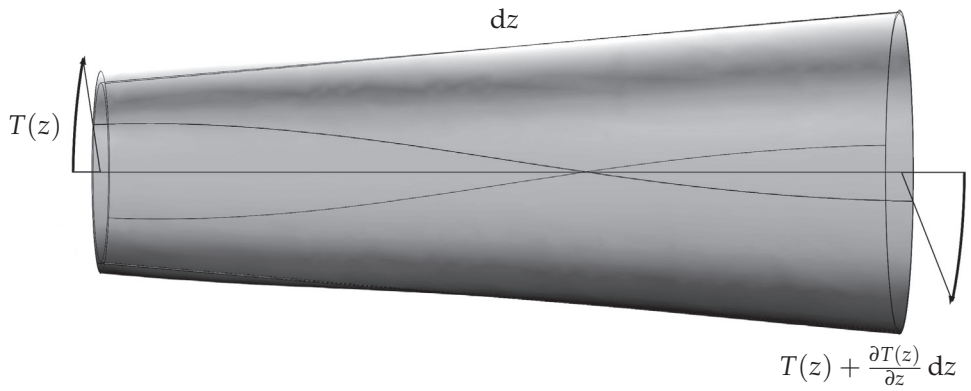


FIGURE 22 Differential element $\mathrm{d}z$ of thin almost cylindrical fiber under torsional motion. Vectors $T(z)$ and $T(z) + \frac{\partial T(z)}{\partial z}\,\mathrm{d}z$ at the ends of block resemble different torques in effect.

We substitute $T(z) = C(z)\partial u_\theta/\partial z$ into the equation (43). Function $C(z)$ is called torsional rigidity and for domains with circular cross-section it is given by

$$C(z) = \mu\pi B_x^4(z)/2.$$

For elliptical cross-sections

$$C(z) = \mu\pi \frac{B_x^3(z)B_y^3(z)}{B_x^2(z) + B_y^2(z)}, \tag{44}$$

where $B_x$ and $B_y$ are again the boundary curves of the domain in $x$ and $y$ - direction. We immediately see that if $B_x = B_y$ then the torsional rigidity equation for elliptical cross-sections yields the one for circular. Therefore we can use equation (44) in 1D model, if the 3D domain has circular or elliptical cross-section. In the rotational equation of motion (43) $I(z)$ is the polar moment of inertia, and it is given by

$$I(z) = \frac{\pi}{4} B_x(z)B_y(z)\left(B_x^2(z) + B_y^2(z)\right).$$

After exchanging the time-derivation from (43) with $\partial/\partial t \to i\omega$ we end up to following static equation:

$$\frac{\partial}{\partial z}\left[\frac{B_x^3(z)B_y^3(z)}{B_x^2(z) + B_y^2(z)}\frac{\partial u_\theta(z)}{\partial z}\right] = \frac{\rho}{4\mu} B_x(z)B_y(z)(B_x^2(z) + B_y^2(z))\omega^2 u_\theta(z). \tag{45}$$

Equation (45) will be used to approximate torsional waves in circular or elliptical fibers. We can find the harmonic wave solutions to it by setting the boundary

curves $B_x$ and $B_y$ identically to 1. We immediately see that it reduces to ordinary wave equation with solutions

$$u(z) = A \exp\left(\pm i \sqrt{\frac{\rho}{\mu}} \omega \, z\right). \tag{46}$$

It will be observed in the proceeding sections that this model gives a very good approximation to real 3D torsional modes with error less than 1% on a wide parameter range. Before going into that we introduce an approximation for longitudinal modes.

## 4.3 Longitudinal waves

For longitudinal waves the suitable 1D approximation is done in analogous way to torsional case except that the physical coefficients in the equations will be different. [18] Consider a differential element for longitudinal motion as shown in Figure 23. We expect that the only affecting field on the cross-section at $z$

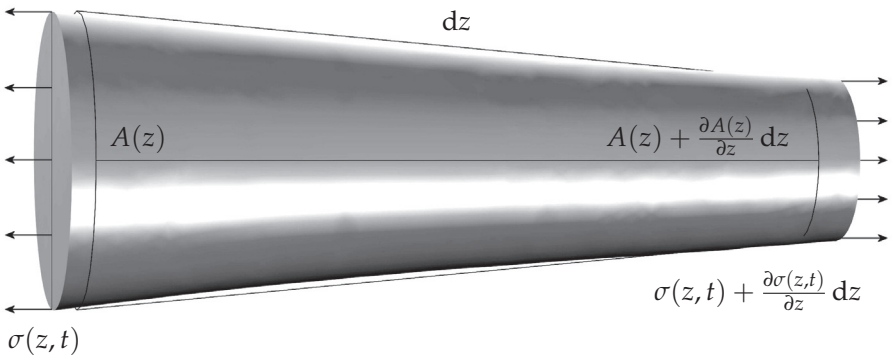


FIGURE 23 Differential element $\mathrm{d}z$ of thin almost cylindrical fiber under longitudinal motion. Vectors $\sigma(z,t)$ and $\sigma(z,t) + \frac{\partial \sigma(z,t)}{\partial z}\,\mathrm{d}z$ at the ends of block resemble different dynamic stress fields in effect. Wire-frame shows the form of the element in stress-free situation.

is dynamically changing stress field $\sigma(x,t)$. Writing down the forces $F(z) = A(z)\sigma(z,t)$ at both ends leads to an equation of longitudinal motion for differential element with variable cross-sectional area. Coefficient $A(z)$ is the area of cross-section. By adding the forces we get

$$-\sigma A + \left(\sigma + \frac{\partial \sigma}{\partial z}\,\mathrm{d}z\right)\left(A + \frac{\partial A}{\partial z}\,\mathrm{d}z\right) = \frac{1}{2}\rho\left(A + \left(A + \frac{\partial A}{\partial z}\,\mathrm{d}z\right)\right)\mathrm{d}z\,\frac{\partial^2 u}{\partial t^2}, \tag{47}$$

where $A := A(z) = \pi B_x(z)B_y(z)$ is the cross-sectional area of the circular or elliptical cross-section and $\sigma := \sigma(z,t)$ is the stress. Here we neglect the second order terms of $\mathrm{d}z$ resulting from the multiplication of differentials. Therefore

$$\frac{1}{A(z)}\frac{\partial}{\partial z}(\sigma(z)A(z)) = \rho\omega^2 u(z),$$

after removing the time dependence. Now by applying Hooke's law, $\sigma(z) = E\partial u(z)/\partial z$ we get

$$\frac{1}{A(z)}\frac{\partial}{\partial z}\left(A(z)\frac{\partial u(z)}{\partial z}\right) = \frac{\rho}{E}\omega^2 u(z), \tag{48}$$

which is the final form of the approximative equation. Setting cross-sectional area $A(z)$ to constant it cancels out and we are again left with an ordinary wave equation. This time the solutions have a form

$$u(z) = \exp\left(\pm i\sqrt{\frac{\rho}{E}}\omega\, z\right). \tag{49}$$

We will later notice that equation (48) approximates the elastic motion of almost cylindrical fiber in $z$-direction with a positively good precision. Together with torsional 1D equation they give almost non-existent error between 1D and 3D models for low frequency waves.

## 4.4 Comparison of frequency spectra produced with 1D and 3D models

Maybe the easiest way to examine the differences of previously introduced models is to compare the frequency spectra of some typical deformation. We intend to use here a cylindrical axially symmetric deformation similar to one in Figure 13. Defining boundary curve for geometry is given in formula (35), with parameters $l = 300nm$, $D = 20nm$ and $\alpha = 0.251$. One dimensional equations should work equally well for all materials so we therefore continue to use material constants for silicon. The 3D spectrum is calculated and the eigenmodes identified by the algorithm explained in Chapter 3. Finally 1D spectrum for each type of vibration is calculated with the formulae presented in this chapter. Flexural, torsional and longitudinal frequency spectra are then plotted separately for examination.

First remark is that with such a strong perturbation parameter we intend to test the limits of approximation: with $\alpha$ large we go far from the definition of *almost* cylindrical fiber and with $l$ not very large compared to average diameter of the fiber we relax to focus only on *thin* fibers. Although we are interested here only on low frequency waves and the first spectral gap we plot the higher frequencies in order to see the increasing error between 1D and 3D models.

Like before, let us start with flexural modes. In Figure 24 there are the first four eigenmodes from 1D flexural model plotted with green dash-dotted line together with first eight eigenmodes from 3D model that passed the flexural test.

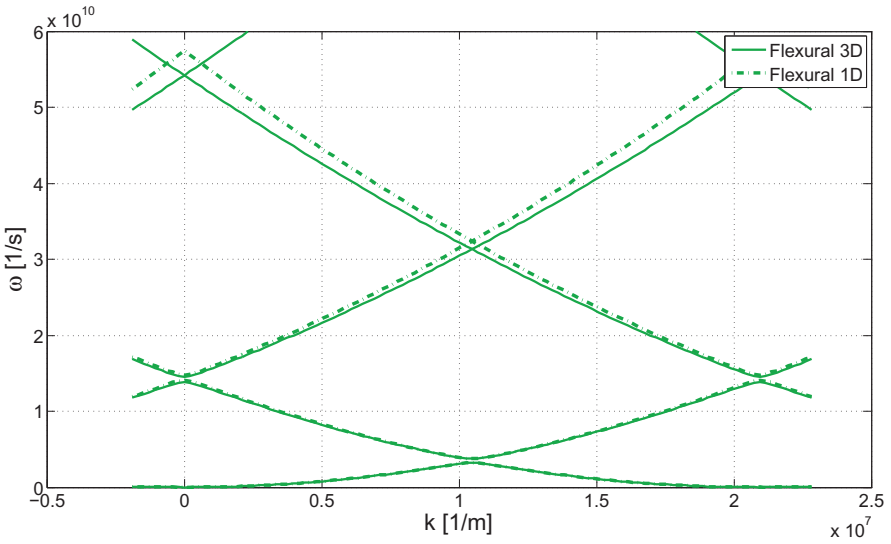


FIGURE 24 Frequency spectra of flexural waves obtained from 1D and 3D models of strongly perturbed periodical domain. Material constants are for silicon (Si). Parameters for geometry are $l = 300nm$, $D = 20nm$ with harmonic perturbation of strength $\alpha = 0.251$. In addition to reasonably good approximation with 1D, we can notice two small spectral gaps for flexural waves.

Recall that 3D eigenmodes are two-fold degenerated so there is only four solid lines visible. We can immediately see remarkable increase in error between 1D and 3D models as $\omega$ increases, but in the neighborhood of the first spectral gap, at $\omega \approx 0.4 \cdot 10^{10}\, 1/s$, the error is almost vanishing. This is good news on behalf of approximative capabilities of 1D models. Another remark is that choosing an appropriate numerical solver is important in this case, since flexural 1D model is more complex than the one for torsional or longitudinal. As a solver we used UMFPACK which seems to give much more robust and more accurate results than SPOOLES which was used for other problems. SPOOLES gives slightly more random results than UMFPACK for eigenfrequencies for $\alpha > 0.1$, and the eigenfrequency corresponding to the first flexural mode in 1D model does not go to zero as $k \to 0$. These problems were present also in 1D flexural spectra of almost cylindrical fibers with $\alpha \approx 0$ and $l$ large. There will be more discussion about numerical implementation in Chapter 8.

For torsional and longitudinal modes 1D approximation is much more accurate. In Figure 25 we present the frequency spectra for both of these modes because of similarity of the results. Spectrum corresponding to torsional waves is plotted with red while longitudinal spectrum is blue. Dash-dotted curves rep-

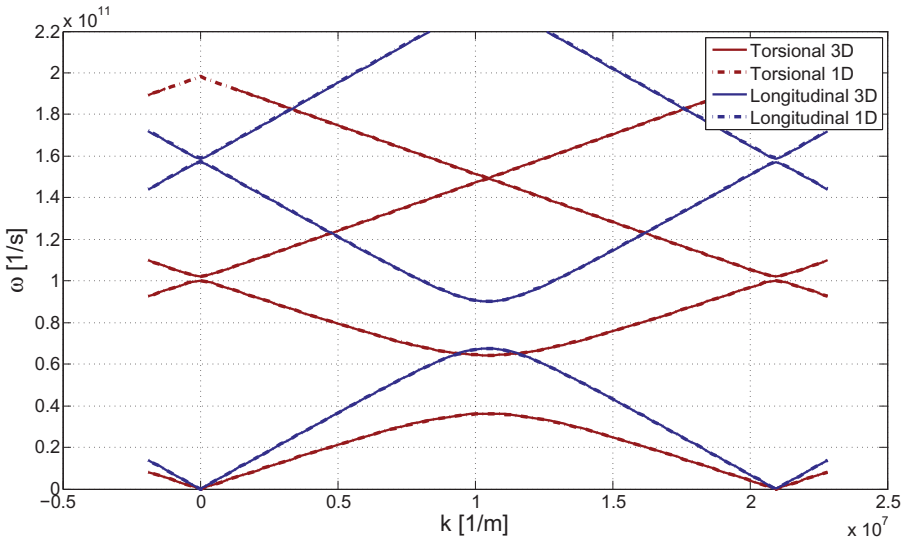


FIGURE 25 Frequency spectra of torsional and longitudinal waves obtained from 1D and 3D models of strongly perturbed periodical domain. Material constants are for silicon (Si). Parameters for harmonically perturbed geometry are $l = 300nm$, $D = 20nm$ and $\alpha = 0.251$. 1D and 3D spectra of these waves clearly coincide on this frequency range. In addition, there are wide spectral gaps for both waves.

resent the 1D spectra as solid lines represent 3D spectrum. Approximation for torsional modes is so good that it is impossible to distinguish 3D and 1D curves from each other in this resolution. This result is in line with theory: 1D approximation of the first torsional mode should coincide with results from exact elasticity theory. [18] For longitudinal modes the approximation is as well significantly good although for higher frequencies 1D and 3D are starting to separate from each other. We can make a remark from Figure 25 that the mode recognition has failed for highest torsional 3D spectral branch near $k \approx 0$ as only 1D curve is visible there. This suggests to adjust the constants in the recognition algorithm.

It can be also observed that perturbation of strength $\alpha = 0.251$ on the boundary generates a large spectral gap for both types of modes. Gaps do not coincide but as it was seen in Chapter 3 for small $\alpha$ they share about the same width. It is our interest to study how the formation of gaps responds to change of parameter $\alpha$ and length $l$ of the periodicity cell. We will examine this incident next.

## 4.5 Spectral gaps in 1D and 3D models

When considering the low temperature thermal conductance of infinite or finite perturbed fibers, it is reasonable to study the properties of spectral gaps as well. We already know that periodical perturbation on the boundary of a fiber creates spectral gaps in frequency spectrum of infinite fiber. Phonons with frequencies in this gap cannot propagate in the fiber. With a good reason we can expect that even when the periodical perturbation is finite, phonons with corresponding frequencies notice a potential barrier because of the perturbation. In the next chapter we will examine how this potential barrier arises for finite fibers when the number of periods is increased. We will also utilize the knowledge gathered here in designing a thermo-resistant fiber in Chapter 7.

Let us now compare numerically the spectral gap widths and locations calculated from 1D and 3D models. This analysis serves as a justification to use 1D models as an approximation for low energy acoustic phonons. We first calculate the widths of first spectral gaps from 1D and 3D model as a function of perturbation parameter $\alpha$ and present them in separate figures for each mode in order to compare the differences. Moreover, the location of the first spectral gap, i.e. the average of the first two eigenvalues will be plotted from 1D and 3D models. It is clear how the average and difference of eigenfrequencies is calculated in 1D case. However, when parameter $\alpha$ changes, the order of 3D eigenmodes at $k = \pi/l$ can change. Therefore in 3D case the algorithm for identifying eigenmodes is run on every step so that eigenfrequencies corresponding to correct phonon types are considered. Comparing 1D and 3D models while changing $\alpha$ becomes especially handy if one wants to find in some sense optimal strength of perturbation while keeping the approximative error limited.

In Figures 26, 27 and 28 we present widths and locations of flexural, torsional and longitudinal spectral gaps of similar periodical fiber than earlier in this chapter. The length of periodicity cell is kept constant while $\alpha$ sweeps over range $[0, 0.5]$ over prescribed steps. Nanometer length scale is used: lenght of the periodicity cell is on purpose taken $l = 10nm$ and $D = 2nm$ so that length:diameter ratio is small. This can be assumed to reveal error more easily than with longer domains. Like before the dash-dotted curves show the results from 1D models as where solid lines refer to 3D models. Color choices of the curves have a following rule: lighter color represents the location of spectral gap on frequency axis and dark colors represent the gap width as a function of parameter $\alpha$.

Let us first analyze the general behavior of these curves. Looking from the pictures the spectral gap width $\Delta\omega = \Delta\omega(\alpha)$ is increasing function for all of these modes and $\Delta\omega(\alpha) \to 0$ as $\alpha \to 0$. However, the flexural wave gap width does not increase as quickly as it does for torsional of longitudinal modes with axisymmetrical harmonic perturbation. For flexural modes both quantities, gap width and location, seem to form strictly concave curves, but for torsional and longitudinal modes the same curves are strictly convex. In fact, for torsional and longitudinal modes spectral gap location seems to be almost independent of $\alpha$.

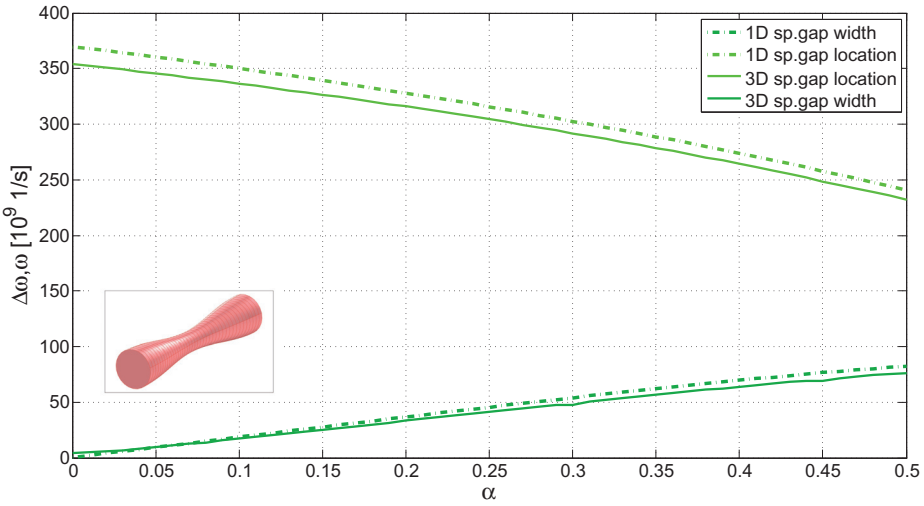


FIGURE 26 Width and location of first flexural spectral gap calculated from 1D and 3D models of periodical domain as a function of perturbation parameter $\alpha$. Inset picture shows the form of 3D periodicity cell for $l = 10nm$, $D = 2nm$ and $\alpha = 0.5$. We can remark the small systematic difference in gap location from 1D and 3D models. Gap width increases slowly as $\alpha \to 0.5$.

This phenomenom can be explained with constant phase velocity of torsional and longitudinal modes. Changing the average diameter of the fiber does not affect speed of these modes. There is also an interesting difference between characteristics of mode types: in order to lower flexural gaps one must increase $\alpha$ thus lowering the weight and width of the fiber, but this doesn't lower the location of gaps for torsional or longitudinal modes which in fact slightly increase. Changing $l$, the length of the cell, is expected to take greater effect on longitudinal and torsional gap locations. We remark that if the parameter $\alpha$ controls the perturbation in such a way that the mass of periodicity cell is constant, then also the flexural spectral gap location becomes independent of $\alpha$. We will take a quick look into wavelengths and velocities of these modes in Chapter 7.

In addition, the figures reveal that the only significant error between models seems to be the one for flexural spectral gap location in 1D approximation. Although this was expected to happen considering the analysis of frequency spectra in earlier sections, it was not clear how this error would spread over wider range of parameter $\alpha$. It seems to have characteristics of systematic error because the error is almost independent of $\alpha$. This kind of inaccuracy could be easily corrected by subtracting the difference from 1D spectrum or by scaling the spectrum by some exponent $\beta$ if agreement on wider range of $\omega$ is desired. Also applying a more advanced 1D model such as Timoshenko beam theory should give more

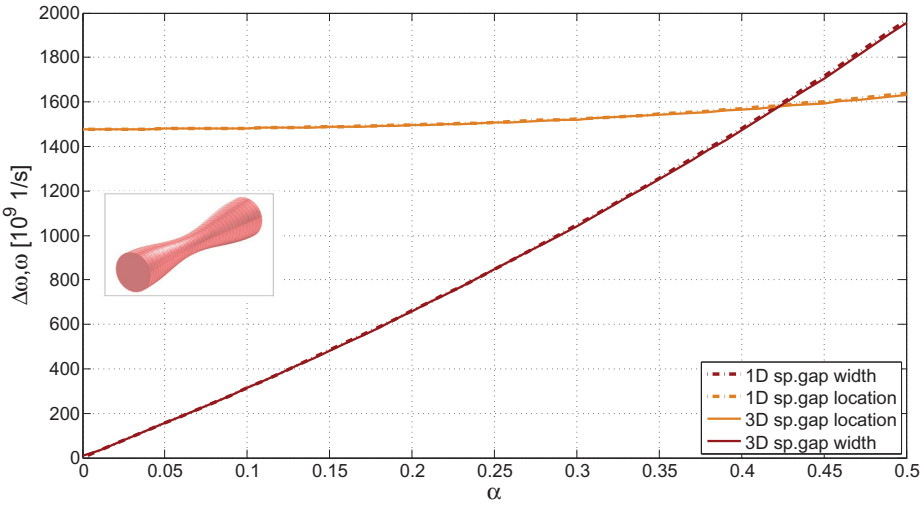


FIGURE 27 Width and location of first torsional spectral gap calculated from 1D and 3D models of periodical harmonic domain as a function of perturbation parameter $\alpha$. Inset picture shows the form of 3D periodicity cell for $l = 10nm$, $D = 2nm$, $\alpha = 0.5$. We see that gap width increases sharply as the perturbation parameter $\alpha$ increases.

accurate results, as suggested by [18]. Final remark is that for width and location of torsional and longitudinal spectral gap there is a slight error increasing polynomially as a function of $\alpha$.

In Figure 29 there are plots of spectral gap locations of all the three modes as a function of $l$, the length of periodicity cell. The length $l$ changes from $8nm$ to $60nm$ for 3D model and up to $100nm$ for 1D models. The choice of horizontal axis limits corresponds to diameter:length ratios 1:4 to 1:50. At the lower end of the range of period $l$ the perturbation for infinite fiber is changing rapidly compared to cell dimensions into $x$- and $y$-direction, while on the other end change is slow. This means that with $l/D$ small we test the reliability of 1D approximation, because the cell is not "thin". First impression is that the curves show inverse proportionality between $l$ and $\omega$. All the modes seem to obey this behavior and there is no such characteristic difference between flexural and the two other modes like there was in a case of variable strength of perturbation. Also the error between 1D and 3D gap locations is clearly insignificant for high $l/D$. Only a small difference between 1D and 3D flexural mode approximation can be observed for small $l/D$.

In Figure 30 we show the first spectral gap widths or flexural, torsional and longitudinal modes. The length of period $l$ again changes from $8nm$ to $60nm$ for 3D model and $8nm$ to $100nm$ for 1D models. Relation between length of period

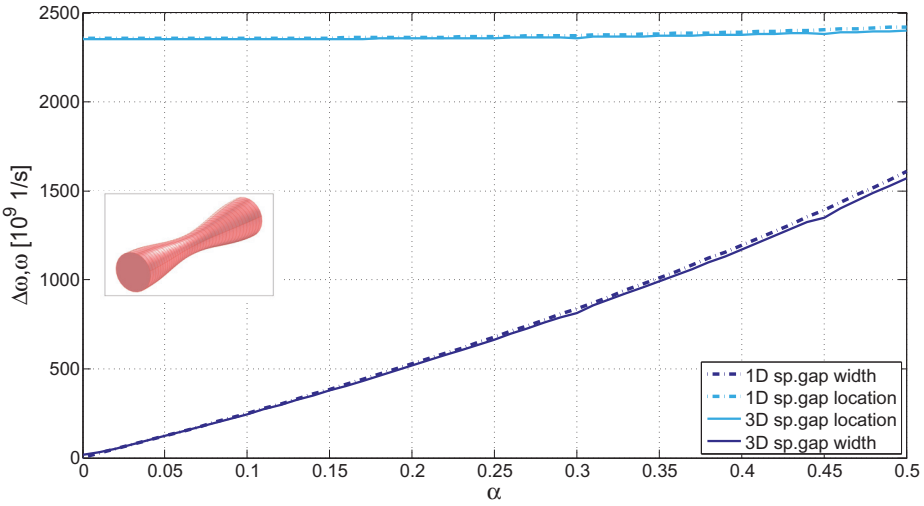


FIGURE 28 Width and location of first longitudinal spectral gap calculated from 1D and 3D models of periodical harmonic domain as a function of perturbation parameter $\alpha$. Inset picture shows the form of 3D periodicity cell for $l = 10nm$, $D = 2nm$, $\alpha = 0.5$. We can notice a slightly increasing error in gap width and location as $\alpha \to 0.5$. Harmonic perturbation seems to induce a comparably wide spectral gap for longitudinal waves.

$l$ and gap widths seems to be $\Delta\omega \sim 1/l$. We can also see that error between 1D and 3D comes slightly visible at $l/D < 5$ in this resolution.

We may end this section by concluding that 1D models are clearly suitable for approximating the characteristics of first spectral gaps for 3D flexural, torsional and longitudinal modes in periodically perturbed cylindrical fibers. They are faster to solve and while there is no need for eigenmode identification, there is no possibility for the identifying algorithm to fail.

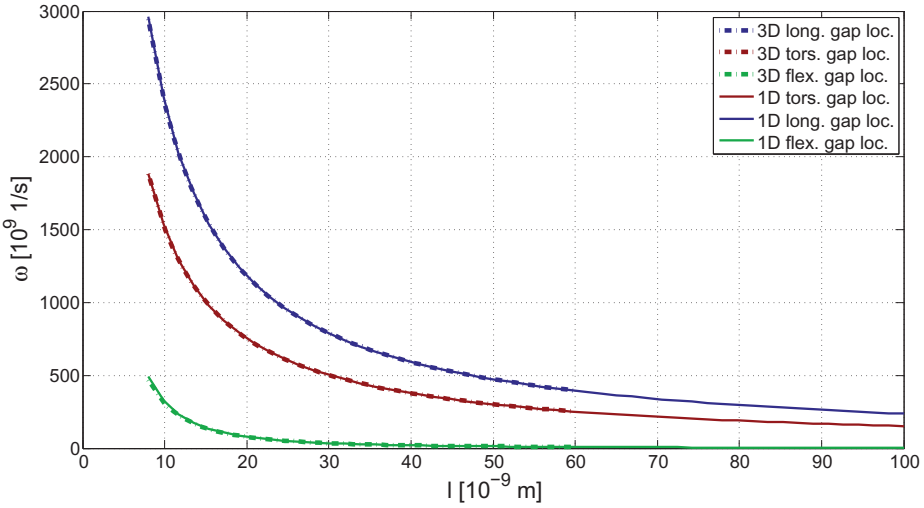


FIGURE 29 Locations of the first flexural, torsional and longitudinal spectral gaps for harmonically perturbed silicon (Si) fiber calculated from 1D and 3D models as a function of length $l$ of the periodicity cell. Gap locations $\omega$ from 3D and 1D model are calculated for $l = 8 - 60nm$ and $l = 8 - 100nm$, respectively. Diameter is $D = 2nm$ and perturbation strength $\alpha = 0.251$ is kept constant. We can perceive a good correspondence between 1D and 3D models when $l$ increases.

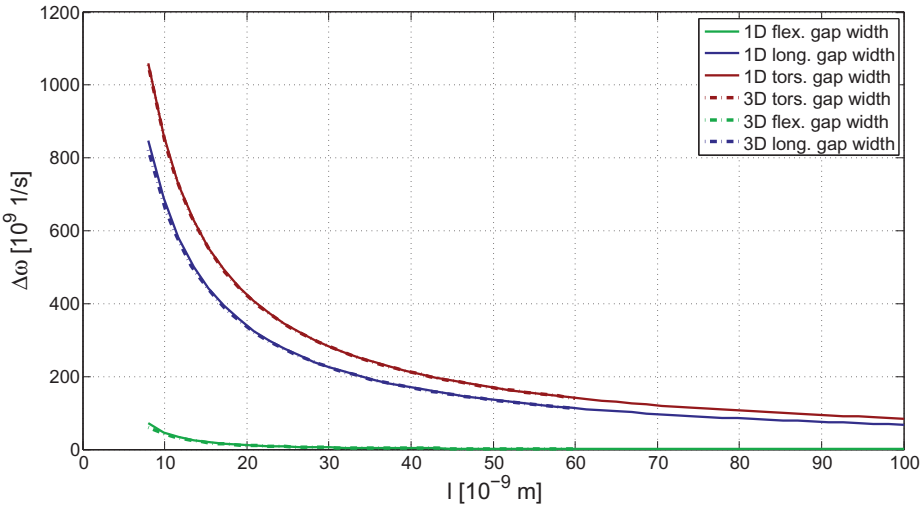


FIGURE 30 Spectral gap widths of the first flexural, torsional and longitudinal modes for harmonically perturbed silicon (Si) fiber calculated from 1D and 3D models as a function of length $l$ of the periodicity cell. Gap widths $\Delta\omega$ from 3D and 1D model are calculated for $l = 8 - 60nm$ and $l = 8 - 100nm$, respectively. Diameter is again set to $D = 2nm$ and perturbation strength is a constant $\alpha = 0.251$.

# 5 TRANSMISSION COEFFICIENTS

In the previous chapters we have studied infinitely long periodically perturbed almost cylindrical fibers. We calculated frequency spectrum for 1D and 3D models and made conclusions about how the lowest energy waves would be disturbed by boundary deformation. We now change the perspective to finite fibers with finite perturbation and explain how to analyze the wave propagation in them. There are some reasons that motivate us to examine thermal conductance of finite fibers: In practical applications nanostructures are finite and usually there is an interest to keep length:diameter ratios in control. Considering for example a 2D grid of bolometers with thermally insulating legs, the density of censors in the grid is inversely proportional to length of legs squared. In such a case, infinite models do not always give an adequate picture of the thermal properties of the system. Moreover, long periodical fibers containing thousands of periods can sometimes be replaced with shorter fiber designs consisting only 10-100 periods of perturbation of variable period length. This construction can reflect phonon waves more effectively than strictly periodic one. A simple example of this type of a fiber was shown in Figure 2.

Methods of analysis used in previous chapters must be changed slightly in order to study finite fibers. This is because we cannot calculate a similar frequency spectrum for fibers containing only a finite deformation. However, there is another way to study wave propagation: a transmission coefficient curve, which is a probability $p_j(\omega)$ for a phonon $j$ of some frequency $\omega$ to be transmitted over the perturbed part $G(R)$ of the fiber. The probability can be calculated from so called scattering amplitudes $s_{jp}$ which are complex numbers describing the elastic wave amplitude and phase before and after the perturbation. The main difficulty is how to find the numbers $s_{jp}$ from 1D or 3D models.

This problem is attacked by using a method [13] to calculate a scattering matrix for the problem and use it to find transmission probabilities. Scattering matrix is a $2M$-dimensional square matrix and its elements are defined as complex amplitudes for different scattered waves. In the next sections we describe this matrix and its use in calculation for transmission coefficients. Moreover, there is a direct way to solve the probabilities by evaluating the solutions of 1D and 3D

problems at the circular ends of the domain. We will first take a look into that and compare the transmission coefficients of 1D and 3D longitudinal waves. It is then proposed that if the 1D approximation works for longitudinal waves it works also for flexural and torsional waves. One dimensional transmission coefficients are also calculated from scattering matrix so that the methods can prove each other to give correct numerical values. The formulation is done following [27] where scattering matrix was calculated for 1D and 2D domains.

## 5.1 Scattering of elastic waves in perturbed 3D fiber

As a mathematical model for the 3D nanofiber $G$ we use an infinite cylindrical domain lying on $z$-axis in $\mathbb{R}^3$. The shape of the cylinder is perturbed slightly near origin so that the perturbation serves as a potential barrier for elastic waves coming from plus or minus infinity along the fiber. When moving farther away from origin we can think the perturbation as a target, a scatterer, which is bombarded by elastic waves whose scattering amplitudes are then measured far away from origin. Let $G$ be a smooth and simply connected domain such that

$$G = \{\, (x,y,z) \,:\, |z| > R,\, |x|^2 + |y|^2 \leq 1 \,\} \cup G(R) \tag{50}$$

where $G(R)$ is a compact simply connected set acting as a perturbed part of the cylinder. By assuming simply connectedness for $G(R)$ we demand there are no holes in the fiber. Let $S > R$ and

$$G(S) = G \cap \{\, (x,y,z) \,:\, |z| \leq S \,\} \tag{51}$$

so that $G(R) \subset G(S)$. Domain $G(S)$ is called a truncated domain, which consists of the perturbed part $G(R)$ and two straight cylinders of length $S - R$ attached to the circular ends of $G(R)$. An illustration of the model is shown in Figure 2 in Chapter 1. Admissible elastic displacement modes in 3D model are the bounded continuous spectrum eigensolutions (see Chapter 1) of Lamé-operator (18) in this domain.

Given a quick thought about the model it seems intuitive that far away from the scatterer there should be only normal phonon modes present. That is because the domain looks locally a straight cylinder and in a cylinder the lowest energy elastic waves are normal phonon modes as was explained in Chapter 2. This heuristic also leads to a general philosophy of elastic scattering theory: to be able to solve the normal phonon modes at given frequency and to express the complete solution as a sum of them. On the other hand, near the deformed part of the fiber there can exist some smooth part of the solution which may be impossible to express as a sum of normal phonon modes. Therefore we only use asymptotic symbol $\mathcal{O}(\exp(-\gamma|z|))$ to keep inside everything else than normal phonon modes. For mathematical formulation of the space of admissible phonon waves see e.g. [27]. To summarize we are looking for phonon displacement fields $Y_j$

such that

$$Y_j(x,y,z) = w_j^+(x,y,z) + \sum_{p=1}^{N} s_{jp} w_p^-(x,y,z) + \mathcal{O}(e^{-\gamma|z|}), \tag{52}$$

where we have one incoming phonon $w_j^+$ and $N$ different outgoing phonons $w_j^-$ forming a linear combination with complex scattering amplitudes $s_{jp}$. The sum of outgoing waves can be thought as a scattering pattern. How large $N$ is depends on the frequency $\omega$ of the waves. In the lowest energy interval $\omega \in [0, \omega_1[$ below the so-called first threshold $\omega_1$, $N = 8$. As we have seen from the figures in previous chapters showing 3D spectra of straigth cylinders and various perturbed domains, there exist only four different eigenmodes in this energy region. Because these modes can propagate either plus or minus infinity their number is multiplied by two. Also at the higher energy levels number $N$ is always even, because of existence of right and leftward propagating waves. Moreover, we recall that normal phonon modes $U_j(x,y,z)$ in infinite unperturbed cylinders were calculated analytically in Chapter 2. We can use them as incoming and outgoing waves in the previous formula after defining

$$w_j^{\pm}(x,y,z) = \begin{cases} \eta_R(z) U_j(x,y,z), & U_j \text{ coming from / going to } \infty, \\ \eta_R(-z) U_j(x,y,z), & U_j \text{ coming from / going to } -\infty. \end{cases} \tag{53}$$

A smooth cut-off function $\eta_R$ was defined by

$$\eta_R(z) = \begin{cases} 1, & z \geq R+1, \\ e^{1-1/(1-|z-R-1|^2)}, & R < z < R+1 \\ 0, & z \leq R. \end{cases}$$

Finally, we can assume that the modes $w_j^{\pm}$ are organized so that for $j = 1, \ldots, 4$ waves $w_j^-$ are going to $-\infty$ and for $j = 5, \ldots, 8$ waves $w_j^-$ go to $\infty$. Also the waves $w_j^+$ for $j = 1, \ldots, 4$ are incoming from $-\infty$ and waves $w_j^+$ for $j = 5, \ldots, 8$ are incoming from $\infty$. Numbers $1, \ldots, 4$ therefore refer to waves acting on the left and numbers $5, \ldots, 8$ on the right.

Recall that we assumed simply connectedness of the domain, so there are no holes inside the fiber. Also, because other scattering processes arising from e.g. high temperature (phonon-phonon scattering), defects or impurities of crystal are assumed to be negligible. Therefore only the perturbation of the boundary in our model is affecting the amplitudes $s_{jp}$. However, we can conjecture that given a complex enough boundary geometry, any scattering pattern can be obtained from outgoing waves $w_p^-$, provided that the energy of the incoming wave $w_j^+$ is preserved. In other words $\sum_p |s_{jp}|^2 = 1$ for all $j$.

To proceed with discussion, we have to expect that given a suitably smooth and symmetric perturbation there should not be much transformation between different phonon types: again, flexural should stay mainly flexural, torsional should stay mainly torsional and longitudinal should stay mainly longitudinal.

We remark that such an assumption must be made cautiously, because for example bulk phonons are known to couple in free boundary scattering. Assuming this allows us to use the previously introduced 1D models in approximation, because they only simulate one type of displacement at a time. How well they approximate, can be decided *a posterior* by comparing the 1D transmission coefficients to ones obtained from 3D model. If there is not much difference then 1D modelling proves itself useful. To compare the differences, we will first introduce a simple method to calculate transmission coefficients for 3D longitudinal waves.

## 5.2 Boundary amplitude method for longitudinal 3D waves

We take into account the assumption that in a domain with enough symmetry basic elastic modes should remain the same after scattering and start to look for 3D solutions of the form

$$\vec{u}(x,y,z) = w_1^+(x,y,z) + s_1 w_1^-(x,y,z) + s_2 w_2^-(x,y,z) + \mathcal{O}(e^{-\gamma|z|}), \qquad (54)$$

where the incoming wave $w_1^+(x,y,z) = \eta_R(-z)(0,0,\exp(i\sqrt{\rho/E}\omega z))$ is mainly of longitudinal type. In theory this wave $w_1^+$ contains harmonics of real longitudinal wave and possibly other types of waves, but because the wavelength of those waves is much lower they can be assumed to pass the perturbation without scattering. Wave $w_1^+$ is used here for simplicity of calculations in order to avoid Bessel functions arising in analytic solutions in Chapter 2. There are also two outgoing waves $w_1^-(x,y,z) = \eta_R(-z)(u_1^-, v_1^-, (\exp(-i\sqrt{\rho/E}\omega z))$ and $w_2^-(x,y,z) = \eta_R(z)(u_2^-, v_2^-, \exp(i\sqrt{\rho/E}\omega z))$ having the same form than the incoming one. There might be some displacement involved in $x$-$y$-direction in the solution, but it is assumed that $u_1^-$,$u_2^-$,$v_1^-$ and $v_2^-$ are small. Constants $\rho$ and $E$ again describe density and Young modulus and they depend on the material at hand.

Problem to be solved is Lamé's equation (18) $\mathcal{L}\vec{u} = 0$ on the truncated domain $G(S)$ with free boundary condition $\nu \cdot \sigma(\vec{u}) = 0$ on $\partial G(S) \backslash I(S)$, where $I(S) = \{\, (x,y,z) \in G \,:\, |z| = S \,\}$ is the set of circular boundaries of truncated domain. Boundary conditions at $I(S)$ must be set differently in order to obtain a solution of the form (54). In COMSOL, strong boundary conditions must be given in terms of so called Robin boundary condition which is a sum of Dirichlet and Neumann conditions. It is sometimes used e.g. in electromagnetics as an impedance boundary condition. We use it here to obtain continuity for displacement and stress fields at the circular boundaries. Neumann condition can be given as a vector differential operator so that each component of the solution can be differentiated separately. Let us first assume

$$\vec{u}(x,y,z) = (0,0,\exp(i\zeta z)) + s_1(u_1^-, v_1^-, \exp(-i\zeta z)),$$

for all $(x,y,z) \in I(S)$, $z = -S$. Because $s_1$ and $s_2$ are unknown, we set the boundary conditions accordingly to get rid of them in the equations. Taking a $z$-

directional derivative $D_z = (0, 0, \partial_z)$ only from $z$-displacement component from the solution gives

$$-D_z \cdot \vec{u}(x, y, z) = -i\zeta \exp(i\zeta z) + s_1 i\zeta \exp(-i\zeta z). \tag{55}$$

We end up to an equation in Robin form

$$-D_z \cdot \vec{u}(x, y, z) + (0, 0, -i\zeta) \cdot \vec{u}(x, y, z) = -2i\zeta \exp(i\zeta z) \tag{56}$$

by adding the term $(0, 0, -i\zeta) \cdot \vec{u}(x, y, z)$. Equation (56) will be used as boundary condition at $(x, y, z) \in I(S)$, $z = -S$, for incoming waves from $-\infty$. At the right boundary $(x, y, z) \in I(S)$, $z = S$, there can coexist in the solution another incoming wave from $+\infty$ which must be forced to zero by setting:

$$D_z \cdot \vec{u}(x, y, z) - (0, 0, i\zeta) \cdot \vec{u}(x, y, z) = 0, \quad (x, y, z) \in I(S),\ z = S. \tag{57}$$

By taking equation (57) as the right boundary condition, it implies that if the solution is of the form $\vec{u}(x, y, z) = (u_2^-, v_2^-, s_2 \exp(i\zeta z) + A \exp(-i\zeta z))$ at $z = S$, then

$$D_z \cdot \vec{u}(x, y, z) = s_2 i\zeta \exp(i\zeta z) - Ai\zeta \exp(-i\zeta z).$$

Now by adding the term $(0, 0, -i\zeta) \cdot \vec{u}(x, y, z)$ we have

$$D_z \cdot \vec{u}(x, y, z) + (0, 0, -i\zeta) \cdot \vec{u}(x, y, z) = -2Ai\zeta \exp(-i\zeta z),$$

which satiesfies the boundary condition (57) only if $A = 0$. The solution at $z = S$ must be therefore $\vec{u}(x, y, z) = (u_2^-, v_2^-, s_2 \exp(i\zeta z))$, which was indeed aimed at.

Let us examine the solutions of the problem with an example: Let $S = 132nm$, and let the boundary curve of the perturbed part of fiber consist two periods of cos-curve with wavelength $60nm$. Length of the perturbed part is therefore equal to $120nm$ and it is less than half of the full length of domain. Boundary curve $B_x(z) = B_y(z)$ is shown in Figure 31 by green. The problem is to find longitudinal 3D displacement field with equation $\mathcal{L}\vec{u} = 0$ with free boundary condition together with previously introduced additional boundary conditions. Frequency $\omega = 392 \cdot 10^9\, 1/s$ is on purpose taken approximately in the middle of the first longitudinal spectral gap of infinite periodical fiber with similar perturbation.

In Figure 31 there is shown the solution to the problem in the inset picture at lower left corner. In the main graph the displacement is evaluated along $z$-axis and drawn as a function of $z$ with blue. The solution seems to behave intuitively, so that far from the perturbation it is close to a superposition of harmonic waves and transformation between waves occurs on the perturbed part of domain. We see that when the amplitude is changing the phase also changes. It can be seen by comparing the blue curves to red curve, which is the shape of the incoming wave extended to the right side of perturbation.

Complex valued amplitudes $A_{\text{left}}$ and $A_{\text{right}}$ of the solution field at the boundary are drawn in the figure on the left and right end, but they can also be calcu-

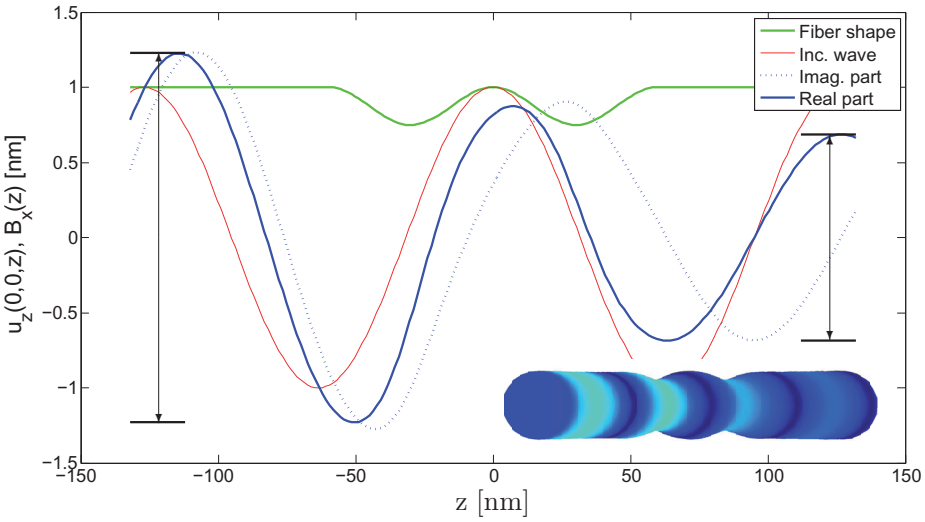


FIGURE 31 $z$-displacement of "almost" longitudinal 3D wave along $z$-axis of 3D cylindrical fiber with two periods of harmonical perturbation. Radial displacement of incoming wave is assumed to be zero. Solid (dotted) blue line is the real (imaginary) part of scattered displacement field in $z$-direction. Red curve is the incoming wave shape in $z$-direction. Green curve shows the silhouette of the fiber. Real and complex field amplitudes $u_z(0,0,z)$ at boundaries $z = \pm S$, which are solved by fitting sin-curves in the solution, are marked with black. Inset picture shows the true 3D displacement field of the solution.

lated easily from the solution by fitting sin-curves on it. We obtain

$$\begin{aligned} A_{\text{left}} =& \frac{\sqrt{\zeta^2(\operatorname{Re} u_z(-S))^2 + (\operatorname{Re}\partial_z u_z(-S))^2}}{\zeta} + \\ &+ i\frac{\sqrt{\zeta^2(\operatorname{Im} u_z(-S))^2 + (\operatorname{Im}\partial_z u_z(-S))^2}}{\zeta}, \\ A_{\text{right}} =& \frac{\sqrt{\zeta^2(\operatorname{Re} u_z(S))^2 + (\operatorname{Re}\partial_z u_z(S))^2}}{\zeta} + i\frac{\sqrt{\zeta^2(\operatorname{Im} u_z(S))^2 + (\operatorname{Im}\partial_z u_z(S))^2}}{\zeta}, \end{aligned} \tag{58}$$

which are derived from the equations such as

$$\begin{aligned} \operatorname{Re} u_z(-S) &= \operatorname{Re} A_{\text{left}} \sin(\zeta(-S) + \phi) \\ \operatorname{Re}\partial_z u_z(-S) &= \operatorname{Re} A_{\text{left}}\, \zeta \cos(\zeta(-S) + \phi). \end{aligned}$$

Boundary amplitudes can be used to solve transmission and reflection coef-

ficients, i.e. normalized scattering amplitudes $|s_1|^2$ and $|s_2|^2$ with

$$\begin{aligned} p_{\text{trans}} &= |s_2|^2 = \frac{1}{2}|A_{\text{right}}|^2, \\ p_{\text{ref}} &= |s_1|^2 = \frac{1}{2}|A_{\text{left}}|^2 - 1. \end{aligned} \tag{59}$$

We will show how the transmission probability formula is obtained. To relate amplitudes $A_{\text{left}}$ and $A_{\text{right}}$ to the probabilities we need only the absolute values of the boundary amplitudes

$$\begin{aligned} |A_{\text{left}}|^2 &= \frac{\zeta^2|u_z(-S)|^2 + |\partial_z u_z(-S)|^2}{\zeta^2} \\ |A_{\text{right}}|^2 &= \frac{\zeta^2|u_z(S)|^2 + |\partial_z u_z(S)|^2}{\zeta^2}. \end{aligned}$$

Assume first $u_z(S) = s_2 \exp(-i\zeta S)$. Then $\partial_z u_z(S) = -i\zeta s_2 \exp(-i\zeta S)$. By taking absolute value of these complex numbers we get $|u_z(S)|^2 = |s_2|^2$ and $|\partial_z u_z(S)|^2 = \zeta^2|s_2|^2$. By multiplying the former with $\zeta^2$ and adding them we get

$$2\zeta^2|s_2|^2 = \zeta^2|u_z(S)|^2 + |\partial_z u_z(S)|^2,$$

from where the formula for $p_{\text{trans}}$ follows. Transmission probability of the lowest energy phonons will later be plotted as a function of frequency $\omega$ and compared to similar curves obtained with scattering matrix method. The boundary amplitude method will be abbreviated with BAM in future.

## 5.3 Boundary amplitude method for 1D waves

When looking more closely on BAM for 3D modes we can see that it only observes $z$-directional motion on $z$-axis and the transmission coefficients are calculated with only that information. It therefore suggests that the same method could be used with 1D models. This will be later shown to be true by comparison, when transmission coefficients calculated from scattering matrix are available.

Let us assume that a problem to be solved on domain $[-S, S]$ can be any of the 1D models (41), (45) or (48). The wavenumber $\zeta$ in the solution form comes from corresponding 1D model. Boundary conditions at $z = \pm S$ must be set similarly to 3D case in order to obtain unique solution of the form

$$u(z) = w_1^+(z) + s_1 w_1^-(z) + s_2 w_2^-(z) + \mathcal{O}(e^{-\gamma|z|}). \tag{60}$$

We use $(-\partial_z - i\zeta)u = 2i\zeta \exp(i\zeta z)$ at $z = -S$ and $(\partial_z - i\zeta)u = 0$ at $z = S$.

Let us again examine the problem with an example: Let $S = 55nm$, and let the boundary curve of the perturbed part of fiber consist of five periods of cos-curve with wavelength $10nm$ and diameter $D = 2nm$. Boundary curve $B_x(z) = B_y(z)$ is shown in Figure 32 by green. The problem is to find torsional 1D displacement field with equation (45) with previously introduced boundary conditions.

Frequency of the wave $\omega = 1900 \cdot 10^9\, 1/s$ is on purpose set to be near the upper edge of first torsional spectral gap of infinite periodical fiber with similar perturbation. This can be checked from Figures 29 and 30. The $\theta$-displacement field

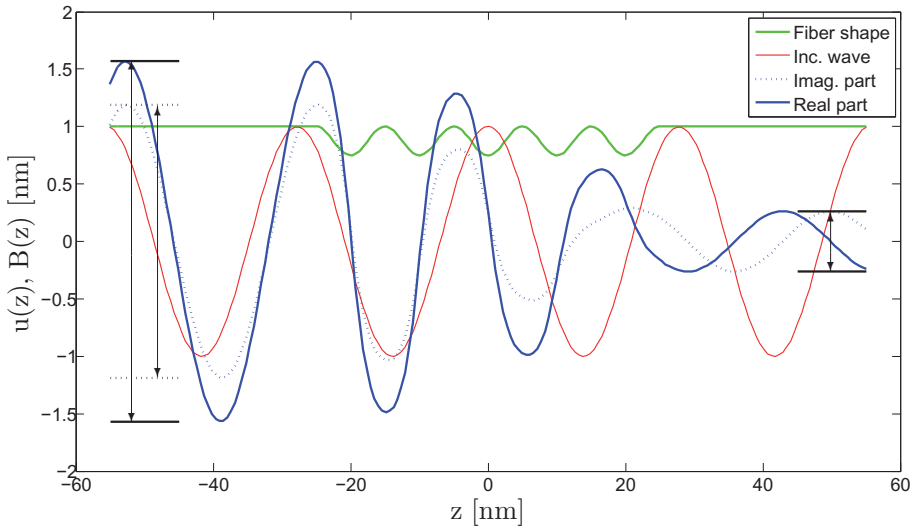


FIGURE 32 Scattering of 1D torsional left-incoming wave from finite periodical perturbation. Boundary shape of 1D fiber is printed in green. Solid (dotted) blue line is the real (imaginary) part of scattered displacement field in $\theta$-direction in cylindrical coordinate system, respectively. Red curve is the incoming wave shape, which is plotted also to left side of the perturbation for comparing the phase shift of field after scattering. Field amplitudes at boundaries, which are solved by fitting sin-curves in the solution, are marked with black.

$u$ is plotted in Figure 32 with other curves that provide the phase information of incoming and scattered waves. The solution seems to behave in a same way comparing to longitudinal 3D solution in previous section. Amplitudes of the solution at boundary are again calculated by fitting sin-curves on the solution.

We may generalize that the boundary amplitude method works for all of the 1D models in question and clearly, differences in boundary amplitudes are related to frequencies near the spectral gaps. We can predict that BAM should give a good correspondence with scattering matrix method which will be introduced later in this chapter.

## 5.4 Comparison of transmission coefficients of longitudinal 1D and 3D waves

We will now compare the transmission coefficient curves obtained with BAM from 1D and 3D models of longitudinal waves. The domain used in simulation cannot be too long because the size of 3D mesh increases rapidly. Therefore we only use perturbations with a simple strictly periodic structure and with a small number of periods starting from two. In Figure 33 there are presented the trans-

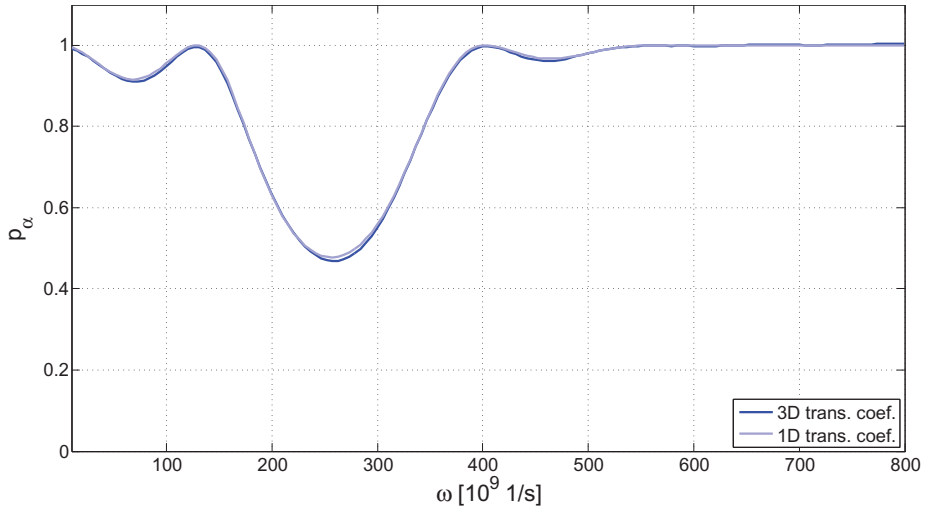


FIGURE 33 Longitudinal transmission coefficients obtained from 3D and 1D models for a fiber containing two periods of cos-type perturbation of wavelength $l = 90nm$ on the boundary. Diameter of the fiber is $D = 10nm$ and perturbation strength $\alpha = 0.251$. We can see that 1D approximation coincides with 3D reasonably well.

mission coefficients of the similar fiber that was used also in Figure 31. It consists of two periods of harmonic perturbation with wavelength $l = 90nm$, diameter $D = 10nm$, and amplitude $\alpha = 0.251$ together with straight cylinders of size $0.55 \cdot 2 \cdot l = 99nm$ attached to the ends. Transmission coefficient curve obtained from 1D model is drawn with light blue while 3D curve is drawn with dark blue. We can see from the picture that the error is almost non-existent.

In order to analyse the error we try to magnify it by introducing a longer and more complex domain with seven periods of cos-curve of wavelength $l = 45nm$. Length of the perturbed part is therefore $315nm$ and to construct the domain appropriately we add cylinders of size $157.5nm$ to both ends. Total length becomes $630nm$. In order to solve a 3D problem in such a thin and long domain we have

to scale down $z$-coordinates in 3D mesh. More discussion about the implementation is left to Chapter 8. Longitudinal transmission coefficients from 1D and 3D models are presented in Figure 34.

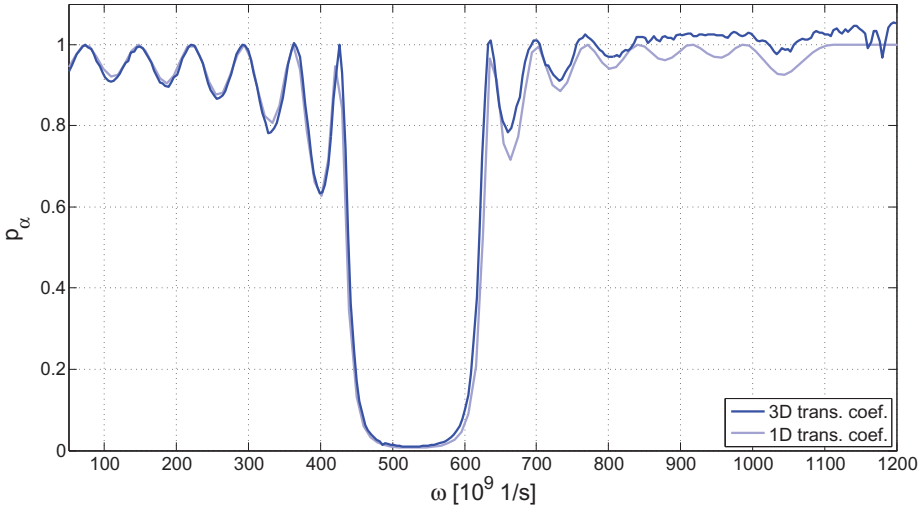


FIGURE 34 Longitudinal transmission coefficients obtained from 3D and 1D models for a fiber containing seven periods of cos-type perturbation of wavelength $l = 45nm$ on the boundary. Diameter is again $D = 10nm$ and perturbation parameter $\alpha = 0.251$. There is an increasing error as a function of $\omega$, which can be explained as numerical inaccuracy because the wavelength of incoming wave gets closer to the length of used 3D mesh element.

We immediately notice that locations of the cliffs in the curves are usually at correct place but there is an increase in error between the depths as frequency increases. This imprecision can be explained as an approximative error of 1D model, which was also detected with eigenfrequency spectra. However the main cliff, its location and depth, is approximated well by 1D model. For higher frequencies there appears some kind of fluctuation in the 3D curve which could be explained as numerical error. This is because the wavelength of higher frequency waves becomes closer and closer to the size of $z$-scaled elements in 3D mesh.

Conclusion of this section is that BAM gives a very good correspondence for transmission coefficients of 1D and 3D longitudinal modes. It therefore suggests that 1D approximation should work well also for flexural and torsional modes. In addition, because longitudinal 1D approximation coincides well with the 3D case it can be expected that fibers with symmetrical perturbation do not couple different elastic modes strongly together.

For torsional modes the error between 1D and 3D can be expected to be of same magnitude as it is for longitudinal modes, because the equation used for

torsional 1D approximation differs from longitudinal one by only its coefficient functions. However, for flexural waves the error between 1D and 3D is expected to be somewhat higher because higher error was observed also in comparison of frequency spectra. Despite the fact, we can expect that cliffs in transmission coefficient curves obtained from 1D and 3D models give well enough correspondence so that 1D model can be used in calculation of thermal conductance.

## 5.5 Scattering matrix method for 3D and 1D models

In order to verify the results obtained with BAM we take a look at a different mathematical method to calculate transmission probabilities. One method was introduced in [13] and it is related to mathematical approximation of the scattering matrix of the problem.

To start with, let us briefly concentrate on the coefficients $s_{jp}$ in the solution (52). Under the first threshold there are four elastic modes present: two flexural ($F_1$, $F_2$), one torsional ($T_1$) and one longitudinal ($L_1$). These modes can be going to either plus or minus infinity, so in the scattering matrix there are total of eight elements in each row related to scattering of one of the normal modes. Total number of rows in $\mathbf{S}$ is eight as well. To clarify the matrix a bit more we can mark each element with an arrow describing the propagation direction of the corresponding wave.

$$\mathbf{S} = \begin{pmatrix} \underline{\overrightarrow{F_1}} & \underline{\overrightarrow{F_2}} & \underline{\overrightarrow{T}} & \underline{\overrightarrow{L}} & \underline{\overleftarrow{F_1}} & \underline{\overleftarrow{F_2}} & \underline{\overleftarrow{T}} & \underline{\overleftarrow{L}} \\ \vdots & \underline{\overrightarrow{F_2}} & \vdots & \vdots & \vdots & \underline{\overleftarrow{F_2}} & \vdots & \vdots \\ \vdots & \vdots & \underline{\overrightarrow{T}} & \vdots & \vdots & \vdots & \underline{\overleftarrow{T}} & \vdots \\ \vdots & \vdots & \vdots & \underline{\overrightarrow{L}} & \vdots & \vdots & \vdots & \underline{\overleftarrow{L}} \\ \underline{\overrightarrow{F_1}} & \vdots & \vdots & \vdots & \underline{\overleftarrow{F_1}} & \vdots & \vdots & \vdots \\ \vdots & \underline{\overrightarrow{F_2}} & \vdots & \vdots & \vdots & \underline{\overleftarrow{F_2}} & \vdots & \vdots \\ \vdots & \vdots & \underline{\overrightarrow{T}} & \vdots & \vdots & \vdots & \underline{\overleftarrow{T}} & \vdots \\ \vdots & \vdots & \vdots & \underline{\overrightarrow{L}} & \vdots & \vdots & \vdots & \underline{\overleftarrow{L}} \end{pmatrix} \tag{61}$$

We also underlined those elements of scattering matrix $\mathbf{S} = (s_{jp})_{j,p=1,\ldots,8}$ that can be approximated with corresponding elements from 1D scattering matrices. It is supposed at this point that the perturbation of the domain is selected so that the other elements are close to zero. We have already seen some evidence that by designing the domain with axial symmetry there is just a negligible scattering from one type to another.

Generally, with scattering matrix one can calculate the scattering pattern of any incoming wave field. For example, if one has an incoming wave field $\vec{u} = \sum_{j=1} A_j w_j^+$ expressible as a sum of normal modes the scattered field is then $(\mathbf{S}\vec{u})_j = \sum_p A_p s_{jp} w_p^-$.

At the moment, the problem is how to calculate the coefficients $s_{jp}$. This will be done following [27] where the method was used for scattering matrices of size $2M \times 2M$. For each $j$ we will use an approximative method for evaluating the row vector $(s_{j1}, \ldots, s_{j2M})$ from the scattering matrix. We define a certain functional $J_j$ and later minimize it to give an approximative value to elements of $j$-th row vector. This functional $J_j$ simply compares the numerical solution of Lamé's equation on truncated domain to any given linear combination of normal modes. Finally in order to minimize functionals $J_j$ we turn them into a matrix equation which can be easily solved numerically.

First we write down the correct boundary value problem in truncated domain $G(S)$ where $S > R$ so that the perturbed part $G(R)$ is included in.

$$\begin{aligned} \mathcal{L}Y_j^S(x,y,z) &= 0, \quad (x,y,z) \in G(S), \\ \nu \cdot \sigma(Y_j^S)(x,y,z) &= 0, \quad (x,y,z) \in \partial G(S) \backslash I(S), \\ (\partial_\nu + i\zeta)Y_j^S &= (\partial_\nu + i\zeta)\left( w_j^+ + \sum_{p=1}^{2M} a_p w_p^- \right), \quad (x,y,z) \in I(S), \end{aligned} \tag{62}$$

where set $I(S) = \{ (x,y,z) \in G : |z| = S \}$ contains the cross-sectional boundaries at $z = \pm S$. Again $\nu$ is the outward unit normal vector, $\zeta \in \mathbb{R}$ and $a_p$, $p = 1, \ldots, 2M$ given complex numbers. We see immediately that the last boundary condition in (62) requires $Y_j^S$ to coincide with given linear combination of outgoing normal mode solutions with complex amplitudes $a_p$, $p = 1, \ldots, 2M$. Operator $(\partial_\nu + i\zeta)$ is used in order to achieve continuity of stress fields in addition to continuity of displacement field.

Now we can define the functional $J_j^S$ as $L^2$-difference of numerical solution $Y_j^S$ and the given linear combination of normal modes at the truncation cross-sections:

$$J_j^S(a_1, \ldots, a_{2M}) = \int_{I(S)} \left| Y_j^S - w_j^+ - \sum_{p=1}^{2M} a_p w_p^- \right|^2 \mathrm{d}A.$$

By the definition of the problem (62) the minimizer $\vec{a}$ of $J_j^S$ is an approximation to row vector $(s_{jp})$ of the scattering matrix of the problem. It was proved in [13] that $a_k$ converges to $s_{jp}$ exponentially fast as $S \to \infty$. Qualitatively, one can quickly become convinced that the minimizer exists for $S \gg R$, and it is unique, because the waves $w_p^\pm$ and $w_j^\pm$ are linearly independent and therefore cannot be used to expressed $Y_j^S$ in many different ways.

The idea of solving the functional $J_j^S$ is to separately find solutions for problem (62) with row vectors $\vec{a}$ being zero, so that only one incoming or outgoing wave is present. Let us write the emerging problems down once more:

$$\begin{aligned} \mathcal{L}U_j^\pm(x,y,z) &= 0, \quad (x,y,z) \in G(S), \\ \nu \cdot \sigma(U_j^\pm)(x,y,z) &= 0, \quad (x,y,z) \in \partial G(S) \backslash I(S), \\ (\partial_\nu + i\zeta)U_j^\pm &= (\partial_\nu + i\zeta)w_j^\pm, \quad (x,y,z) \in I(S), \end{aligned} \tag{63}$$

where $j = 1, \ldots, 2M$. We recall that in the definition of incoming waves a cut-off function was used, so that for $j = 1$, we have $w_j^+ = 0$ on right end of domain $G(S)$. It means we have a boundary condition $\partial_\nu U_j^+ = -i\zeta U_j^+$ at that end. The boundary condition forces $U_j^+(x,y,z) = C(x,y)\exp(-i\zeta z)$ there, and we therefore have a Bloch wave solution at that cross-section of the cylinder. With the waves $U_j^\pm$ solved, the full solutions $Y_j^S$ can be written in terms of them:

$$Y_j^S = U_j^+ + \sum_{p=1}^{2M} a_p U_p^-.$$

This relation is the one where the coefficients $a_p$ can be solved. It is done by introducing $2M \times 2M$ matrices $E^S$ and $F^S$ depending on domain truncation point $S$. Matrix elements are defined as complex inner products

$$\begin{aligned} E_{ij}^S &= (U_i^- - w_i^-, U_j^- - w_j^-)_{I(S)}, \\ F_{ij}^S &= (U_j^- - w_j^-, U_i^+ - w_i^+)_{I(S)} \end{aligned} \tag{64}$$

on the two cross-sectional boundaries $I(S)$, i.e.

$$(V,W)_{I(S)} = \int_{I(S)} V(x,y,z)\overline{W(x,y,z)}\,\mathrm{d}x\mathrm{d}y.$$

Letting $G_j^S = (U_j^+ - w_j^+, U_j^+ - w_j^+)_{I(S)}$ we can write the functional $J_j^S$

$$J_j^S(a) = (a_j E^S, a_j) + 2\mathrm{Re}(F_j^S, a_j) + G_j^S,$$

where $F_j^S = (F_{j1}^S, \ldots, F_{j2M}^S)$. Now the minimizer $a_j^0(S)$ can be found from the equation

$$a_j^0(S)E^S + F_j^S = 0, \tag{65}$$

which is just a gradient of $J_j^S$ set equal to zero.

One dimensional case differs from 3D only by definition of inner products (64). They are reduced to products of point-wise differences:

$$\begin{aligned} E_{ij}^S &= (U_i^-(-S) - w_i^-(-S))(U_j^-(-S) - w_j^-(-S)) \\ &\quad + (U_i^-(S) - w_i^-(S))(U_j^-(S) - w_j^-(S)), \\ F_{ij}^S &= (U_j^-(-S) - w_j^-(-S))(U_i^+(-S) - w_i^+(-S)) \\ &\quad + (U_j^-(S) - w_j^-(S))(U_i^+(S) - w_i^+(S)). \end{aligned} \tag{66}$$

Also the scattering matrices are of size $2 \times 2$, because each 1D model can simulate only one type of wave. The abbreviation for scattering matrix method will be SM in proceeding pages of this thesis.

We conclude after the simulations that the difference between transmission coefficients calculated with BAM and SM is negligible. This serves also as a proof that both methods work and there are no errors in the program code for MATLAB. Because calculating the whole scattering matrix in 1D with SM is over four times slower than direct calculation of probability with BAM, we use only BAM in future with occasional error checks with SM.

## 5.6 Transmission coefficients in 1D

Since the 1D equations introduced in Chapter 4 approximate only one type of the modes at a time we must calculate all the modes separately. The problem is that for some particular deformation there might occur scattering from one mode type to another. Therefore it is not easy to decide whether the 1D model gives reliable approximation. For example longitudinal modes can become coupled with torsional modes if there is a twisted change in the principal axis of inertia of the fiber cross-section along the deformed part, as it can be seen if an animation of the eigenmode is constructed with COMSOL. However, with symmetrical fibers, for example if the cross-section is constantly circle, there shouldn't be significant scattering between these two mode types. We already found some evidence earlier in this chapter that a perturbation with enough symmetry should not couple different vibration modes when 3D transmission coefficients of longitudinal modes were examined.

Let us recall that as an incoming and outgoing waves at the circular ends of the fiber we use

$$\begin{aligned} w_{\mathrm{F}}^{\pm}(z) &= \exp\left(\pm i\sqrt{\sqrt{\frac{4\rho}{E}}\frac{\omega}{a}}z\right), \\ w_{\mathrm{T}}^{\pm}(z) &= \exp\left(\pm i\omega\sqrt{\frac{\rho}{\mu}}z\right), \\ w_{\mathrm{L}}^{\pm}(z) &= \exp\left(\pm i\omega\sqrt{\frac{\rho}{E}}z\right), \end{aligned} \tag{67}$$

where sub-indexes F, T and L stand for flexural, torsional and longitudinal waves. These normalized solutions were calculated from equations (41), (45) and (48) in Chapter 4.

First we shall examine the modes with lowest energy, flexural modes: In Figure 35 there are shown the transmission coefficients calculated with BAM for finite fibers of different number of periods of perturbation. Total length of the fiber changes from $110nm$ to $440\mu m$ while the diameter is $D = 2nm$. Radius of the boundary of the fiber follows cos-curve with period length $l = 10nm$ and the perturbation strength is again $\alpha = 0.251$. After the perturbed part $G(R)$ to both directions there is attached a finite straight cylinder with length $0.55R$ so that the whole length of the domain becomes $2.2 \times n \times 10nm$ where $n$ is the number of periods. Value $0.55R$ was chosen by comparing transmission coefficient curves of fibers of different lengths. The length of straigth cylinders was chosen high enough so that $\mathcal{O}(\exp(-\gamma|z|))$ in equation (52) is negligible and therefore the curves would not change much while changing the length of the domain.

For reference there are also the eigenfrequencies of similar infinitely perturbed fiber. We can clearly see that the spectral gaps from infinite model correspond to cliffs in transmission coefficient curves. Also, with more periods the cliff deepens converging asymptotically to some kind of characteristic function $\chi_{\mathrm{F}}$ of

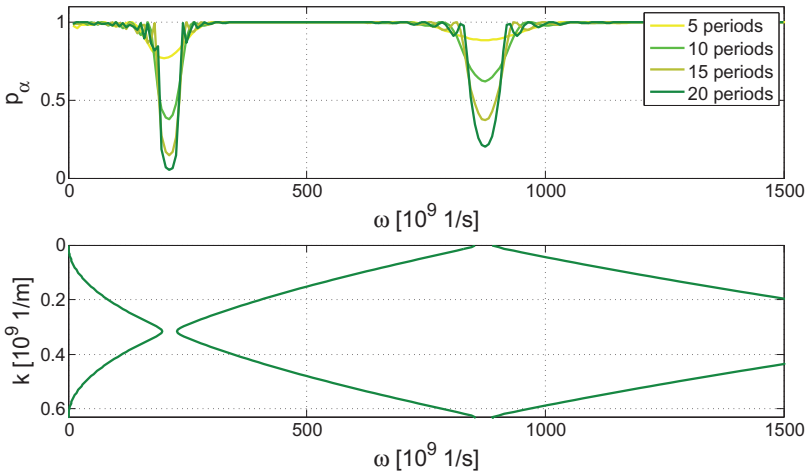


FIGURE 35 Up: Transmission coefficients $p_{\mathrm{F}}$ for flexural wave as a function of frequency $\omega$ in a perturbed cylindrical fiber with finitely many periods of perturbation. Down: Eigenfrequencies of similar infinitely perturbed fiber. Spectral gaps of infinite model seem to correspond to cliffs in transmission probability curves. At least 20 periods of perturbation is needed to decrease the probability $p_F$ close to zero in the first spectral gap.

spectral gaps, i.e.

$$\chi_{\mathrm{F}}(\omega) = \begin{cases} 1, & \text{if } \omega \text{ not in spectral gap,} \\ 0, & \text{if } \omega \text{ in spectral gap.} \end{cases}$$

These functions $\chi_\alpha$ could be used for calculating thermal conductance for infinite periodically structured fibers. This procedure was used in 1D e.g. in [28]. We will utilize it in Chapter 6 to various periodicity shapes.

One dimensional approximation of transmission coefficients for torsional modes is shown in Figure 36. Domain is again cylindrical one with axi-symmetric cos-type perturbation in the middle with strength $\alpha = 0.251$. Length of the perturbation changes from $220nm$ to $880nm$ units as the number of perturbation increases. The diameter is $D = 2nm$. There are 2,4,6 and 8 periods of perturbation in the fibers, and we can immediately see that the effect of perturbation to transmission probability is much stronger than for flexural waves. Length of period for perturbation is $l = 50nm$ and the straight cylinders after the perturbation are again $0.55R$. The cliff appearing over the spectral gap is also about as wide as the gap is. Therefore only a few periods of perturbation can be assumed to be enough for diminishing the thermal conductance for torsional waves.

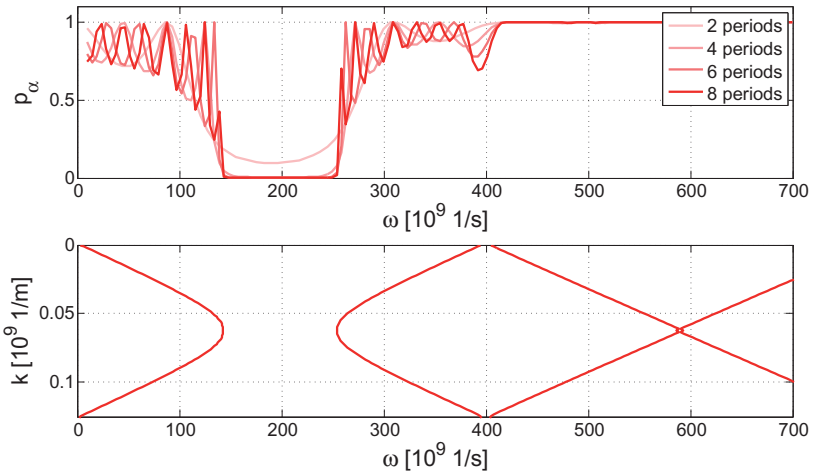


FIGURE 36 Up: Transmission coefficients $p_{\mathrm{T}}$ for torsional wave as a function of frequency $\omega$ in a perturbed cylindrical fiber with finitely many periods of perturbation. Down: Eigenfrequencies of similar infinitely perturbed fiber. Spectral gaps of infinite model seem to correspond to cliffs in transmission probability curves. Probability $p_T \approx 0$ is reached for frequencies inside the first spectral gap with eight periods of perturbation.

Similar results can be obtained with longitudinal 1D waves. In Figure 37 there are transmission coefficients of a fiber with diameter $D = 2nm$ again with 2,4,6 and 8 periods of perturbation. Length of period is now set to $l = 60nm$ and the total length therefore changes from $264nm$ to $1056nm$ as number of perturbations increase. We can clearly see that spectral gaps of infinite fiber correspond to drops in transmission probability.

We may end this section by concluding that for all the investigated phonon modes the transmission coefficient curves seem to converge to characteristic equations of spectral gaps as number of periods increases. For flexural modes there appeared considerably wide second spectral gap, which suggests that harmonic perturbation may not be the most effective choice in reflecting flexural waves. We will return to this remark in Chapter 7.

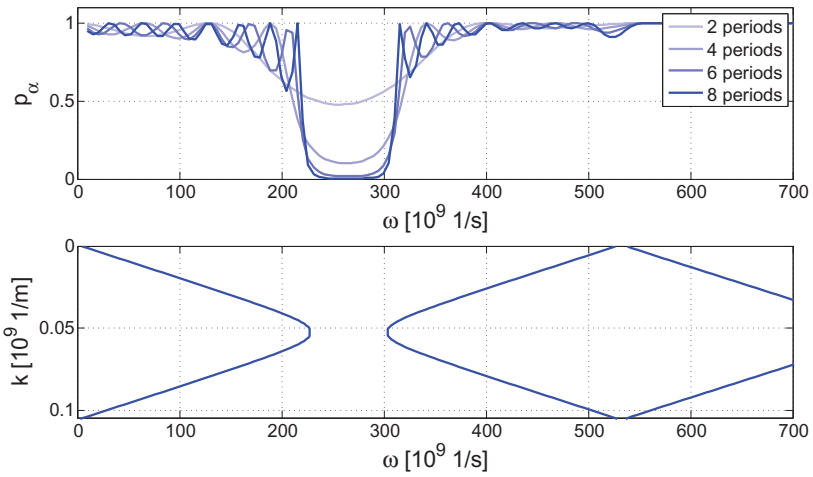


FIGURE 37 Up: Transmission coefficients $p_{\mathrm{L}}$ for longitudinal wave as a function of frequency $\omega$ in a perturbed cylindrical fiber with finitely many periods of perturbation. Down: Eigenfrequencies of similar infinitely perturbed fiber. Spectral gaps of infinite model again seem to correspond to cliffs in transmission probability curves. Probability $p_L \approx 0$ is reached for frequencies inside the first spectral gap with eight periods of perturbation.

# 6 THERMAL CONDUCTANCE

In the previous chapter we have introduced methods for calculating the transmission probability for elastic phonons of lowest energy. This information is now used to calculate the phonon thermal conductance. The formulae discussed in this chapter were successfully used by number of different research groups e.g. [29, 30, 31, 32, 33]. The numerical results were compared with experimental data by [34, 35], where a good agreement was found by calculating the thermal conductance from full dispersion relations of phonons. In our calculation we only use the low-end spectrum because the presence of higher modes is exponentially small. Regardless, we may expect a good agreement also with our results and experimental data when it is available. With this pretreatment we are now ready to introduce a formula for phonon thermal conductance. Later in this chapter we will make calculations of the thermal conductance of nanofibers with various boundary deformations. We use both finite and infinite periodical models as an example.

## 6.1 Equation for thermal conductance by acoustic phonons

Let us assume that left and right ends of the fiber are connected to reservoirs with temperatures $T_{\text{left}}$ and $T_{\text{right}}$. Thermal distribution of phonons in the reservoirs is given by Planck distribution $n_i(\omega) = 1/(\exp(\hbar\omega/k_B T_i) - 1)$. Constants $\hbar$ and $k_B$ are Planck constant and Boltzmann constant, respectively. We will be discussing here only on the thermal conductance along the fiber and neglect reflection phenomena at the joints of fiber and reservoirs. Interfaces between 2D and 1D regimes were examined e.g. in [7]. Our starting point here is one dimensional Landauer energy flux

$$\frac{\partial Q}{\partial t} = \frac{1}{2\pi} \sum_{\alpha} \int_{\omega_{\min}}^{\infty} \hbar\omega (n_{\text{left}}(\omega) - n_{\text{right}}(\omega)) p_{\alpha}(\omega) \, \mathrm{d}\omega \tag{68}$$

as in [7],[27]. Lower integration limit $\omega_{\min}$ is the cut-off frequency for phonon $\alpha$. Quantity $p_{\alpha}(\omega)$ is the transmission probability along the fiber for phonon $\alpha$. At

the first threshold the main contribution to thermal conductance is by the lowest energy acoustic modes, i.e. by phonons with $\omega_\alpha(0) = 0$. Therefore lower integration limit is $\omega_{\min} = 0$. This regime corresponds to temperatures below $1K$. Present phonon modes are the familiar flexural, torsional and longitudinal modes which have been studied in the preceding chapters. In higher temperatures than $1K$ other modes such as shear modes start to contribute to thermal conductance.

Let $|T_{\text{left}} - T_{\text{right}}| \ll \min\{ T_{\text{left}}, T_{\text{right}} \}$, so that temperature difference between reservoirs is small compared to temperature. Under this assumption, the thermal conductance can be presented in a form

$$\Omega = \frac{\partial Q/\partial t}{T_{\text{left}} - T_{\text{right}}} = \frac{\hbar^2}{2\pi k_B T^2} \sum_\alpha \int_{\omega_{\min}}^{\infty} p_\alpha(\omega) \frac{\omega^2 \exp(\beta\hbar\omega)}{(\exp(\beta\hbar\omega) - 1)^2} \, \mathrm{d}\omega \,, \tag{69}$$

where $\beta = 1/(k_B T)$ and $T = T_{\text{left}} \approx T_{\text{right}}$.

In order to understand the formula (69) better and to simplify numerical calculation we make a change of a variable: Let $X = \hbar\omega/k_B T$. The formula becomes

$$\begin{aligned} \Omega &= \frac{\hbar^2}{2\pi k_B T^2} \sum_\alpha \int_0^\infty p_\alpha \left( \frac{X}{\beta\hbar} \right) \frac{X^2 \exp(X)}{\beta^2\hbar^2 (\exp(X) - 1)^2} \frac{1}{\beta\hbar} \, \mathrm{d}X \\ &= \frac{k_B^2 T}{2\pi\hbar} \sum_\alpha \int_0^\infty p_\alpha \left( \frac{X}{\beta\hbar} \right) \underbrace{\frac{X^2 \exp(X)}{(\exp(X) - 1)^2}}_{D(X)} \, \mathrm{d}X \,, \end{aligned} \tag{70}$$

where it is easily seen how the integrand contributes to the integral. The distribution function $D(X)$ goes quickly to zero as $X \to \infty$. For example $X = 10$ implies $D(X) \approx 0.0045$. Limit at $X = 0$ is one. Therefore with variable $X$ we need to integrate only over the zone $[0, 10]$ for sufficient precision. Temperature dependence of the integral (69) is left into scaling factor of $p_\alpha$ and into coefficient $k_B^2 T/(2\pi\hbar)$. The latter multiplied by the integral of distribution $D(X)$ is known as a universal quantum of thermal conductance $\Omega_{\text{univ}}$. [7]

As we saw in the previous chapter finite periodical deformations seem to assign frequency bands where phonon propagation is mainly disturbed. These bands correspond to spectral gaps of similar infinitely perturbed fibers. In vicinity of the spectral gaps there also occurs weak resonances in the transmission probability curves which can slightly affect the phonon propagation. However, we can expect that as $\omega \to \infty$ transmission probability $p_\alpha \approx 1$. Wavelength of such waves becomes small and slowly changing boundary has no or just very little effect on them. Also, at the other end as $\omega \to 0$ the wavelength becomes long in comparison to deformed part of the fiber. Such waves do not either experience a strong potential wall caused by the perturbation. With this reasoning we may now estimate the low and high temperature limit for thermal conductance through a periodical perturbation. As $T \to \infty$ scaled transmission coefficient curve $p_\alpha(X)$ tends move towards $X = 0$. When integrating over $X$, thermal conductance becomes $\Omega = \Omega_{\text{univ}}$. Also as $T \to 0$ curve $p_\alpha(X)$ spreads to infinity in comparison to phonon distribution $D(X)$ and the integral again gives the same

result. We may later observe from the numerical simulations that for all fiber designs used here $\Omega(T)$ increases rapidly towards $\Omega_{\text{univ}}$ as $T \to 0$.

In order to diminish thermal conductance transmission probability curves should be nullified on some zone near zero. Let us take as a general objective that transmission coefficients $p_\alpha$ will be less than 0.1 on interval $[0.2, 7]$ for temperatures $T = 0.1 - 1K$ for all massless modes. At this point we do not have a reference how well different fiber designs function on this matter. Let us assume for instance that for $T = 0.5K$ we manage to reach a complete drop on transmission coefficients on interval $[0.2, 7]$. This would result to 7.7% left over of the total area $\pi^2/3$ of distribution $D(X)$ so thermal conductance would be reduced more than 10 times compared to a fiber without such forbidden band.

Let us find out which frequencies $\omega$ should be reflected in $T = 0.1 - 1K$ in order to nullify transmission probability on that particular zone. We recall from formula (70) that the change of variable was made with $X = \hbar\omega/k_B T$. Therefore $\omega = Xk_B T/\hbar$. If now $X = 0.2$ and $T = 0.1K$ then $\omega_1 \approx 2.62 \cdot 10^9\, 1/s$, and if $X = 7$ then $\omega_2 \approx 91.6 \cdot 10^9\, 1/s$. So $T = 0.1K$ requires nullified frequency band on $0.42 - 14.6GHz$. By setting $T = 1K$ we end up to frequency band multiplied by ten: $4.17 - 146GHz$. An immediate remark is that the zones are overlapping so minimum and maximum frequencies can be chosen as $Z = 0.42 - 146GHz$. However we do not yet have a reference how easily a band gap of this size can be obtained.

Looking the first spectral gap locations and widths from Figures 29 and 30 we can see that for example torsional waves can have roughly $\Delta\omega_T \approx 800 \cdot 10^9\, 1/s$ at $\omega_T \approx 1500 \cdot 10^9\, 1/s$ for a 25.1% perturbed cell with length $10nm$ and diameter $2nm$ at both ends. These frequencies can be scaled to different units of length with $\omega_{\alpha,\text{scaled}} = \omega_\alpha/a$ where $a$ is a scaling factor and $\alpha$ describes the phonon type. Scaling can be used when needed to calculate spectral gaps for thicker and longer fibers. If for example the diameter of a fiber is $10nm$ instead of $2nm$ we use $a = 5 \cdot 10^{-9}/1 \cdot 10^{-9} = 5$. For such a fiber, we would have $\omega_{T,\text{scaled}} = 300 \cdot 10^9\, 1/s$ and $\Delta\omega_{T,\text{scaled}} = 160 \cdot 10^9\, 1/s$. These quantities fall into frequency range $Z$. Therefore we can predict that fibers with diameter $10nm$ and periodicity cells with length $50nm$ could be used for reducing phonon thermal conductance at low temperatures. We will consider the scaling of spectral gap frequencies in more detail in the following chapter.

## 6.2 Infinite periodical fibers

We recall from previous chapter the claim that thermal conductance can be calculated with characteristic functions $\chi_\alpha$ of frequency spectra for different modes. These functions are defined with

$$\chi_\alpha(\omega) = \begin{cases} 1, & \text{if } \omega \text{ not in spectral gap of phonon } \alpha, \\ 0, & \text{if } \omega \text{ in spectral gap of phonon } \alpha, \end{cases} \tag{71}$$

for phonon modes $\alpha$. Such a characteristic function can be formed by first calculating the 3D frequency spectrum for some periodicity cell and then identifying the spectral gaps for different modes with mode recognition algorithm. If the periodicity cell has enough symmetry in its geometry then the modes should remain mainly flexural, torsional or longitudinal.

Assume that we manage to design a cell that nullifies the transmission coefficients for $T = 0.5K$ on range $X = 0.2 - 7$. This range corresponds to frequencies $2 - 73GHz$. We shall examine how this affects the thermal conductance on wider temperature range $T = 0.1 - 10K$. In Figure 38 we can compare the scaled

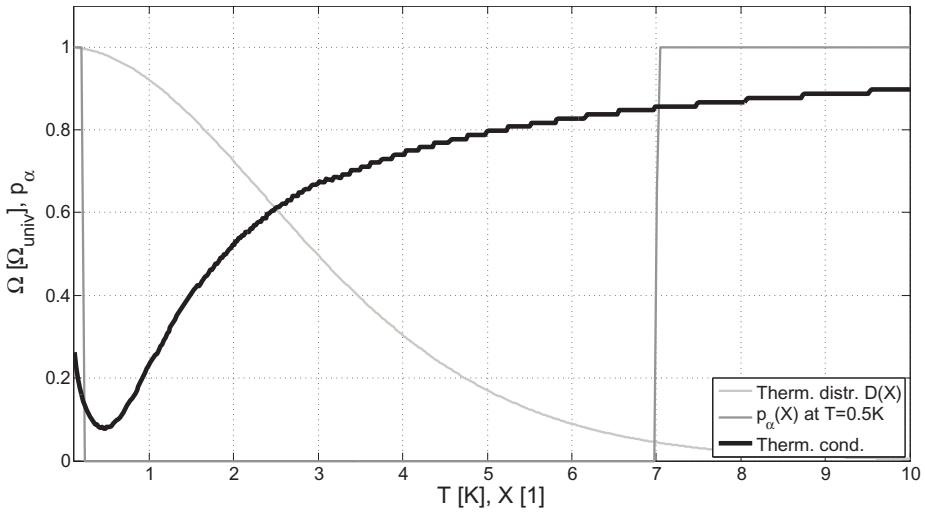


FIGURE 38 Normalized thermal conductance of an ideally designed periodical nanofiber with forbidden band set to $2 - 73GHz$ on temperature range $T = 0.1 - 10K$. As a reference a scaled characteristic function of spectral gaps in units of $X$ at $T = 0.5$. Thin grey curve shows the shape of the scaled phonon distribution $D(X)$.

transmission coefficient curve to thermal distribution of phonons as a function of scaled frequency parameter $X$ and see how the thermal conductance is changed. Thermal conductance is presented as a function of $T$ with thick black curve, and it is normalized into units of universal quantum $\Omega_{\text{univ}}$. We immediately notice that at $T = 0.5K$ such transmission coefficient curve indeed provides over 10 times smaller thermal conductance as was calculated in previous section. However as temperature changes transmission coefficient curve is rescaled to edges of zone $Z$ and more mass of $D(X)$ is left over to contribute to thermal conductance. When $T$ increases $p_\alpha$ is scaled left and when $T$ decreases $p_\alpha$ is scaled right. This is the reason why $\Omega$ increases as $T$ changes from $0.5K$. Thermal conductance at $T = 0.1K$ or $T = 1K$ is still roughly 20% of the corresponding value for unperturbed cylin-

der.

After simulating the thermal conductance of a few infinite periodical 3D models we conclude that a typical harmonic axi-symmetrical perturbation can result into 30% drop in thermal conductance for longitudinal or torsional waves at $T \approx 0.5K$ if the length:diameter ratio is chosen ideally for these modes. Usually, contributing flexural waves travel through such perturbation without trouble. If the boundary curve of axi-symmetrical perturbation is more complex, e.g. has a shape of smoothed sawtooth wave which is constructed as a superposition of multiple shorter wavelengths, we obtained 10% drop in thermal conductance for flexural waves at temperature range $T = 0.1 - 1K$, and at the same time, $10 - 30\%$ drop for torsional and longitudinal waves on temperature range $T = 1 - 3K$. The results are shown in Figure 39. For the reference there is also shown a 3D

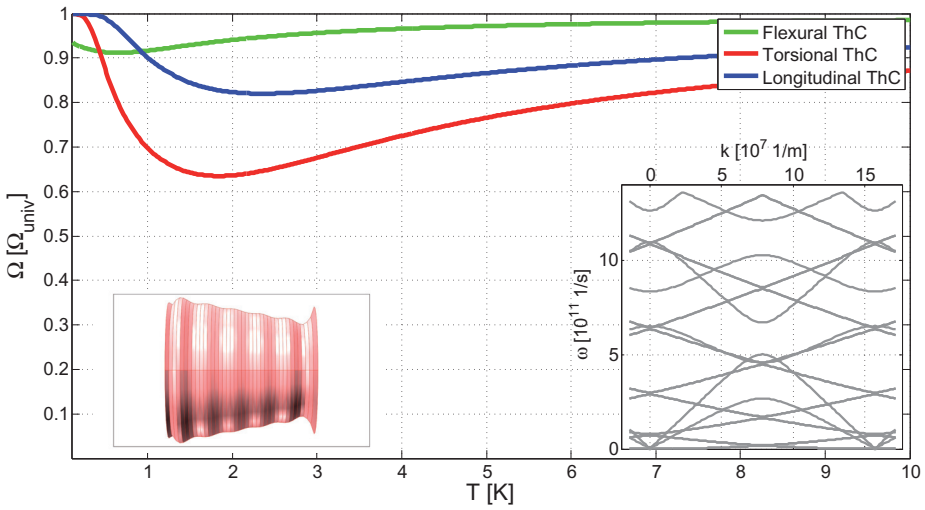


FIGURE 39 Thermal conductance by flexural, torsional and longitudinal modes in a periodical silicon fiber with smooth sawtooth-shaped periodicity cell. Length of the cell $l = 40nm$ and diameter at the ends $D = 2nm$. Inset pictures show the shape of (horizontally scaled) periodicity cell and a 3D frequency spectrum of the cell.

frequency spectrum of the cell.

We may predict that somewhat higher decrease in thermal conductance of infinite periodical fibers can be obtained with using form optimization methods to design the periodicity cell. Also, it should be possible to find a single geometry which considerably lowers the thermal conductance of all three modes at range $T = 0.1 - 1K$.

## 6.3 Finite periodical fibers

Let us now consider thermal conductance of finitely perturbed fibers. We will fix here a geometry for a typical finitely periodical fiber and calculate the complete thermal conductance through it. In Figure 40 we present first calculations of ther-

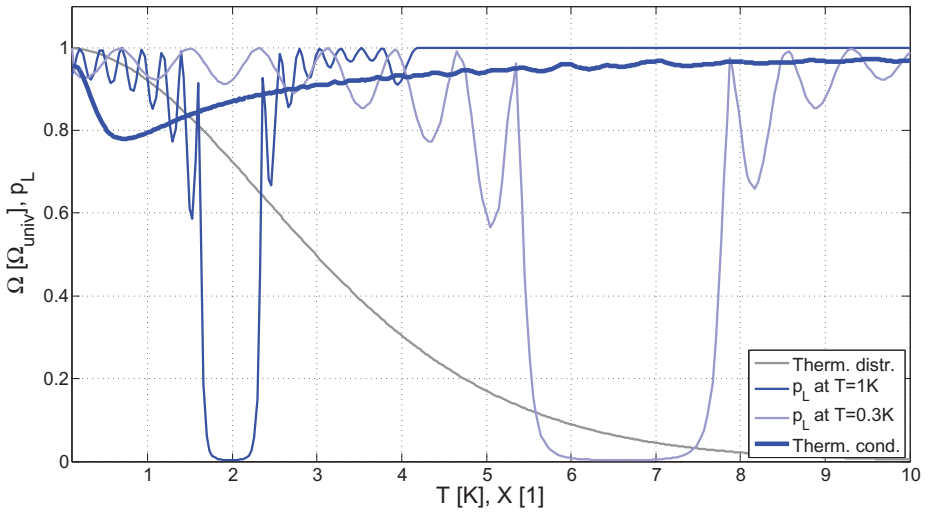


FIGURE 40 Normalized thermal conductance of 1D longitudinal waves on temperature range $T = 0.1 - 10K$ in a finite fiber with eigth periods of harmonic perturbation. Geometry parameters are $l = 60nm$, $D = 2nm$ and $\alpha = 0.251$. The scaled transmission probability curves at $T = 1K$ and $T = 0.3K$ show how they are shifted to right when temperature decreases. Grey curve shows the shape of the scaled phonon distribution $D(X)$.

mal conductance by longitudinal waves in a cylindrical fiber with $n = 8$ periods of harmonic perturbation on the boundary. Thermal conductance is again normalized to units of universal quantum of thermal conductance so that it is comparable with thermal conductance of a straight prismatic cylinder. It is presented with thick blue curve in the figure. Period length of the perturbation is the same $l = 60nm$ as in some of the previous examples in last chapter. Gray curve corresponds to distribution function $D(X)$ in the integral (70) and thin blue curves show the scaled transmission probabilities of longitudinal waves for two different temperatures. The fiber under inspection is $960nm$ long and has a diameter of $2nm$. The thick blue curve shows that for a fiber with the described boundary shape there is approximately 80% thermal conductance by longitudinal waves on range $T = 0.5 - 1K$ compared to conductance of unperturbed cylinder. If larger temperature range $T = 0.1 - 10K$ is observed one can say that the thermal con-

ductance by longitudinal waves is lowered approximately 5%.

To obtain a complete picture of the thermal conductance one must calculate and sum the corresponding curves for torsional and flexural modes in the same geometry. In Figure 41 there are shown normalized thermal conductances

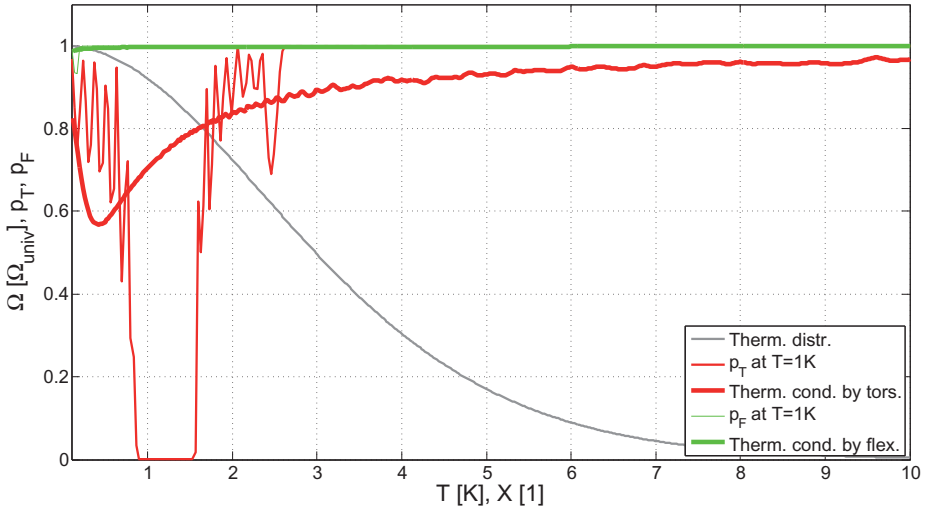


FIGURE 41 Normalized thermal conductivities by 1D torsional and flexural waves in a finite fiber with eight periods of harmonic perturbation on temperature range $T = 0.1 - 10K$. Geometry parameters are $l = 60nm$, $D = 2nm$ and $\alpha = 0.251$. Also drawn are the transmission probability curves $p_F$ and $p_T$ with a scaled phonon distribution $D(X)$.

by torsional and flexural waves, torsional with red and flexural with green as before. We can see, by comparison with previous figure, that perturbation of period length $l = 60nm$ affects the propagation of torsional waves at $T = 1K$ such a way that thermal conductance is lowered noticeably more. However, flexural waves are not affected by the perturbation because their wavelengths at $T = 1K$ are much shorter. Thermal conductance by flexural waves drops only slightly as $T \to 0K$. By choosing $T = 0.5K$ we can now calculate the total thermal conductance with

$$\Omega = (0.8 + 0.6 + 1 + 1) \cdot \Omega_{\text{univ}} \approx 1.6 \cdot 10^{-12}\, W/K.$$

Final remark of this chapter is that cliffs in transmission probability curves for different mode types did not effectively cover the main part of distribution function $D(X)$ where there is most of the area. In order to diminish thermal conductance one must widen the cliffs of transmission probability curves so that the integrand in (69) is close to zero on wider range. This is the topic in next chapter: How to design a fiber that has strongly reduced total thermal conductance on given low-level temperature interval?

# 7 DESIGNING THE PERTURBATION

Now that we are able to calculate low-level thermal conductance of deformed dielectric nanofibers with 1D models we can study how to execute the perturbation so that total thermal conductance would have desired properties. We continue to work with silicon (Si) as a material keeping in mind the nearest applications for fiber shape design. There are still several questions to be answered concerning the design: How to affect the propagation of all of the phonon modes that are present? How many periods should there be in the perturbation? What should be the strength of the perturbation? How to make forbidden band wider for different phonon types? The last problem will be the one we are answering first.

## 7.1 Chirped fibers

There are at least a couple of solutions to problem how to widen the forbidden band for phonons. First is to build so-called chirped structure. One can think that in a chirped fiber perturbation is almost periodical, so that the length of period is slightly changing when moving along the fiber. In a chirped fiber there will be correct lengths in perturbation to reflect back phonons from wider frequency band than in regular fiber with constant length of period. In chirped fibers the ratio between lengths of neighboring periods $L_i$ and $L_{i+1}$ should be kept constant, so that the density of lengths would be constant. Then, if we examine two phonons of type $\alpha$ with slightly different frequencies $\omega_1 \approx \omega_2$, we can assume that they experience approximately the same potential barrier from the perturbation and share approximately the same transmission probability. Therefore we define $L := L_{i+1}/L_i \geq 1$ to be called *period ratio*. With the number of periods $n$ and period ratio $L$ known in the perturbation we can calculate ratio between lengths of the first and the final period:

$$C := \frac{L_n}{L_1} = \frac{L_n}{L_{n-1}}\frac{L_{n-1}}{L_1} = \ldots = \frac{L_n}{L_{n-1}} \cdots \frac{L_2}{L_1} = L^{n-1}. \tag{72}$$

This quantity will be called *chirp ratio*. If period ratio $L$ is close enough to one and number of periods $n$ high enough then it can be assumed that forbidden band becomes wider and transmission probability in the gap stays zero or close to zero. However if $L$ goes too high there will be resonance effects for phonons inside the band gap and cliffs in transmission coefficient curve start to fill up. We can use here as a reference the final section of Chapter 5 where it was found that eight periods of constant perturbation was enough for torsional and longitudinal modes to be fully reflected on some small frequency interval. When there was less periods available the transmission probability did not reach small enough values. Flexural waves appeared to require little more than 20 periods to be reflected with the same probability.

We continue by constructing an analytical description of the boundary curve. Function $B$ in (35) will be changed a bit for chirped structures. We put as an argument for cos-function another function $\Lambda = \Lambda(z)$

$$B(z) = \left\{ 1 - \frac{1}{2}\left[1 + \operatorname{sign}\left(R - |z|\right)\right] \frac{1}{2}\left[1 + \cos\left(\pi + 2\pi\Lambda(z+R)\right)\right] \alpha \right\}, \qquad (73)$$

which scales the zeros of cos-function so that period ratio $L$ is obtained. For simplicity let us use notation

$$\Sigma(m) := \sum_{i=0}^{m-1} L_1 L^i,$$

with $\Sigma(0) = 0$. This is the usual geometric series. Real number $R$ in the formula (73) is the half-length of the perturbation, as in Figure 2. It can be calculated from number of periods $n$ and period ratio $L$ with $R = \frac{1}{2}\Sigma(n)$. Function $\Lambda$ is constructed in a following way: It has support on $[0, 2R]$ and it is equal to zero elsewhere. It must have a property $\Lambda(\Sigma(m)) = m$, on $[0, 2R]$, so therefore it is inverse function of $\Sigma$. We follow a known procedure for finding the inverse of geometric series. Multiply the definition of $\Sigma(m)$ by $(1 - L)$:

$$\begin{aligned}
(1-L)\sum_{i=0}^{m-1} L_1 L^i &= (1-L)L_1(L^0 + L^1 + \ldots + L^{m-1}) \\
&= L_1(1 - L^m) \\
\implies \Sigma(m) &= \sum_{i=0}^{m-1} L_1 L^i = L_1 \frac{1-L^m}{1-L}.
\end{aligned}$$

This form can be inverted analytically and we finally end up to

$$\Lambda(z) = \log_L\left(1 - \frac{z(1-L)}{L_1}\right) = \frac{\log\left(1 - \frac{z(1-L)}{L_1}\right)}{\log L}.$$

Now that we have an analytic form for boundary curve of chirped fiber we would like to decide which period lengths should be present in the perturbation. Our goal is still the same: to reach 90% drop in thermal conductance for temperatures $T = 0.1 - 1K$. As stated before the mainly contributing phonons should

TABLE 1 Wavelengths for different phonon types in silicon wire of diameter $10nm$ for frequency range $0.41 - 146GHz$, which was calculated to provide 90% drop in thermal conductance if the transmission probability of such waves is nullified.

| Phonon $\alpha$ | $c_\alpha$ $[m/s]$ | $\lambda_{\min,\alpha}$ $[10^{-9}m]$ | $\lambda_{\max,\alpha}$ $[10^{-6}m]$ |
|---|---|---|---|
| Flexural | 222-4144 | 28.4 | 0.53 |
| Torsional | 4705 | 32.3 | 11.3 |
| Longitudinal | 7498 | 51.4 | 18.0 |

have frequencies in zone $Z := 0.41 - 146GHz$. Knowing the frequencies, we can make quick approximations on the wavelengths for different phonons with equation

$$\lambda_\alpha = 2\pi \frac{c_\alpha}{\omega}. \tag{74}$$

The phase velocity $c_\alpha$ for each phonon type can be taken from 1D equations (41), (45) and (48) from Chapter 4. For longitudinal and torsional waves we simply get

$$c_L = \sqrt{\frac{E}{\rho}}, \qquad c_T = \sqrt{\frac{\mu}{\rho}}.$$

The wave speed of these modes is independent of frequency. They are said to propagate non-dispersively. For flexural waves the equation is just a bit problematic, because there is angular frequency $\omega$ and parameter $a$ describing the radius of the fiber present in the equation (42). Dependence on $\omega$ results into dispersive wave propagation, as

$$c_F = \omega/\zeta = \sqrt{\omega a \sqrt{\frac{E}{4\rho}}}.$$

Because $a$ was assumed to be independent of $z$ we are essentially calculating the flexural wavelength in an unperturbed fiber. Dispersion of flexural waves can be tried to explain physically so that changing the perturbation strength $\alpha$ affects the fiber *bending stiffness* $EI(z) \sim B(z)^4$ more than it affects the cross-sectional mass $\rho A(z) \sim B(z)^2$. Recalling quickly from Figure 26 that flexural gap location is a decreasing function of perturbation parameter $\alpha$ we can only expect to approximate the gap location with this formalism. If $\alpha \approx 0$ is small, then we can anticipate a good approximation.

With the wave speeds and the frequency range we can now calculate the wavelengths of phonons in a fiber. Let us fix the unperturbed diameter at $D = 10nm$. Then $a = 5nm$, and we can express the calculated wavelengths in a Table 1. Now, going back to Figure 31 in Chapter 5 we can make some visual interpretations about the scattering process. The frequency of the incoming wave was chosen in the middle of the spectral gap of similar infinitely perturbed fiber. We can see that the wavelength is about double the wavelength of the perturbation functions $B_x$ and $B_y$. This suggests that the perturbation wavelength should be half of the phonon wavelength. With the previous formulae this can be easily

checked, as one can take for example parameters $l = 300nm$, $a = 10nm$ and $\omega \approx 0.5 \cdot 10^{11}\, 1/s$ from Figure 25 for torsional wave band gap, and calculate

$$\lambda_T = 2\pi\sqrt{\frac{\mu}{\rho}}\frac{1}{\omega} \approx 591nm \approx 2 \cdot l.$$

Also, while considering flexural waves, one might want to confirm that the formulas correspond the numerical results. Let $l = 10nm$ and $a = 1nm$ as in Figure 26. Let $\alpha \approx 0$ and we can read spectral gap frequency $\omega \approx 360 \cdot 10^9\, 1/s$ from the figure. Then we calculate

$$\lambda_F = 2\pi\frac{\sqrt{\omega a\sqrt{\frac{E}{4\rho}}}}{\omega} \approx 20.3nm \approx 2 \cdot l.$$

For longitudinal waves the formula works similarly. The conclusion is therefore that given the phonon wavelengths in Table 1 one should half them and use the obtained values as the period of perturbation in the definition of boundary curve.

There is yet another important parameter to set when designing a chirped structure. It is the number of periods $n$ which is sufficiently small so that total length of fiber does not rise too much while transmission coefficients are still effectively nullified. This can be analyzed independently for different vibration types by fixing the chirp ratio $C$ according to minimum and maximum wavelengths that are wanted to be reflected and let the number of periods increase. Period ratio decreases as a function of number of periods. This way a 3D surface of transmission coefficients can be drawn as a function of number of periods $n$ and frequency $\omega$ in order to decide the best value for $n$ which should be used in calculations for thermal conductance. We will demonstrate the use of such a 3D surface in next sections.

## 7.2 Fibers with cylindrical chirped deformation

Let us first consider longitudinal motion. To reflect longitudinal waves we have to construct a very long fiber which tests the limits of numerical accuracy of basic table-top computer. Even if we choose narrower bandwidth than $Z$ for longitudinal wavelengths with first period $L_1 = 30nm$ and chirp ratio $C = 160$ the resulting fiber can be over $100\mu m$ long. The smallest details have therefore length:diameter ratio $3:1$ and we need there at least $10-20$ FEM-nodes in every period to obtain numerically accurate results. As period length increases moving along the fiber, we cannot make the node grid much more sparse because otherwise it would result into loss of detail for high frequency waves. With high number of periods $n$ we easily ended up to almost maximal number of FEM-nodes for the computer used in simulations.

In Figure 42 there is shown a 3D graph of transmission coefficients as a function of number of periods $n$ and frequency $\omega$. This type of 3D graph is similar

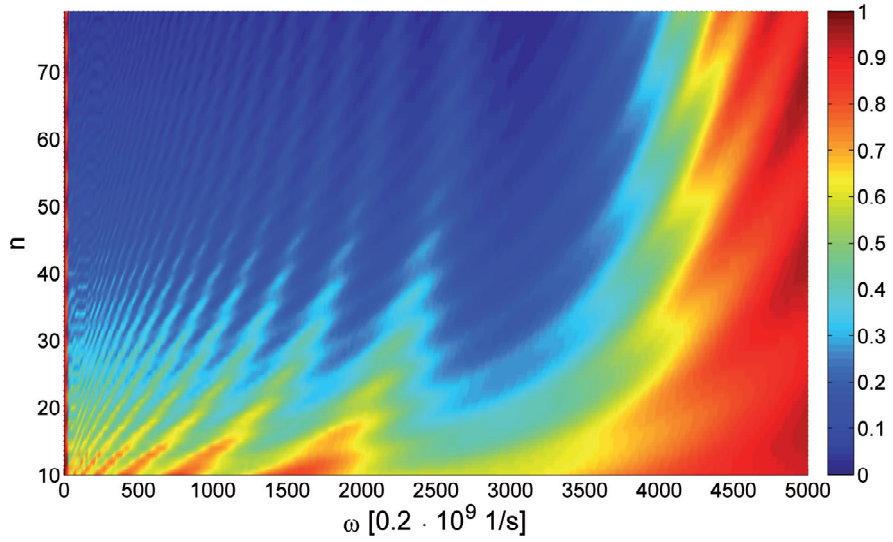


FIGURE 42 Transmission coefficients of 1D longitudinal waves for variable number of perturbations in Silicon fiber with diameter $10nm$. First period $L_1 = 30nm$ and chirp ratio $C = 160$, so that last period is always $L_n = 4.8\mu m$. Period number $n$ changes from $10 - 79$. We can notice that transmission probability decreases almost uniformly on frequency band $2.4 - 127GHz$ as $n$ increases.

to one used in [30]. Let us first examine visually how many periods should be used to reflect longitudinal waves. The darker blue area which becomes visible after $n \geq 70$ can be estimated to diminish transmission probability under 0.1 for frequency range $2.4 - 127GHz$ and we can therefore use a value for $n$ from that scale. Let $n = 80$ for instance.

Now, in Figure 43 we show the thermal conductance by 1D longitudinal waves with the scaled transmission coefficient curve at $T = 1K$ with the chosen geometry parameters. First remark of the parameters is that the total length of the fiber $2 \cdot S = 107\mu m$ is still many times smaller than phonon free length in Silicon at low temperature, $T < 10K$. Therefore these parameters are physically reasonable. In the inset picture there is shown the boundary curve of the fiber.

Length of boundary cylinders was set to $0.7 \cdot R$ where $R$ is the half-length of perturbed part of the fiber. It was checked that reducing the length of boundary cylinders does not visibly affect the result. We can perceive from Figure 43 that on temperature interval $T = 0.2 - 1K$ longitudinal thermal conductance is reduced to $1/10$ of the one for prismatic cylinder. We also remark that the scaled transmission coefficient curve at $T = 1K$ near $X \approx 8.7$ rises over 1. This phenomenon can

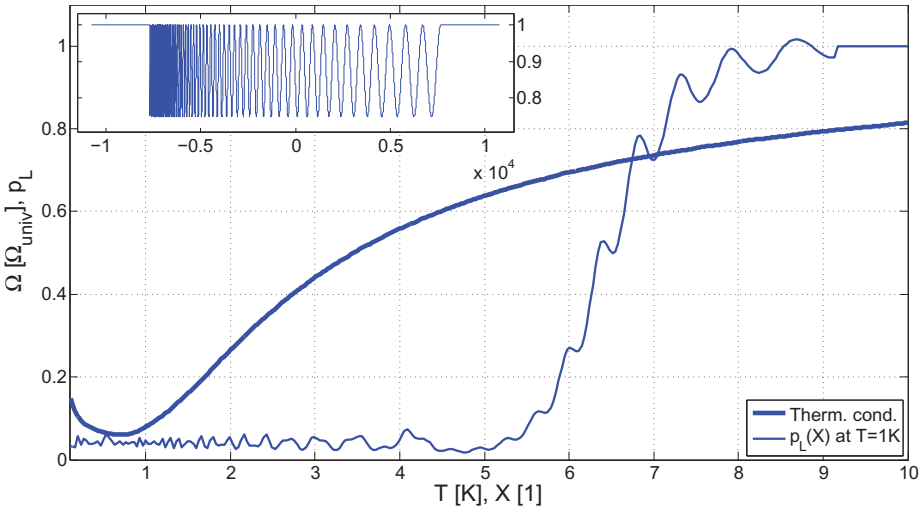


FIGURE 43 Thermal conductance by longitudinal waves in $107\mu m$ Silicon fiber with diameter $10nm$. Transmission coefficient $p_L(X)$ at $T = 1K$. Inset picture: Boundary curve $B(z)$ for chirped fiber with 80 periods of cos-type perturbation with first period $L_1 = 30nm$, chirp ratio $C = 160$ and period ratio $L = 1.0664$.

be explained with numerical inaccuracy because corresponding frequencies are high compared to mesh resolution. The thermal conductance reached only 80% drop at $T = 0.1K$ because we decided to cut out the longest periods of deformation. However, it can be immediately concluded that 90% drop can be reached at $T = 0.1K$ or even lower by using longer fiber models.

For torsional waves we intend to use the same perturbation as for longitudinal waves. We can predict, by refering to similarities of spectral gap locations, that this design would reflect torsional modes approximately with the same efficiency as longitudinal waves. In Figure 44 we show the results of calculation. The thermal conductance by torsional waves reaches over 90% drop on the whole temperature range $T = 0.1 - 1K$. One remark on the scaled transmission probability curve presented in the figure is that for high frequencies $X \geq 6$ the numerical error results into $p_T(X) \geq 1$. This does not have a great impact on thermal conductance because the distribution $D(X) \approx 0$ on that region. Therefore we can neglect this error.

For flexural waves 1D design is even more complex in numerical sense than it is for longitudinal waves because the fourth order equation must be used in simulation. Therefore we have two dependent variables for UMFPACK solver and in order to maintain the same numerical accuracy number of degrees of freedom is doubled to 122882. This is roughly the highest possible with the computer

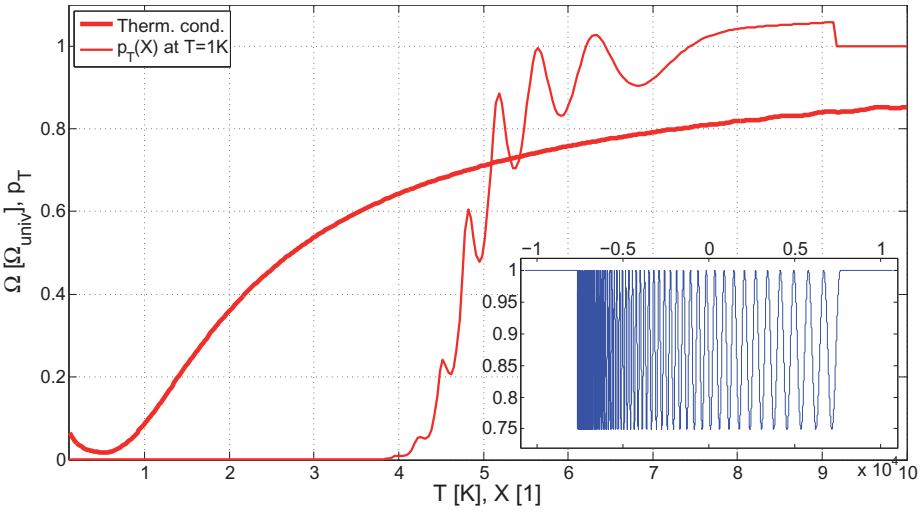


FIGURE 44 Thermal conductance by torsional waves in a Silicon fiber of length $107\mu m$ and diameter $10nm$ as a function of temperature. Scaled transmission coefficient $p_T(X)$ at $T = 1K$. Inset picture: Boundary curve $B(z)$ for chirped fiber with 80 periods of cos-type perturbation with first period $L_1 = 30nm$, chirp ratio $C = 160$ and period ratio $L = 1.0664$.

setup used in simulations. In order to reflect high frequency flexural waves the period length must be very small. As before the perturbation was of cos-type with perturbation amplitude $\alpha = 0.251$. We used value $L_1 = 15nm$ for the first period of perturbation. This value is close to half of approximated minimum wavelength of flexural waves that mainly contribute to thermal conductance in $T \approx 1K$. Nevertheless, unlike for torsional and longitudinal waves, periodical perturbation creates a considerably wide second spectral gap for flexural waves. We intend to use this phenomenon even that we clearly verify from frequency spectra that 1D model used has significant error near the second spectral gap. However 1D approximation near the second gap seems to be always higher than corresponding gap from 3D spectrum so we may trust that given a slow and long enough perturbation the 1D model approximates 3D transmission coefficient curve from above.

Moreover, because flexural waves are not interfered as much as longitudinal or torsional wave by this type of perturbation we used a small value for period ratio $L = 1.005$. This value was chosen from comparison of transmission coefficient graphs for different parameters. Number of periods is 350 and the chirp ratio is therefore only $C = 5.7011$. We remark that increasing a perturbation parameter $\alpha$ in order to use less periods of perturbation would harm structural properties of the fiber. It is clear that for axi-symmetrical case tensile strength

depends on the minimum value of the area of cross-section of the fiber. In Figure 45 we show the flexural wave thermal conductance obtained with given param-

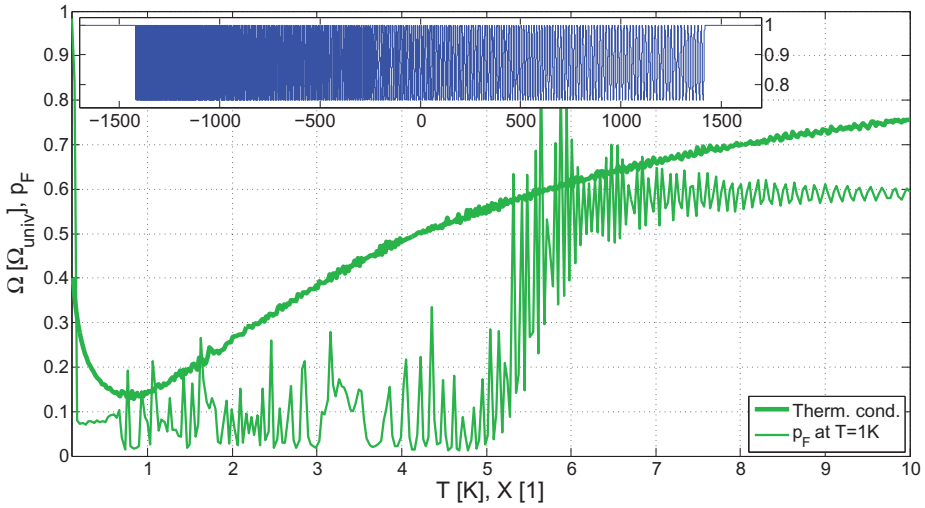


FIGURE 45 Inset picture: Boundary curve $B(z)$ for chirped fiber with 350 periods of cos-type perturbation with period ratio $L = 1.005$. Other geometry parameters are $L_1 = 15nm$, $D = 10nm$ and $\alpha = 0.251$. Thich green curve shows the calculated thermal conductance by flexural waves. Thin green curve is the scaled transmission probability $p_F(X)$ at $T = 1K$.

eters. For reference there is also shown the boundary curve in the inset picture and scaled transmission coefficient $p_F(X)$ in the main graph. It is interesting to see how the second spectral gap contributes to thermal conductance of flexural waves. From $X \geq 5$ we have $p_F(X) \approx 0.6$. These frequencies do not play a major role in temperatures under $1K$. Even with all the efforts done we notice that flexural thermal conductance does not reach the desired $1/10$ of the universal thermal conductance on temperature range $T = 0.1 - 1K$. Also, because the chirp ratio of the perturbation was only a fraction of what it was for longitudinal and torsional waves, we can understand why it seems that $p_F(X) \to 1$ much quicker than $p_L$ and $p_T$ for $X \approx 0$. Clearly, being able to use boundary curves with more periods one can confidently assume that 90% drop can be obtained with cos-type cylindrical perturbation. However, there is another solution to the problem and we intend to describe it next.

## 7.3 Elliptical balanced deformation for reflecting flexural waves

In order to use stronger amplitude of perturbation for reflecting flexural waves with less number of periods we introduce an elliptical deformation which is balanced so that the cross-sectional area remains constant. With area of cross-section staying constant longitudinal modes should propagate almost freely through the perturbation. This hypothesis can be made because 1D model for longitudinal waves depends only on the area of cross-section. Torsional modes are also expected to remain mostly intact because area moment of inertia, which contributes in torsional 1D equation, does not change much between circular and elliptical cross-section. We also intend to use elliptical deformation with periodically chirped setup. Elliptical deformation will be constructed so that function $\Lambda$, which scales the zeros of cos-function into a geometric series, is usable again.

Starting with the assumption that area of cross-section is constant we have for elliptical case $A = \pi B_x(z)B_y(z)$ where the boundary curves $B_x$ and $B_y$ act as elliptical semi-axes. To obtain a domain with constant cross-sectional area we can set for example $B_x \sim 1 + \alpha \sin$ when $B_y \sim 1/(1 + \alpha \sin)$. However, this does not form a symmetrical perturbation so that $x$- and $y$-polarized flexural waves would experience the same potential wall. To revise this, we recall that $\Lambda$ was built to map one period $[\Sigma(m), \Sigma(m+1)]$ to $[m, (m+1)]$. Therefore, we can again use sin-curve as a perturbation so that on $D_{\mathrm{l}}^m := [2\pi m, 2\pi m + \pi]$ it is defined normally and we invert it on $D_{\mathrm{r}}^m :=]2\pi m + \pi, 2\pi(m+1)]$. Boundary curve $B_y = 1/B_x$ will then have otherwise equal shape except that order of $D_{\mathrm{l}}^m$ and $D_{\mathrm{r}}^m$ is reversed. By defining the boundary curves with alternating the inversion, $x$- and $y$-polarized flexural waves will share the same frequency spectrum. This claim will be verified shortly. Function $\Lambda$ was defined on $[0, \infty[$ so we must use periodical cut-off function for $D_{\mathrm{l}}^m$ and $D_{\mathrm{r}}^m$. The periodical cut-off function $\psi$ is defined by

$$\psi(z) = \frac{1}{2}(1 + \operatorname{sign}(\sin z)).$$

Now we can set for balanced sin-type function $S = S(z)$

$$S(z) = \psi(z)(1 + \alpha \sin z) + \psi(z + \pi)\frac{1}{(1 + \alpha \sin z)},$$

where $\alpha$ is the amplitude parameter of the perturbation. First term in the sum has support on $D_{\mathrm{l}}^m$ and the other term on $D_{\mathrm{r}}^m$. Boundary curves $B_x$ and $B_y$ are defined with

$$B_x(z) = \frac{1}{2}(1 - \operatorname{sign}(R - |z|)) + \frac{1}{2}(1 + \operatorname{sign}(R - |z|))S(2\pi\Lambda(z + R)) \qquad (75)$$

and $B_y = 1/B_x$.

In Figure 46 we show the frequency spectrum of elliptical balanced fiber. Length of period is $l = 50nm$ and diameter $D = 10nm$ at the circular boundaries. Parameter $\alpha$ controlling the perturbation is set to $\alpha = 0.7$. It controls

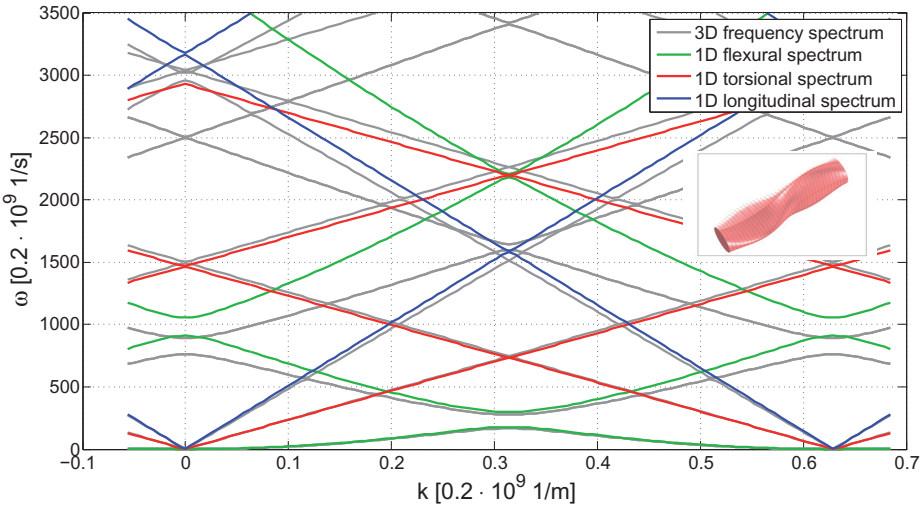


FIGURE 46 Comparison of 3D and 1D frequency spectra of infinite periodical elliptically perturbed balanced fiber. Periodicity cell of the fiber is shown in the inset picture. Period length is $l = 50nm$ and diameter of the cell at circular boundaries is $D = 10nm$. Strength of perturbation is $\alpha = 0.7$. We can notice comparably wide spectral gaps for flexural waves at $\omega_1 \approx 50 \cdot 10^9\, 1/s$ and $\omega_2 \approx 180 \cdot 10^9\, 1/s$.

the maxima of boundary curve so that in each elliptically squeezed spot maximal radius on the major semi-axis is $1 + \alpha$. Minor axis is inverse of that number: $1/(1 + \alpha)$. As it can be seen from inset picture the periodicity cell looks extremely strongly squeezed. We can immediately say by examining the spectrum that 3D model does not reveal noticeable spectral gaps for torsional or longitudinal waves. There is only one gap for longitudinal waves that is visible and it is located at the second cross-section of longitudinal wave spectra. One dimensional models for longitudinal and torsional vibration agree very well with 3D model even in this strongly perturbed case. Only the slope, i.e. the speed of 1D waves is slightly different than the corresponding value from 3D graph. The second 3D longitudinal spectral gap for $k = 0$ and $\omega \approx 600 \cdot 10^9\, 1/s$ does not show in 1D approximation, but this error can be neglected because we are focusing mainly on first spectral gaps. There are some spectral gaps visible for flexural waves, and we observe by examining them that 1D approximation should work as well as it does for cylindrical domain. The error increases in similar fashion as frequency of the wave increases. Therefore we can assume that 1D simulation of transmission coefficients for elliptical periodically perturbed fibers is as accurate as it is for cylindrical fibers.

Let us now calculate the thermal conductance for chirped elliptically per-

turbed domain. We put as first period $L_1 = 20nm$ in a fiber with diameter $D = 10nm$. This setting of $L_1$ is slightly more than half of the approximated minimum flexural wavelength $\lambda_{F,\min} = 28.4nm$ for reflected frequency zone $Z$. Again, we can use the second spectral gap to reflect high frequency flexural waves. Let chirp ratio $C = 6.8$ and let number of periods increase from $n = 10$ to $n = 69$. In Figure 47 we present similar 3D graph as for longitudinal waves in last section.

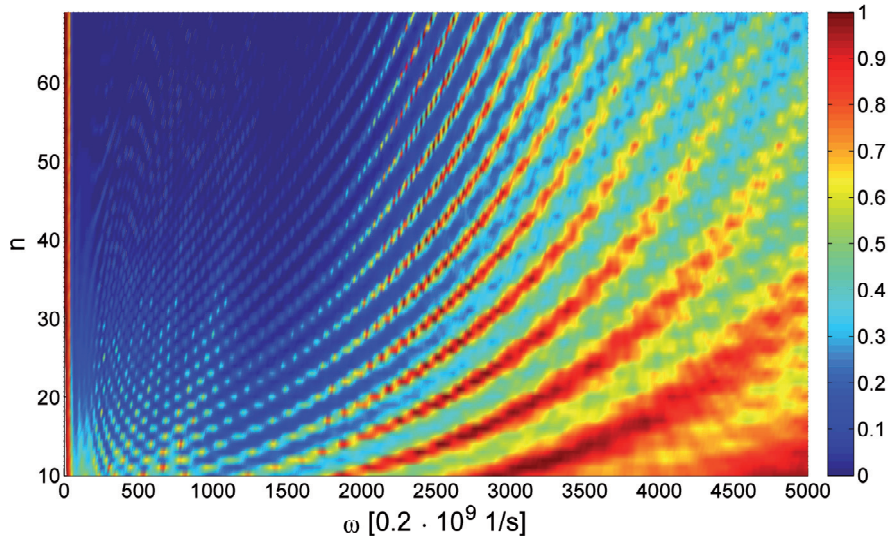


FIGURE 47 Transmission coefficients of 1D flexural waves for variable number of elliptical balanced perturbations in silicon fiber with diameter $10nm$. First period $L_1 = 20nm$ and chirp ratio $C = 6.8$, so that last period is always $L_n = 136nm$. Number of periods $n$ changes from $10 - 69$. We notice that transmission probability decreases almost uniformly on band $2.4 - 70GHz$ as $n$ increases. On the band $70 - 159GHz$, which is "governed" by second flexural gap, the decreasing is slower and there appear resonances.

We can see that there are more resonance spikes than there is for longitudinal waves but althogether the picture looks the same. Increasing number of periods does not affect much to transmission probability after $n \geq 50$ so we can decide that best number for $n$ is 50. Total length of the fiber then becomes $4.3\mu m$.

Now, with the parameters chosen for a chirped structure we show the thermal conductance by flexural waves in Figure 48 together with the scaled transmission probability curve at $T = 1K$. Inset picture shows the form of boundary curve $B_x$. First impression of the curves is that elliptical fiber with such a pronounced deformation reflects flexural waves very well. It seems to be easy

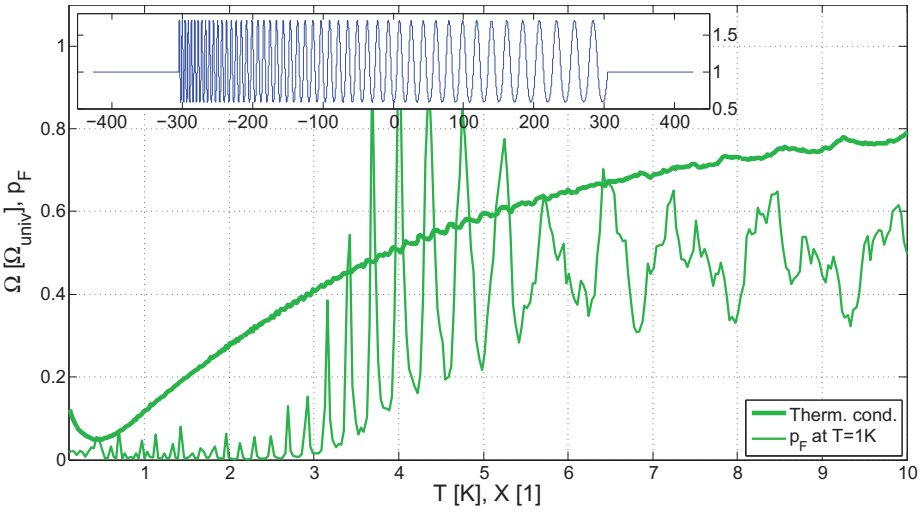


FIGURE 48 Thermal conductance by flexural waves in silicon fiber with diameter $10nm$ and length $4.3\mu m$. Transmission coefficient $p_F(X)$ at $T = 1K$. Inset picture: Boundary curve $B(z)$ for chirped elliptical balanced fiber with 50 periods of sin-type perturbation with first period $L_1 = 20nm$, period ratio $L = 1.04$, chirp ratio $C = 6.8$ and perturbation strength $\alpha = 0.7$.

to obtain a thermal conductance reduction even lower than $1/10$ of corresponding straight cylinder. For perturbation of 50 periods the reduction on interval $[0.1K, 1K]$ is about 90% which satisfies our aim.

## 7.4 Fibers with several perturbed parts

The fact that flexural, torsional and longitudinal modes of same frequency need different perturbation on the fiber to be reflected back leads us to study fibers whose perturbed part consists of two or three different perturbations put in a series. Each of these parts is designed for one phonon type and it is assumed that any of the parts does not interfere much with other phonon types except the one that it is designed for. This might be achievable with computerized form optimization or with just conventional design applying physical arguments.

Let us study with an example what happens if two almost periodical perturbations are put in a series. We choose here only slightly chirped structures with small number of periods in order to maintain good numerical accuracy and low time spend in calculation. We can assume that interference effect of two perturbed parts is independent of the physical model used so we can choose e.g.

longitudinal 1D model. Let perturbation $G_1(R_1)$ contain ten periods of symmetric cos-type perturbation with chirp ratio $C_1 = 3$ and length of the first period $L_{11} = 50nm$. Let perturbation $G_2(R_2)$ contain six periods of similar perturbation with chirp ratio $C_2 = 2$ and first period $L_{21} = 100nm$. Diameter of both fibers is $D = 10nm$. We also parameterize the distance $l$ between perturbations $G_1$ and $G_2$ in order to study how far from each other different perturbations should be placed without much interference. To construct shorter fibers $l$ should be minimized. In Figure 49 we present the transmission probabilities $p_L$ of parts $G_1$ and

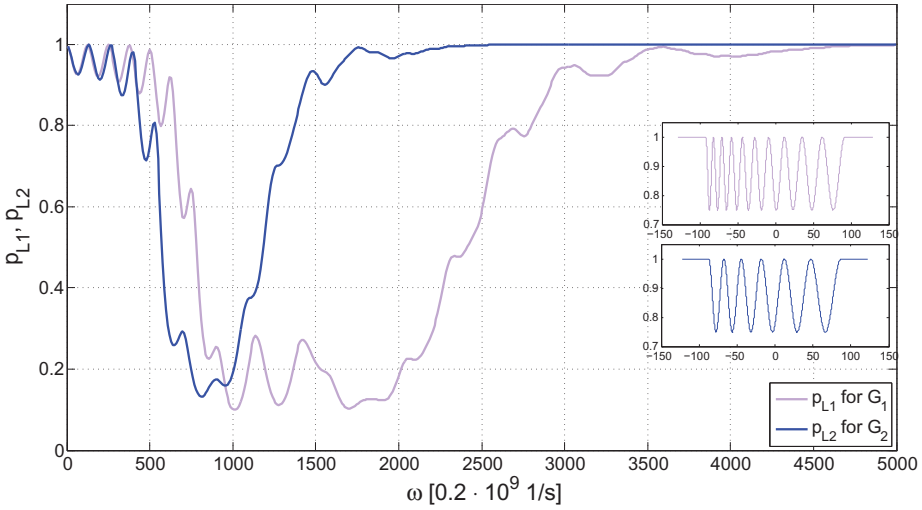


FIGURE 49 Transmission probabilities of longitudinal 1D waves in perturbations $G_1$ and $G_2$. Inset pictures show the form of boundary curve $B_x$. Up: $G_1$, Down: $G_2$.

$G_2$ as a function of $\omega$. Immediate remark is that probability cliffs overlap around $\omega \approx 180 \cdot 10^9\, 1/s$.

In Figure 50 there is also the transmission probability curve for fiber containing both perturbations $G_1$ and $G_2$ with mutual distance $l = 0$. The black curve in Figure 50 is formed by multiplying probability curves $p_{L1}$ and $p_{L2}$. We can immediately see that it serves as an approximation to transmission probability of combined fiber. Blue curve in Figure 50 has spikes which can be explained as resonances in longer perturbed part. We noticed that increasing the distance $l$ results into more spikes on transmission coefficient curve. There was no difference in cliff depth or width. Therefore we conclude that distance should be set to zero when combining almost periodical perturbations.

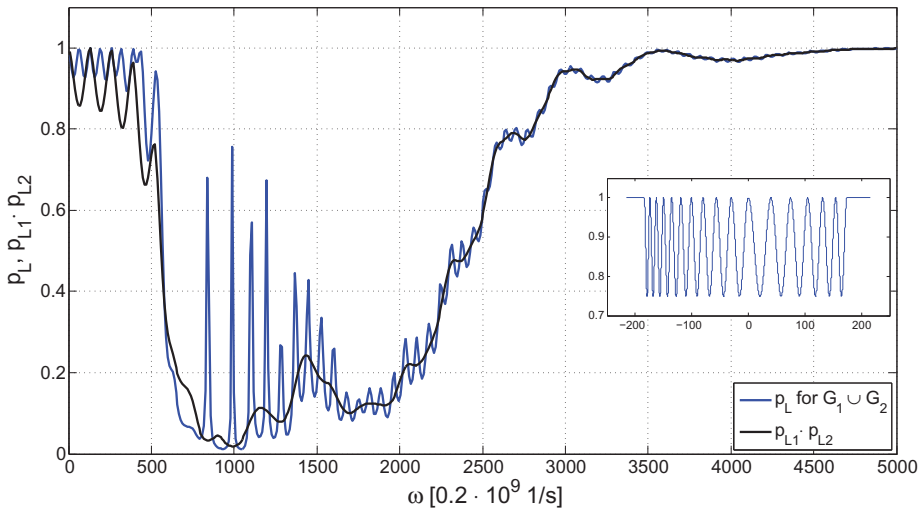


FIGURE 50 Transmission probability of combined perturbations $G_1 \cup G_2$ together with product of $p_{L1}$ and $p_{L2}$ from Figure 49. Inset picture shows to form of combined fiber.

# 8 NUMERICAL IMPLEMENTATION IN MATLAB/COMSOL

In this final chapter we give a description of the program code and numerical method that was used in elastic wave simulations in 1D and 3D nanofibers. Simulation was done completely with MATLAB version R2008b and COMSOL version 3.5. Moreover, COMSOL Multiphysics graphical user interface was often used to produce MATLAB script to serve as a basis for correct syntax and to set up a correct physical problem. As a numerical method to solve the arising equations we used finite element method, abbreviated here by FEM as usual. The mathematical partial differential problems arising from simulation were mounted to COMSOL toolboxes and build-in FEM solvers SPOOLES and UMFPACK were run to obtain numerical solutions. COMSOL Multiphysics was also used for drawing some figures of fibers and periodicity cells in the thesis. Some parts of the coding for MATLAB and working with COMSOL was done with Dr. Alexey Pozharskiy. Simulations were run on Intel(R) Core(TM)2 Duo CPU E8500 @ 3.16$GHz$ system with 4G ram memory. Before explaining the program structure in detail we take a quick glance at FEM.

## 8.1 Finite element method

To solve a partial differential equation with the finite element method, a mesh must be constructed on the geometry. It is a piece-wise partition of the domain. Mesh consists of small units of a simple shape called mesh elements. Mesh elements can be of various forms, linear or curved. Curved mesh elements are used to approximate a curved domain better than linear elements. [38] In our studies we chose curved elements, because the domain is cylindrical and there is curvature involved with the perturbation. Perhaps the most common choice is to use mesh elements of polynomial curvature of order $k$. This means that all the elements are polynomials of degree $k$ and they can be described with $k+1$ different nodes. We have chosen $k = 2$, because a slowly changing cross-sectionally cir-

cular or elliptical domain, as it is in our case, can be thought to be approximated sufficiently well with second order polynomials. It means that for each mesh element parameterized with $t \in [0,1]$ the points $t = 0, 1/2$ and 1 define the shape of the element. It should be remarked that by increasing the mesh thickness results usually to better precision and therefore an optimal mesh should be sought from various curvature and thickness alternatives.

Once the mesh is formed, we can introduce approximations to the dependent variables. We go through here the discussion presented in [38] by concentrating only on one unknown variable, $u$. The general idea in FEM is to approximate $u$ with functions $\phi$ that can be described with a finite number of parameters. These parameters are called degrees of freedom. Functions $\phi$ form so called finite element space or a basis. Usually with a polynomial mesh of degree $k$ Lagrange elements of degree $k$ are used as a basis. Lagrange basis is formed by introducing polynomials $\phi_n$ such a way that on every node $t = n/k$, $n = 0, 1, \ldots, k$,

$$\phi_n(t) = \begin{cases} 1, & \text{if } t = n, \\ 0, & \text{if } t \neq n. \end{cases}$$

Now the dependent variable $u$ can be expressed formally with $u = \sum_n U_n \phi_n$ on each mesh element. Coefficients $U_n$ form a solution vector $U$ when $n$ goes through all the nodes in mesh. In order to solve $U$ one must discretize also all the constrains, boundary conditions, and the equation itself.

Let us focus only on 2D problem on $\Omega$ for simplicity. Assume we have some constrains

$$\begin{aligned} 0 &= R^{(2)} \qquad \text{on } \Omega, \\ 0 &= R^{(1)} \qquad \text{on } \partial\Omega, \\ 0 &= R^{(0)} \qquad \text{on } P, \end{aligned}$$

where $P$ is some set of points. Now for each mesh element in $\partial\Omega$ coded by number $m$, consider the nodes $j = 1, \ldots, k$ denoted by $x^{(1)}_{mj}$. Then we can discretize the constraints on boundary with

$$0 = R^{(1)}\left(x^{(1)}_{mj}\right).$$

Constraints then hold point-wise at the Lagrange points. The constraints on domain $\Omega$ and set of discrete points $P$ are discretized in the similar way. Finally all the point-wise constraints are collected in one equation $0 = M(U)$ with a discretized solution vector $U$.

We now discretize the problem by considering the weak form:

$$\begin{aligned} 0 = &\int_\Omega W^{(2)} + \int_{\partial\Omega} W^{(1)} + \Sigma_P W^{(0)} \\ &- \int_\Omega v \cdot h^{(2)} \mu^{(2)} - \int_{\partial\Omega} v \cdot h^{(1)} \mu^{(1)} - \sum_P v \cdot h^{(0)} \mu^{(0)}, \end{aligned}$$

where $\mu^{(d)}$ are so called Lagrange multipliers and functions $v$ are the test functions. It is enough to require that the weak equation holds when we choose the

test functions as basis functions $v = \phi_n$. By inserting these into the weak formulation we are left with one equation for each $n$. Let

$$\Lambda_{mj}^{(d)} = \mu^{(d)} \left( x_{mj}^{(d)} \right) w_{mj}^{(d)},$$

where $w_{mj}^{(d)}$ are certain weight factors. From the discretized weak equation the term

$$\int_{\partial\Omega} \phi_n \cdot h^{(1)} \mu^{(1)}$$

is approximated as a sum over the mesh elements in $\partial\Omega$. The contribution from each mesh element number $m$ is approximated with the Riemann sum

$$\sum_j \phi_n \left( x_{mj}^{(1)} \right) \cdot h^{(1)} \left( x_{mj}^{(1)} \right) \mu^{(1)} \left( x_{mj}^{(1)} \right) w_{mj}^{(1)} = \sum_j \phi_n \left( x_{mj}^{(1)} \right) \cdot h^{(1)} \left( x_{mj}^{(1)} \right) \Lambda_{mj}^{(1)}$$

where $w_{mj}^{(1)}$ is the length of "appropriate" part of the mesh element $m$. The integral over $\Omega$ and the sum over points $P$ is approximated in a similar fashion.

To sum up, we can write the discretized weak equation as $0 = L(U) - N_F(U)\Lambda$, where $L$ is a vector whose $n^{th}$ component is

$$\int_\Omega W^{(2)} + \int_{\partial\Omega} W^{(1)} + \sum_P W^{(0)}$$

being evaluated with test functions $v = \phi_n$. Vector $\Lambda$ contains all the discretized Lagrange multipliers $\Lambda_{mj}^{(d)}$ and matrix $N_F$ has rows formed by concatenating the vectors $\phi_n(x_{mj}^{(d)})$ and $h^{(d)}(x_{mj}^{(d)})$. For more explicit presentation of FEM see e.g. [36, 37]. We now move on to the implementation of the program.

## 8.2 Program code

To start with, we show a diagram in Figure 51 explaining the structure of the program used in simulations. Each block in the diagram represents one or multiple actions ordered from MATLAB. We will explain the main points here so that the numerical results could be easily reproduced.

The program code consists of a main loop where on every step the parameters are changed according to task. Curved arrow refers to this loop. For example when calculating transmission coefficients frequency $\omega$ in the equation is changed every step. Also the domain can be parameterized: for example the number of periods in the perturbation can be changed every step which results to recalculation of length and rebuilding the domain. Parameters block contains the information about the name of the fiber, radius, length, setup for boundary curve function, period number, period ratio and chirp ratio. There are also numerous parameters about resolution of pictures, minimum and maximum frequencies and physical constants, and finally the order which task is to be calculated by the

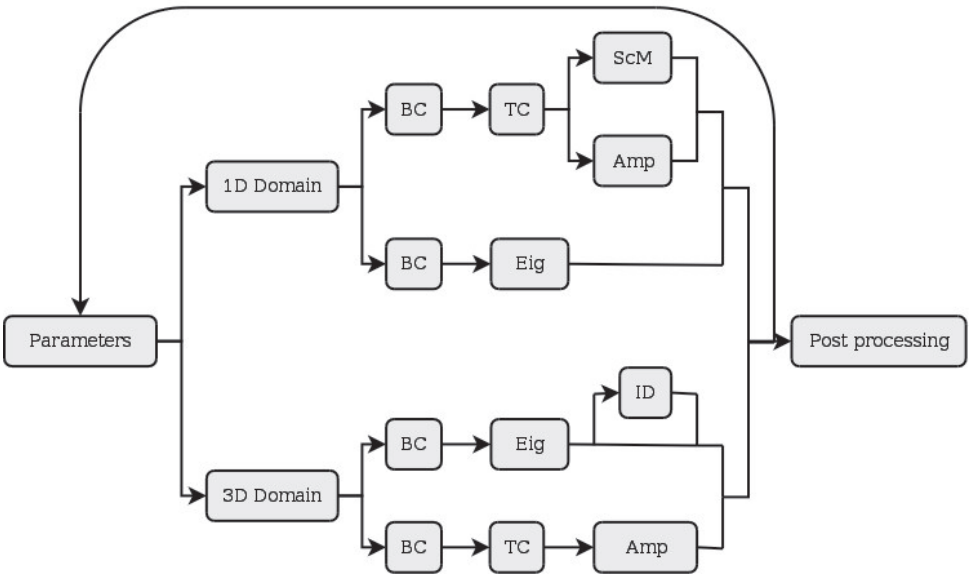


FIGURE 51 Diagram of the program that is used to simulate propagation of elastic waves in 1D and 3D domains.

solver. Solver is then chosen accordingly for 1D or 3D case. Let us now explain the main parts of code and give some details about the solutions we made. A basic understanding of MATLAB syntax is expected from the reader.

## 8.3 One dimensional simulation

One dimensional solver first builds a 1D domain with respect to information of the length and the task. For eigenfrequency problem the domain is set to equal the length of one period with

```
fiber_final=solid1([-(1+10e-6)*first_period/2,...
                    first_period/2]);
```

where there is a small addition ($10^{-6}$ %) at left boundary in order relax the symmetry of the domain. This was found to give more robust functionality for the code. For calculating the transmission coefficients, the domain was built larger containing the perturbation and additional straight parts at the ends of fiber. Also the mesh was constructed so that finally when solving the problem the number of degrees of freedom was between $60000 - 120000$. These values were the largest which could be used on a computer system at hand.

After formation of the domain correct time-independent one dimensional ordinary differential equation for each task is set by defining the coefficient func-

tions in the general second order formula (76)

$$\begin{cases} e_a \frac{\partial^2 u}{\partial t^2} + d_a \frac{\partial u}{\partial t} + \nabla \cdot (-c\nabla u - \alpha u + \gamma) + \beta \cdot \nabla u + au = f & \text{in } G(S), \\ \nu \cdot (c\nabla u + \alpha u - \gamma) + qu = g - h^T \mu & \text{on } \partial G(S), \\ hu = r & \text{on } \partial G(S). \end{cases} \tag{76}$$

For example to solve flexural transmission coefficient the equation was set with

```
equ.f = 0;
equ.da = 0;
equ.c = {{1,0;0,1}};
equ.a = {{0,'1/(BY(x)*BX(x)^3)';...
        '(omega^2)*(4*rho/E)*(BX(x)*BY(x))',0}};
```

while other coefficients are by default set to zero. Here e.g. BX(x) refers to MATLAB .m file containing definition of boundary curve function $B_x(x)$. The solver also sets correct boundary conditions according to task. For transmission coefficients, different boundary conditions were chosen for each phonon type. For example with longitudinal wave simulation with BAM method we use an inline function to apply different values of $\omega$ to boundary conditions. This was done by

```
a = num2str(omega*sqrt(rho/E));
fcns{1}.type='inline';
fcns{1}.name='Long(x)';
fcns{1}.expr=sprintf('exp(%s *i*x)',a);
fcns{1}.complex='true';
```

and function Long(x) was then used in boundary condition

```
bnd.g = {'-2*i*zeta*Long(x)',0};
```

For both BAM and SM the scattering problem for longitudinal and torsional waves was solved with

```
fem.sol=femstatic(fem, ...
                  'complexfun','on', ...
                  'solcomp',{'u'}, ...
                  'outcomp',{'u'}, ...
                  'linsolver','spooles');
```

For flexural waves an additional variable v was used in order to be able to solve fourth order ordinary differential equation, and instead of SPOOLES, a solver called UMFPACK was used to get rid of inaccuracy at low values of $\omega$.

For SM method the inner products (66) were calculated by evaluating the incoming and outgoing fields with function postint which returns the value of solution $u$ at given node. For BAM, the field amplitudes and their derivatives at both boundaries were evaluated with e.g.

```
uleft = postinterp(FieldLeftIn,'u',[CoordLeft]);
uxleft = postinterp(FieldLeftIn,'ux',[CoordLeft]);
```

and after that amplitudes were calculated with equation (58). Finally in transmission coefficients for different frequencies are stored in a vector or matrix which is later plotted and stylized in post processing block.

The construction of eigenfrequency solver for 1D is somewhat simpler. Only the equation must be set differently according to which phonon type one intends to simulate.

## 8.4 Three dimensional simulation

In 3D simulation the domain must be geometrically constructed along the shapes of boundary curves $B_x$ and $B_y$. In order to build the perturbation, a point-wise approximation of boundary curves is taken and stored into vectors scalevectX and scalevectY. Resolution of this approximation is 40 steps per period for infinite fibers and 60 steps per perturbation for finite fibers. The resolution for finite fibers cannot be taken much bigger because of the increase of mesh size. Number 60 was found the best by testing several other resolutions and comparing the strength of numerical fluctuations in transmission coefficient curves.

After taking the linear approximation a 2D base circle or ellipse is drawn by

```
e1 = ellip2(BX(lbound),BY(lbound),...
            'base','center','pos',[0,0]);
```

and it is expanded to 3D with information stored to distvect, scalevectX and scalevectY. Expansion is done with extrude by commanding

```
graph = extrude(e1,'distance',distvect,...
                'scale',[scalevectX;scalevectY]);
```

The resulting perturbation is circular or elliptical tube whose boundary curves at $x$-$z$ and $y$-$z$ plane follow piece-wise linear approximations of boundary curve functions $B_x$ and $B_y$.

Finally if the task is to solve a scattering problem of longitudinal wave in finite fiber to obtain transmission coefficients, an additional straight cylinders are added to both ends of perturbation. The mesh is built with default settings from COMSOL except that for long fibers $z$-direction must be scaled. We have used values $0.4, \ldots, 1$ for Zscale with command

```
fem.mesh=meshinit(fem,'Zscale',0.4);
fem.mesh=meshrefine(fem);
fem.mesh=meshrefine(fem);
```

Usually two or three mesh triangulations are done in 3D case in order to obtain a finer mesh. The number of degrees of freedom is over 60000 for eigenfrequency problems and scattering problems emerging from simulations.

Setting up the correct boundary conditions in 3D problems needs more rigorous scripting than in 1D case. COMSOL solver needs information about the vertices that are located on the edges of boundary element for which boundary

condition is set. In COMSOL faces and vertices are numbered in awkward fashion so that even small changes in the geometry of domain can change the ordering. Therefore at the beginning of a loop cycle, right after the domain is built the face numbers of circular ends are identified. It is done algorithmically by finding the faces which are closest to points $(0, 0, \pm R \mp \epsilon)$, $\epsilon > 0$ small, outside of the 3D domain. Vertices that lay on these faces are identified as well and put in correct cyclic order into string cell variables bnd.ind and submap. This guarantees that no twist will appear in the solution field. Identifying algorithm of faces and vertices was made with help of MATLAB codes by Yannick Fargier, which were obtained from COMSOL Discussion Forum.

For 3D eigenfrequency problem we used COMSOL build-in toolbox Structural Mechanics, Solid Stress-Strain, where the equation (76) is set in weak form. However the boundary conditions can still be given in strong form for COMSOL solvers. For solving the eigenfrequency problem we used options complexfun, conjugate and symmetric set to "on" where the first orders COMSOL to handle complex valued functions correctly. Last two options set the coefficient matrix of the problem Hermitian i.e. conjugate and symmetric so that certain unwanted solutions are neglected. These do not represent elastic displacement modes. SPOOLES was used to numerically solve the 3D problem in this case. Eigenfrequencies are then stored into matrix and if necessary the identifying algorithm is run for eigenmodes.

The identifying algorithm tests the eigenmodes according to rules explained in Chapter 3. For every solved eigenmode a number of points along $z$-axis are evaluated in the solution field with function postinterp. Then $x$-$y$ and $z$-norms are calculated for comparing their values to control values which are set in advance. Finally, according to the results obtained, every mode is named after its characteristics and the information is stored in string variable to be used to construct separate eigenfrequency curves.

To solve the scattering problem for 3D longitudinal waves we used the same toolbox than for 3D eigenfrequency problem. Only the weak term in the equation was revised slightly by adding term $\rho\omega^2(u\tilde{u} + v\tilde{v} + w\tilde{w})$ to it. Tildes over directional displacement fields $u$, $v$ and $w$ refer to test functions. Weak term in MATLAB then appears as

```
equ.weak='-ex_sld_test*sx_sld-ey_sld_test*sy_sld -...
          ez_sld_test*sz_sld -2*exy_sld_test*sxy_sld -...
          2*eyz_sld_test*syz_sld -2*exz_sld_test*sxz_sld +...
          rho_sld*omega^2*(u*test(u)+v*test(v)+w*test(w))';
```

where sx_sld $= \sigma_{xx}$, ex_sld_test $= \widetilde{e_{xx}}$, etc. are stresses and test functions with the notation borrowed from definition (20). Boundary conditions at the ends of domain are set in similar fashion to 1D case except that inline function, called ZLong(x,y,z), is three dimensional. They are set with

```
bnd.g = {0,{0;0;'-2*i*zeta*Zlong(x,y,z)'},0};
bnd.q = {0,{0;0;'-i*zeta'},{0;0;'-i*zeta'}};
```

where zeta is defined with zeta $= E\omega\sqrt{\rho/E}$. Additional coefficient $E$ is put in

front to compensate matrix $c$ in the formula for strong boundary condition in equation (76). Matrix $c$ cannot be set to e.g. identity matrix because weak formulation of the problem forces it to be recalculated.

## 8.5 Post processing

After calculating the necessary amount of problems for the task at hand the results are plotted and stylized. For presenting displacement fields graphically in Chapter 2 and 3 we used COMSOL function postplot. In order to set correct parameters for color scale, camera angle and distance we applied COMSOL Multiphysics to build MATLAB script for that. By sharing the same orientation and distance displacement fields can be compared more easily. Also the inset pictures of domains used in many graphs showing frequency spectra or transmission coefficient were produced by COMSOL script and with geomplot function. Three dimensional objects were always drawn with perspective and, if applicable, rendered.

Color coding for flexural, torsional and longitudinal waves was automatically kept standard through out the text. Flexural frequency spectrum, transmission coefficients and thermal conductance used medium green color with RGB code $(0, 173, 0)$. Torsional waves were coded with red $(255, 0, 0)$ where longitudinal were blue $(0, 0, 255)$. Also the main figures were named automatically so that the header would express the name of fiber, length, diameter, value of parameter $\alpha$ or other important quantities.

Eigenfrequency solver stores solutions in a matrix. Each row vector in the matrix corresponds to solution with one set of preliminary parameters. Elements of the row vector are the eigenfrequencies expressed in complex numbers $z$, where imaginary component gives the eigenfrequency and real number can be understood as an quantity for error. If $\operatorname{Re} z \ll \operatorname{Im} z$ then the real part is neglected from the solution. Frequency spectrum is plotted with function plot hence the resulting graph is a set of piece-wise linear curves that go through elements in each row vector. The resolution of frequency spectra, i.e. the length of row vectors, was usually 120. Transmission coefficients are also stored in vectors and plotted with the same function plot. To form 3D surfaces of transmission coefficients we again used a matrix as a storage medium and finally plotted the solution with function surf. Shading model for 3D surfaces used interpolation method called Gouraud shading.

Finally the thermal conductance curves were calculated on basis of transmission coefficient vectors. We used a simple loop to calculate the contribution of each element in vector to the integral of thermal conductance. This had to be done because MATLAB cannot directly integrate functions defined by their values stored in vectors. Also the change of variable $X = \hbar\omega/k_B T$ with different value of $T$ for transmission coefficient curves was done in a loop where on each step the vector elements $p_i$, $p_{i+1}$ surrounding $\omega$ were searched. Then a value for

$X$ was calculated from the linear curve connecting the scaled values of $p_i$, $p_{i+1}$. Consequence of this algorithm is that for higher $T$ the resolution of scaled transmission coefficient curve is reduced because it is scaled towards zero. However the curves are smooth enough to express a general behavior of thermal conductance for perturbed nanofibers of this design.

# 9 CONCLUSIONS AND FURTHER STUDY

In the thesis we have given an account on the investigation of acoustic phonons (elastic waves) of sufficiently low frequencies in cylindrical corrugated dielectric nanofibers. First we calculate the frequency spectra of phonon propagation for various periodically corrugated cylinders. We found out that periodically corrugating the boundary of the fiber results into spectral gaps in the frequency spectrum. The phonons whose frequencies lay in these gaps are prevented from propagating. We also compared the exact 3D spectrum to 1D spectra obtained from various 1D models. These well known 1D models [18] gave very good estimates at the low-frequency region of exact 3D spectrum. We concluded that 1D models are suitable for simulating the lowest phonon modes.

We also considered a phonon propagation in finitely corrugated fibers. This was first done by numerically calculating the amplitudes of scattered displacement field (BAM) for longitudinal waves at the beginning and the end of the 3D perturbed fiber. Afterwards, similar calculation was done with 1D model for longitudinal waves and we concluded that 1D modelling should be sufficiently reliable for all the massless modes. In addition, a different method (SM) to calculate the scattering matrix [13] was used in 1D to compute the transmission probabilities, which gave the same results. We concluded that SM and BAM lead to equal results and that BAM should be used because it is over four times faster. For a sufficiently long finite fiber with cos-type perturbed part we managed to find estimates for a number of periods, which reduces transmission probability of various phonon types less than 0.1 in the first spectral gap. We also concluded that the forbidden band for phonons could be increased by monotonously increasing perturbation periods and combining various perturbations in a series.

We make use of the results on phonon propagation to calculate low-temperature thermal conductance of corrugated nanofibers. We also designed a finitely long nanofiber with different corrugated parts that has a thermal conductance of only about 10% of the similar unperturbed cylinder. Such a fiber can be utilized e.g. as a structural support for low-temperature infrared detectors. Moreover, during the studies a program code was written for MATLAB/COMSOL that can be used to compute the transmission probabilities of phonons or the thermal con-

ductance of a nanofiber with given geometry parameters.

The research done gives a reasonable basis for further studies. The program code that was used in simulations can be harnessed to similar studies concerning thermal conductance in more complicated structures, for example, fibers with complex geometry or ”superlattices”. The latter can be constructed by periodical variation of material constants. It was reported [39] that e.g. periodic doping of silicon ($^{28}$Si) by its isotope $^{42}$Si can reduce thermal conductance as much as four times at $300K$. Similar results can be expected at low-temperature limit. Material parameters of nanofibers can be changed also by adding clumps of other material, which affect the rigidity or density of the fiber. One can also study the thermal conductance of simpler nanosize structures such as in [40].

Another direction involving numerical studies would be to apply the program code into shape optimization procedure to find an optimal form for the periodicity cell. [41, 42] The goal can be for example to obtain better reflective properties with a shorter corrugation or an ability to reflect only certain types of phonons.

## REFERENCES


[1] Baskin L.M., Neittaanmäki P., Plamenevskii B.A., Pozharskii A.A., A Method for Reducing the Low-Temperature Thermal Conductivity of Nanofibers, Doklady Physics, vol.53, no.1, 34-38, (2008).

[2] Baskin L.M., Neittaanmäki P., Plamenevskii B.A., Pozharskii A.A., Control of the Low-Temperature Thermal Conductivity of Deformed Nanofibers, Reports of the Depart. Math. Inf. Tech., Series B. Scientific Computing, No.B 8, (2006).

[3] Ashcroft N.W., Mermin N.D., Solid State Physics, Holt, Rinehart and Winston, (1976).

[4] Ziman J.M., Electrons and Phonons, Oxford University Press, (2003).

[5] Ibach H., Lüth H., Solid-State Physics, Springer, (2003).

[6] Landauer R., IBM J. Res. Dev., 1:22385A, 91, (1981).

[7] Rego L.G.C., Kirczenow G., Quantized thermal conductance of dielectric quantum wires, Phys. Rev. Let. 81(1):232-235, (1998).

[8] Santamore D.H., Cross M.C., Effect of phonon scattering by surface roughness on the universal thermal conductance, Phys. Rev. Lett., 87:115502, (2001).

[9] Santamore D.H., Cross M.C., Effect of surface roughness on the universal thermal conductance, Phys. Rev. B, 63:184306, (2001).

[10] Poladian L., Graphical and WKB analysis of nonuniform Bragg gratings, Phys. Rev. E, 48:4758, (1993).

[11] Nazarov S.A., Plamenevsky B.A., Elliptic Problems in Domains with Piecewise Smooth Boundaries, Walter de Gruyter, Berlin, (1994).

[12] Grikurov V., Heikkola E., Neittaanmäki P., Plamenevskii B.A., On computation of scattering matrices and on surface waves in diffraction gratings, Numerische Mathematik, 94 (2), 269-288, (2003).

[13] Kalvine V.O., Neittaanmäki P., Plamenevskii B.A., Method for computing scattering matrices for general dissipative and selfadjoint elliptic problems in domains with cylindrical ends, J. Math. Sci., 122, no.3, 3212-3245, (2004).

[14] Timoshenko S.P., Goodier J.N., Theory of Elasticity, McGraw-Hill, (1970).

[15] Timoshenko S.P., Woinowsky-Krieger S., Theory of Plates and Shells, McGraw-Hill, (1964).

[16] Timoshenko S.P., Gere J., Theory of Elastic Stability, 2nd ed., McGraw-Hill, (1961).

[17] Landau L.D., Lifshitz E.M., Theory of Elasticity, Third ed., Pergamon Press, (1986).

[18] Graff K.F., Wave Motion in Elastic Solids, Dover, (1991).

[19] Ylinen A., Kimmo- ja lujuusoppi, WSOY, (1965).

[20] Tiihonen T., Matemaattinen mallintaminen, lecture notes 16, Univ. of Jyväskylä, (1991).

[21] Clough R.W., Penzien J., Dynamics of structures, McGraw-Hill, (1975).

[22] Murray N.W., Introduction to the theory of thin-walled structures, Oxford University Press, (1986).

[23] Pennala E., Koneiden ja rakenteiden värähtelyt, Otakustantamo, (1998).

[24] Weber L., Gmelin E., Transport Properties of Silicon, Appl. Phys. A, 53, 136-140, (1991).

[25] Li D., Wu Y., Kim P., Shi L., Yang P., Majumdar A., Thermal conductivity of individual silicon nanowires, Appl. Phys. Lett. 64, no.14, (2003).

[26] Chen K.-Q., Li W.-X., Duan W., Shuai Z., Gu B.-L., Effect of defects on the thermal conductivity in a nanowire, Phys. Rev. B, 72, (2005).

[27] Pozharskii A., On the Electron and Phonon Transport in Locally Periodical Waveguides, Jyväskylä Studies in Computing, 101, (2008).

[28] Cleland A.N., Schmidt R.K., Yung C.S., Thermal conductance of nanostructured phononic crystals, Phys. Rev. B, 64, (2001).

[29] Li W.-X., Chen K.-Q., Duan W., Wu J., Gu B.-L., Acoustic phonon mode splitting behavior of an asummetric y-branch three terminal junction, Appl. Phys. Lett., 85, no.5, (2004).

[30] Li W.-X., Chen K.-Q., Duan W., Wu J., Gu B.-L., Acoustic phonon transport through a T-shaped quantum waveguide, J. Phys: Condens. Matter, 16, (2004).

[31] Nie L.-Y., Wang L., Chen K.-Q., Zou B.S., Zhao L.H., Thermal conductance in quantum wire with two obstacles, Physica E, 39, (2007).

[32] Kambili A., Fagas G., Fal'ko V.I., Lambert C.J., Phonon-mediated thermal conductance of mesoscopic wires with rough edges, Phys. Rev. B, 60, no.23, (1999).

[33] Martin P.N., Aksamija Z., Pop E., Ravaioli U., Reduced Thermal Conductivity in Nanoengineered Rough Ge and GaAs Nanowires, Nano Lett., 10(4), (2010).

[34] Mingo N., Calculation of Si nanowire thermal conductivity using complete phonon dispersion relations, Phys Rev. B, 68, (2003).

[35] Mingo N., Yang L., Li D., Majumdar A., Predicting the Thermal Conductivity of Si and Ge Nanowires, Nano Lett., 3, no.12, (2003).

[36] Hughes T.J.R., The Finite Element Method, Dover, (2000).

[37] Neittaanmäki P., Krizek M., Mathematical and Numerical Modelling in Electrical Engineering, Kluwer Academic Publishers, (1996).

[38] COMSOL: Multiphysics User's Guide, COMSOL 3.5, (2008).

[39] Yang N., Zhang G., Li B., Ultralow Thermal Conductivity of Isotope-Doped Silicon Nanowires, Nano Lett. 8, no.1, (2008).

[40] Tighe T.S., Worlock J.M., Roukes M.L., Direct thermal conductance measurements on suspended monocrystalline nanostructures, Appl. Phys. Lett. 70(20), (1997).

[41] Haslinger J., Neittaanmäki P., Finite Element Approximation for Optimal Shape, Material and Topology Design, 2nd ed. Chichester: J. Wiley and Sons, (1996).

[42] Neittaanmäki P., Sprekels J., Tiba D., Optimization of Elliptic Systems: Theory and Applications, Springer, (2006).

## YHTEENVETO (FINNISH SUMMARY)

Tässä työssä, nimeltään ”Poimutettujen nanokuitujen lämmönjohtavuuden numeerinen simulointi matalissa lämpötiloissa” on simuloitu numeerisesti reunaltaan poimutettujen elastisten nanokuitujen lämmönjohtavuutta matalissa lämpötiloissa. Kuidun pinnalle muotoiltiin erityinen hitaasti muuttuva sylinterimäinen tai elliptinen poimutus, jotta lämpöenergiaa kuljettavat elastiset aallot (fononit) heijastuisivat takaisin ja kuidun lämmönjohtavuutta voitaisiin näin alentaa. Lämpötila-alueella $T = 0.1 - 10K$ lämpöenergiaa kuljettavat pääosin poikittais- ja pitkittäissuuntaiset, sekä rotaationaaliset aallot, joita simuloitiin 1D- ja 3D-mallein. Äärellisten elementtien menetelmää (FEM) käytettiin ratkaistaessa jaksollisten nanokuitujen taajuusspektri, sekä lyhyiden lokaalisti jaksollisten kuitujen sirontamatriisi. Landauerin teoriaa käytettiin lopuksi ratkaistaessa lämmönjohtavuutta. Numeeriset laskelmat tehtiin käyttäen kuidun materiaalina piitä (Si). Tutkimuksessa havaittiin, että 3D-taajuusspektriä voidaan approksimoida 1D-aaltojen spektrillä, joka saadaan tietyistä yksinkertaisista differentiaaliyhtälöistä. Simuloimalla lukuisia erilaisia kuidun muotoja esitettiin arvoja parametreille, joilla 1D-mallinnus antaa luotettavia tuloksia. Tutkimuksessa voitiin todeta, että yksiulotteista mallia voidaan luotettavasti käyttää matalaenergisten aaltojen läpäisytodennäköisyyksien laskemiseen. Lopuksi piinanokuidulle suunniteltiin erityinen poimutettu sylinterimäinen muoto siten, että kuidun kokonaislämmönjohtavuus saatiin laskemaan 90% lämpötila-alueella $T = 0.1 - 1K$.

# JYVÄSKYLÄ STUDIES IN COMPUTING

1 Ropponen, Janne, Software risk management - foundations, principles and empirical findings. 273 p. Yhteenveto 1 p. 1999.
2 Kuzmin, Dmitri, Numerical simulation of reactive bubbly flows. 110 p. Yhteenveto 1 p. 1999.
3 Karsten, Helena, Weaving tapestry: collaborative information technology and organisational change. 266 p. Yhteenveto 3 p. 2000.
4 Koskinen, Jussi, Automated transient hypertext support for software maintenance. 98 p. (250 p.) Yhteenveto 1 p. 2000.
5 Ristaniemi, Tapani, Synchronization and blind signal processing in CDMA systems. - Synkronointi ja sokea signaalinkäsittely CDMA järjestelmässä. 112 p. Yhteenveto 1 p. 2000.
6 Laitinen, Mika, Mathematical modelling of conductive-radiative heat transfer. 20 p. (108 p.) Yhteenveto 1 p. 2000.
7 Koskinen, Minna, Process metamodelling. Conceptual foundations and application. 213 p. Yhteenveto 1 p. 2000.
8 Smolianski, Anton, Numerical modeling of two-fluid interfacial flows. 109 p. Yhteenveto 1 p. 2001.
9 Nahar, Nazmun, Information technology supported technology transfer process. A multi-site case study of high-tech enterprises. 377 p. Yhteenveto 3 p. 2001.
10 Fomin, Vladislav V., The process of standard making. The case of cellular mobile telephony. - Standardin kehittämisen prosessi. Tapaustutkimus solukkoverkkoon perustuvasta matkapuhelintekniikasta. 107 p. (208 p.) Yhteenveto 1 p. 2001.
11 Päivärinta, Tero, A genre-based approach to developing electronic document management in the organization. 190 p. Yhteenveto 1 p. 2001.
12 Häkkinen, Erkki, Design, implementation and evaluation of neural data analysis environment. 229 p. Yhteenveto 1 p. 2001.
13 Hirvonen, Kullervo, Towards better employment using adaptive control of labour costs of an enterprise. 118 p. Yhteenveto 4 p. 2001.
14 Majava, Kirsi, Optimization-based techniques for image restoration. 27 p. (142 p.) Yhteenveto 1 p. 2001.
15 Saarinen, Kari, Near infra-red measurement based control system for thermo-mechanical refiners. 84 p. (186 p.) Yhteenveto 1 p. 2001.
16 Forsell, Marko, Improving component reuse in software development. 169 p. Yhteenveto 1 p. 2002.
17 Virtanen, Pauli, Neuro-fuzzy expert systems in financial and control engineering. 245 p. Yhteenveto 1 p. 2002.
18 Kovalainen, Mikko, Computer mediated organizational memory for process control. Moving CSCW research from an idea to a product. 57 p. (146 p.) Yhteenveto 4 p. 2002.
19 Hämäläinen, Timo, Broadband network quality of service and pricing. 140 p. Yhteenveto 1 p. 2002.
20 Martikainen, Janne, Efficient solvers for discretized elliptic vector-valued problems. 25 p. (109 p.) Yhteenveto 1 p. 2002.
21 Mursu, Anja, Information systems development in developing countries. Risk management and sustainability analysis in Nigerian software companies. 296 p. Yhteenveto 3 p. 2002.
22 Seleznyov, Alexandr, An anomaly intrusion detection system based on intelligent user recognition. 186 p. Yhteenveto 3 p. 2002.
23 Lensu, Anssi, Computationally intelligent methods for qualitative data analysis. 57 p. (180 p.) Yhteenveto 1 p. 2002.
24 Ryabov, Vladimir, Handling imperfect temporal relations. 75 p. (145 p.) Yhteenveto 2 p. 2002.
25 Tsymbal, Alexey, Dynamic integration of data mining methods in knowledge discovery systems. 69 p. (170 p.) Yhteenveto 2 p. 2002.
26 Akimov, Vladimir, Domain decomposition methods for the problems with boundary layers. 30 p. (84 p.). Yhteenveto 1 p. 2002.
27 Seyukova-Rivkind, Ludmila, Mathematical and numerical analysis of boundary value problems for fluid flow. 30 p. (126 p.) Yhteenveto 1 p. 2002.
28 Hämäläinen, Seppo, WCDMA Radio network performance. 235 p. Yhteenveto 2 p. 2003.
29 Pekkola, Samuli, Multiple media in group work. Emphasising individual users in distributed and real-time CSCW systems. 210 p. Yhteenveto 2 p. 2003.
30 Markkula, Jouni, Geographic personal data, its privacy protection and prospects in a location-based service environment. 109 p. Yhteenveto 2 p. 2003.
31 Honkaranta, Anne, From genres to content analysis. Experiences from four case organizations. 90 p. (154 p.) Yhteenveto 1 p. 2003.
32 Raitamäki, Jouni, An approach to linguistic pattern recognition using fuzzy systems. 169 p. Yhteenveto 1 p. 2003.
33 Saalasti, Sami, Neural networks for heart rate time series analysis. 192 p. Yhteenveto 5 p. 2003.
34 Niemelä, Marketta, Visual search in graphical interfaces: a user psychological approach. 61 p. (148 p.) Yhteenveto 1 p. 2003.
35 You, Yu, Situation Awareness on the world wide web. 171 p. Yhteenveto 2 p. 2004.
36 Taatila, Vesa, The concept of organizational competence – A foundational analysis. - Perusteanalyysi organisaation kompetenssin käsitteestä. 111 p. Yhteenveto 2 p. 2004.

37 LYYTIKÄINEN, VIRPI, Contextual and structural metadata in enterprise document management. - Konteksti- ja rakennemetatieto organisaation dokumenttien hallinnassa. 73 p. (143 p.) Yhteenveto 1 p. 2004.
38 KAARIO, KIMMO, Resource allocation and load balancing mechanisms for providing quality of service in the Internet. 171 p. Yhteenveto 1 p. 2004.
39 ZHANG, ZHEYING, Model component reuse. Conceptual foundations and application in the metamodeling-based systems analysis and design environment. 76 p. (214 p.) Yhteenveto 1 p. 2004.
40 HAARALA, MARJO, Large-scale nonsmooth optimization variable metric bundle method with limited memory. 107 p. Yhteenveto 1 p. 2004.
41 KALVINE, VIKTOR, Scattering and point spectra for elliptic systems in domains with cylindrical ends. 82 p. 2004.
42 DEMENTIEVA, MARIA, Regularization in multistage cooperative games. 78 p. 2004.
43 MAARANEN, HEIKKI, On heuristic hybrid methods and structured point sets in global continuous optimization. 42 p. (168 p.) Yhteenveto 1 p. 2004.
44 FROLOV, MAXIM, Reliable control over approximation errors by functional type a posteriori estimates. 39 p. (112 p.) 2004.
45 ZHANG, JIAN, Qos- and revenue-aware resource allocation mechanisms in multiclass IP networks. 85 p. (224 p.) 2004.
46 KUJALA, JANNE, On computation in statistical models with a psychophysical application. 40 p. (104 p.) 2004.,
47 SOLBAKOV, VIATCHESLAV, Application of mathematical modeling for water environment problems. 66 p. (118 p.) 2004.
48 HIRVONEN, ARI P., Enterprise architecture planning in practice. The Perspectives of information and communication technology service provider and end-user. 44 p. (135 p.) Yhteenveto 2 p. 2005.
49 VARTIAINEN, TERO, Moral conflicts in a project course in information systems education. 320 p. Yhteenveto 1p. 2005.
50 HUOTARI, JOUNI, Integrating graphical information system models with visualization techniques. - Graafisten tietojärjestelmäkuvausten integrointi visualisointitekniikoilla. 56 p. (157 p.) Yhteenveto 1p. 2005.
51 WALLENIUS, EERO R., Control and management of multi-access wireless networks. 91 p. (192 p.) Yhteenveto 3 p. 2005.
52 LEPPÄNEN, MAURI, An ontological framework and a methodical skeleton for method engineering – A contextual approach. 702 p. Yhteenveto 2 p. 2005.
53 MATYUKEVICH, SERGEY, The nonstationary Maxwell system in domains with edges and conical points. 131 p. Yhteenveto 1 p. 2005.
54 SAYENKO, ALEXANDER, Adaptive scheduling for the QoS supported networks. 120 p. (217 p.) 2005.
55 KURJENNIEMI, JANNE, A study of TD-CDMA and WCDMA radio network enhancements. 144 p. (230 p.) Yhteenveto 1 p. 2005.
56 PECHENIZKIY, MYKOLA, Feature extraction for supervised learning in knowledge discovery systems. 86 p. (174 p.) Yhteenveto 2 p. 2005.
57 IKONEN, SAMULI, Efficient numerical methods for pricing American options. 43 p. (155 p.) Yhteenveto 1 p. 2005.
58 KÄRKKÄINEN, KARI, Shape sensitivity analysis for numerical solution of free boundary problems. 83 p. (119 p.) Yhteenveto 1 p. 2005.
59 HELFENSTEIN, SACHA, Transfer. Review, reconstruction, and resolution. 114 p. (206 p.) Yhteenveto 2 p. 2005.
60 NEVALA, KALEVI, Content-based design engineering thinking. In the search for approach. 64 p. (126 p.) Yhteenveto 1 p. 2005.
61 KATASONOV, ARTEM, Dependability aspects in the development and provision of location-based services. 157 p. Yhteenveto 1 p. 2006.
62 SARKKINEN, JARMO, Design as discourse: Representation, representational practice, and social practice. 86 p. (189 p.) Yhteenveto 1 p. 2006.
63 ÄYRÄMÖ, SAMI, Knowledge mining using robust clustering. 296 p. Yhteenveto 1 p. 2006.
64 IFINEDO, PRINCELY EMILI, Enterprise resource planning systems success assessment: An integrative framework. 133 p. (366 p.) Yhteenveto 3 p. 2006.
65 VIINIKAINEN, ARI, Quality of service and pricingin future multiple service class networks. 61 p. (196 p.) Yhteenveto 1 p. 2006.
66 WU, RUI, Methods for space-time parameter estimation in DS-CDMA arrays. 73 p. (121 p.) 2006.
67 PARKKOLA, HANNA, Designing ICT for mothers. User psychological approach. – Tieto- ja viestintätekniikoiden suunnittelu äideille. Käyttäjäpsykologinen näkökulma. 77 p. (173 p.) Yhteenveto 3 p. 2006.
68 HAKANEN, JUSSI, On potential of interactive multiobjective optimization in chemical process design. 75 p. (160 p.) Yhteenveto 2 p. 2006.
69 PUTTONEN, JANI, Mobility management in wireless networks. 112 p. (215 p.) Yhteenveto 1 p. 2006.
70 LUOSTARINEN, KARI, Resource , management methods for QoS supported networks. 60 p. (131 p.) 2006.
71 TURCHYN, PAVLO, Adaptive meshes in computer graphics and model-based simulation. 27 p. (79 p.) Yhteenveto 1 p.
72 ZHOVTOBRYUKH, DMYTRO, Context-aware web service composition. 290 p. Yhteenveto 2 p. 2006.

73 KOHVAKKO, NATALIYA, Context modeling and utilization in heterogeneous networks. 154 p. Yhteenveto 1 p. 2006.
74 MAZHELIS, OLEKSIY, Masquerader detection in mobile context based on behaviour and environment monitoring. 74 p. (179 p). Yhteenveto 1 p. 2007.
75 SILTANEN, JARMO, Quality of service and dynamic scheduling for traffic engineering in next generation networks. 88 p. (155 p.) 2007.
76 KUUVA, SARI, Content-based approach to experiencing visual art. - Sisältöperustainen lähestymistapa visuaalisen taiteen kokemiseen. 203 p. Yhteenveto 3 p. 2007.
77 RUOHONEN, TONI, Improving the operation of an emergency department by using a simulation model. 164 p. 2007.
78 NAUMENKO, ANTON, Semantics-based access control in business networks. 72 p. (215 p.) Yhteenveto 1 p. 2007.
79 WAHLSTEDT, ARI, Stakeholders' conceptions of learning in learning management systems development. - Osallistujien käsitykset oppimisesta oppimisympäristöjen kehittämisessä. 83 p. (130 p.) Yhteenveto 1 p. 2007.
80 ALANEN, OLLI, Quality of service for triple play services in heterogeneous networks. 88 p. (180 p.) Yhteenveto 1 p. 2007.
81 NERI, FERRANTE, Fitness diversity adaptation in memetic algorithms. 80 p. (185 p.) Yhteenveto 1 p. 2007.
82 KURHINEN, JANI, Information delivery in mobile peer-to-peer networks. 46 p. (106 p.) Yhteenveto 1 p. 2007.
83 KILPELÄINEN, TURO, Genre and ontology based business information architecture framework (GOBIAF). 74 p. (153 p.) Yhteenveto 1 p. 2007.
84 YEVSEYEVA, IRYNA, Solving classification problems with multicriteria decision aiding approaches. 182 p. Yhteenveto 1 p. 2007.
85 KANNISTO, ISTO, Optimized pricing, QoS and segmentation of managed ICT services. 45 p. (111 p.) Yhteenveto 1 p. 2007.
86 GORSHKOVA, ELENA, A posteriori error estimates and adaptive methods for incompressible viscous flow problems. 72 p. (129 p.) Yhteenveto 1 p. 2007.
87 LEGRAND, STEVE, Use of background real-world knowledge in ontologies for word sense disambiguation in the semantic web. 73 p. (144 p.) Yhteenveto 1 p. 2008.
88 HÄMÄLÄINEN, NIINA, Evaluation and measurement in enterprise and software architecture management. - Arviointi ja mittaaminen kokonais- ja ohjelmistoarkkitehtuurien hallinnassa. 91 p. (175 p.) Yhteenveto 1 p. 2008.
89 OJALA, ARTO, Internationalization of software firms: Finnish small and medium-sized software firms in Japan. 57 p. (180 p.) Yhteenveto 2 p. 2008.
90 LAITILA, ERKKI, Symbolic Analysis and Atomistic Model as a Basis for a Program Comprehension Methodology. 321 p. Yhteenveto 3 p. 2008.
91 NIHTILÄ, TIMO, Performance of Advanced Transmission and Reception Algorithms for High Speed Downlink Packet Access. 93 p. (186 p.) Yhteenveto 1 p. 2008.
92 SETÄMAA-KÄRKKÄINEN, ANNE, Network connection selection-solving a new multiobjective optimization problem. 52 p. (111p.) Yhteenveto 1 p. 2008.
93 PULKKINEN, MIRJA, Enterprise architecture as a collaboration tool. Discursive process for enterprise architecture management, planning and development. 130 p. (215 p.) Yhteenveto 2 p. 2008.
94 PAVLOVA, YULIA, Multistage coalition formation game of a self-enforcing international environmental agreement. 127 p. Yhteenveto 1 p. 2008.
95 NOUSIAINEN, TUULA, Children's involvement in the design of game-based learning environments. 297 p. Yhteenveto 2 p. 2008.
96 KUZNETSOV, NIKOLAY V., Stability and oscillations of dynamical systems. Theory and applications. 116 p. Yhteenveto 1 p. 2008.
97 KHRIYENKO, OLEKSIY, Adaptive semantic Web based environment for web resources. 193 p. Yhteenveto 1 p. 2008.
98 TIRRONEN, VILLE, Global optimization using memetic differential evolution with applications to low level machine vision. 98 p. (248 p.) Yhteenveto 1 p. 2008.
99 VALKONEN, TUOMO, Diff-convex combinations of Euclidean distances: A search for optima. 148 p. Yhteenveto 1 p. 2008.
100 SARAFANOV, OLEG, Asymptotic theory of resonant tunneling in quantum waveguides of variable cross-section. 69 p. Yhteenveto 1 p. 2008.
101 POZHARSKIY, ALEXEY, On the electron and phonon transport in locally periodical waveguides. 81 p. Yhteenveto 1 p. 2008.
102 AITTOKOSKI, TIMO, On challenges of simulation-based globaland multiobjective optimization. 80 p. (204 p.) Yhteenveto 1 p. 2009.
103 YALAHO, ANICET, Managing offshore outsourcing of software development using the ICT-supported unified process model: A cross-case analysis. 91 p. (307 p.) Yhteenveto 4 p. 2009.
104 KOLLANUS, SAMI, Tarkastuskäytänteiden kehittäminen ohjelmistoja tuottavissa organisaatioissa. - Improvement of inspection practices in software organizations. 179 p. Summary 4 p. 2009.
105 LEIKAS, JAANA, Life-Based Design. 'Form of life' as a foundation for ICT design for older adults. - Elämälähtöinen suunnittelu. Elämänmuoto ikääntyville tarkoitettujen ICT tuotteiden ja palvelujen suunnittelun lähtökohtana. 218 p. (318 p.) Yhteenveto 4 p. 2009.

106 VASILYEVA, EKATERINA, Tailoring of feedback in web-based learning systems: Certitude-based assessment with online multiple choice questions. 124 p. (184 p.) Yhteenveto 2 p. 2009.

107 KUDRYASHOVA, ELENAV., Cycles in continuous and discrete dynamical systems. Computations, computer assisted proofs, and computer experiments. 79 p. (152 p.) Yhteenveto 1 p. 2009.

108 BLACKLEDGE, JONATHAN, Electromagnetic scattering and inverse scattering solutions for the analysis and processing of digital signals and images. 297 p. Yhteenveto 1 p. 2009.

109 IVANNIKOV, ANDRIY, Extraction of event-related potentials from electroencephalography data. - Herätepotentiaalien laskennallinen eristäminen EEG-havaintoaineistosta. 108 p. (150 p.) Yhteenveto 1 p. 2009.

110 KALYAKIN, IGOR, Extraction of mismatch negativity from electroencephalography data. - Poikkeavuusnegatiivisuuden erottaminen EEG-signaalista. 47 p. (156 p.) Yhteenveto 1 p. 2010.

111 HEIKKILÄ, MARIKKA, Coordination of complex operations over organisational boundaries. 265 p. Yhteenveto 3 p. 2010.

112 FEKETE, GÁBOR, Network interface management in mobile and multihomed nodes. 94 p. (175 p.) Yhteenveto 1 p. 2010.

113 KUJALA, TUOMO, Capacity, workload and mental contents - Exploring the foundations of driver distraction. 146 p. (253 p.) Yhteenveto 2 p. 2010.

114 LUGANO, GIUSEPPE, Digital community design - Exploring the role of mobile social software in the process of digital convergence. 253 p. (316 p.) Yhteenveto 4 p. 2010.

115 KAMPYLIS, PANAGIOTIS, Fostering creative thinking. The role of primary teachers. - Luovaa ajattelua kehittämässä. Alakoulun opettajien rooli. 136 p. (268 p.) Yhteenveto 2 p. 2010.

116 TOIVANEN, JUKKA, Shape optimization utilizing consistent sensitivities. - Muodon optimointi käyttäen konsistentteja herkkyyksiä. 55 p. (130p.) Yhteenveto 1 p. 2010.

117 MATTILA, KEIJO, Implementation techniques for the lattice Boltzmann method. - Virtausdynamiikan tietokonesimulaatioita Hila-Boltzmann -menetelmällä: implementointi ja reunaehdot. 177 p. (233 p.) Yhteenveto 1 p. 2010.

118 CONG, FENGYU, Evaluation and extraction of mismatch negativity through exploiting temporal, spectral, time-frequency, and spatial features. - Poikkeavuusnegatiivisuuden (MMN) erottaminen aivosähkönauhoituksista käyttäen ajallisia, spektraalisia, aikataajuus - ja tilapiirteitä. 57 p. (173 p.) Yhteenveto 1 p. 2010.

119 LIU, SHENGHUA, Interacting with intelligent agents. Key issues in agent-based decision support system design. 90 p. (143 p.) Yhteenveto 2 p. 2010.

120 AIRAKSINEN, TUOMAS, Numerical methods for acoustics and noise control. - Laskennallisia menetelmiä akustisiin ongelmiin ja melunvaimennukseen. 58 p. (133 p.) Yhteenveto 2 p. 2010.

121 WEBER, MATTHIEU, Parallel global optimization Structuring populations in differential evolution. - Rinnakkainen globaalioptimointi. Populaation rakenteen määrittäminen differentiaalievoluutiossa. 70 p. (185 p.) Yhteenveto 2 p. 2010.

122 VÄÄRÄMÄKI, TAPIO, Next generation networks, mobility management and appliances in intelligent transport systems. - Seuraavan sukupolven tietoverkot, liikkuvuuden hallinta ja sovellutukset älykkäässä liikenteessä. 50 p. (111 p.) Yhteenveto 1 p. 2010.

123 VIUKARI, LEENA, Tieto- ja viestintätekniikka-välitteisen palvelun kehittämisen kolme diskurssia. - Three discourses for an ICT-service development . 304 p. Summary 5 p. 2010.

124 PUURTINEN, TUOMAS, Numerical simulation of low temperature thermal conductance of corrugated nanofibers. - Poimutettujen nanokuitujen lämmönjohtavuuden numeerinen simulointi matalissa lämpötiloissa. 114 p. Yhteenveto 1 p. 2010.